FINAL REPORT

Empirical Investigation of the Factors Influencing Marine Applications of EMI

SERDP Project MR-2409

MARCH 2018

Thomas Bell
Leidos

Bruce Barrow
Acorn SI

Daniel Steinhurst
Glenn Harbaugh
Nova Research

Carl Friedrichs
Grace Massey
Virginia Institute of Marine Science

Page Intentionally Left Blank

Page Intentionally Left Blank

REPORT DOCUMENTATION PAGE

Form Approved
OMB No. 0704-0188

1. REPORT DATE *(DD-MM-YYYY)*
03/30/2018

2. REPORT TYPE
SERDP Final Report

3. DATES COVERED *(From - To)*
9/27/2014 - 3/31/2018

4. TITLE AND SUBTITLE
Empirical Investigation of the Factors Influencing Marine Applications of EMI

5a. CONTRACT NUMBER
Contract: 14-C-0046

5b. GRANT NUMBER

5c. PROGRAM ELEMENT NUMBER

6. AUTHOR(S)
Thomas Bell, Leidos
Bruce Barrow, Acorn SI
Daniel Steinhurst and Glenn Harbaugh, Nova Research
Carl Friedrichs and Grace Massey, Virginia Institute of Marine Science

5d. PROJECT NUMBER
MR-2409

5e. TASK NUMBER

5f. WORK UNIT NUMBER

7. PERFORMING ORGANIZATION NAME(S) AND ADDRESS(ES)
Leidos
4001 N Fairfax Drive, Suite 675
Arlington, VA 22203

8. PERFORMING ORGANIZATION REPORT NUMBER
MR-2409

9. SPONSORING/MONITORING AGENCY NAME(S) AND ADDRESS(ES)
Strategic Environmental Research and Development Program
4800 Mark Center Drive, Suite 17D03
Alexandria, VA 22350-3605

10. SPONSOR/MONITOR'S ACRONYM(S)
SERDP

11. SPONSOR/MONITOR'S REPORT NUMBER(S)
MR-2409

12. DISTRIBUTION/AVAILABILITY STATEMENT
Distribution A; unlimited public release

13. SUPPLEMENTARY NOTES

14. ABSTRACT
This report documents results from a series of measurements of target electromagnetic induction (EMI) responses in a large salt water tank, and background EMI responses in various salt water and sedimentary environments along the York River, VA estuary. The electronics and data acquisition system used in the tests was a standard transient EMI (TEM) package used for munitions detection and classification on land. For the tank tests, targets included simple aluminum and steel test items (spheres, spheroids and cylinders) as well as inert ordnance items. The basic test protocol involved carefully measuring and comparing target and background responses in air and in the water.

15. SUBJECT TERMS
Marine Applications, EMI, Acoustic Doppler Current Profiler, Berkeley UXO Discriminator, Compact Data Acquisition System, Electromagnetic Induction, Marine Berkeley UXO Discriminator, Time-domain Electromagnetic Multi-sensor Towed Array Detection System (TEMTADS), Unexploded Ordnance

16. SECURITY CLASSIFICATION OF: a. REPORT	b. ABSTRACT	c. THIS PAGE	17. LIMITATION OF ABSTRACT	18. NUMBER OF PAGES	19a. NAME OF RESPONSIBLE PERSON / 19b. TELEPHONE NUMBER *(Include area code)*
UNCLASS	UNCLASS	UNCLASS	UNCLASS	94	Thomas Bell / 301-712-7021

Page Intentionally Left Blank

Abstract

This report documents results from a series of measurements of target electromagnetic induction (EMI) responses in a large salt water tank, and background EMI responses in various salt water and sedimentary environments along the York River, VA estuary. The electronics and data acquisition system used in the tests was a standard transient EMI (TEM) package used for munitions detection and classification on land. For the tank tests, targets included simple aluminum and steel test items (spheres, spheroids and cylinders) as well as inert ordnance items. The basic test protocol involved carefully measuring and comparing target and background responses in air and in the water. On the whole we found nothing to indicate that a salt water environment *per se* compromises the utility of advanced TEM sensors for target classification.

We observed relatively weak electric field contributions to the early time response for bare aluminum targets located off to the side of the transmit and receive coils. This is where the electric field is strongest relative to the primary magnetic field. Even for bare aluminum targets it was not a significant factor for most sensor-target geometries. With the exception of test setups specifically targeting electric field effects we found no significant differences between measured responses in air and in salt water for the different test items and test geometries.

Measurements of the background response *vs*. depth were made at field sites along the York River. The water salinity varied from fresh or slightly brackish (<2‰) to ~25‰, and bottom sediments ranged from mud to silty sands. We found that a four layer model comprising a non-conducting half-space (air) over a conducting water layer, combined with a shallow conducting sediment layer overlaying a deeper, more resistive half-space provides a good match to the data. Calculations indicate that the background response and its variation are not small compared representative munitions signals at early times. However, when the background response varies smoothly it can be effectively dealt with by standard filtering techniques similar to those used in munitions response surveys on land.

Contents

Figures

Tables

Acronyms

ADCP	Acoustic Doppler Current Profiler
BUD	Berkeley UXO Discriminator
CB	Clay Bank
cDAQ	Compact Data Acquisition System
CI	Catlett Islands
CTD	Conductivity Temperature Depth
EMI	Electromagnetic Induction
ESTCP	Environmental Security Technology Certification Program
FP	Ferry Point
GI	Goodwin Island
GP	Gloucester Point
MBUD	Marine Berkeley UXO Discriminator
NWS	Naval Weapons Station
PM	Pamunkey Mud
PS	Pamunkey Sand
PVC	Polyvinyl chloride
Rx	Receive
R/V	Research Vessel
SERDP	Strategic Environmental Research and Development Program
SHM	Sweet Hall Marsh
SNR	Signal to Noise Ratio
SPM	Suspended Particulate Matter
TC	Taskinas Creek
TEM	Transient Electromagnetic

TEMTADS	Time-domain Electromagnetic Multi-sensor Towed Array Detection System
TFS	Total Fixed Solids
TS	Total Solids
TVS	Total Volatile Solids
Tx	Transmit
UXO	Unexploded Ordnance
VIMS	Virginia Institute of Marine Science
WP	West Point

Page Intentionally Left Blank

Objective

Many active and former military installations have ranges and training areas that include adjacent water environments such as ponds, lakes, rivers, estuaries, and coastal ocean areas. In other sites, training and testing areas were deliberately situated in water environments. Disposal and accidents have also generated significant munitions contamination in the coastal and inland waters in the United States. On land, the Environmental Security Technology Certification Program (ESTCP) Classification Pilot Program has demonstrated that the advanced electromagnetic induction (EMI) sensor arrays emerging from research sponsored by the Strategic Environmental Research and Development Program (SERDP) and ESTCP can be used to reliably detect and classify buried unexploded ordnance (UXO) at real munitions response sites under operational conditions. The marine environment introduces complexities in the response of these sensor systems which could adversely affect performance. This project is a comprehensive research study of the factors affecting the performance of advanced EMI sensor arrays in the marine environment.

This research effort includes controlled tank tests addressing the fundamental physics of the EMI response in a conducting medium and field measurements of the EMI response to the water column and underlying sediments at various representative marine sites. Our motivation is that there is very little hard empirical data on the performance of transient EMI (TEM) sensor arrays in marine environments. Such data are needed to validate models for predicting underwater EMI detection and classification performance as well as the simplifying assumptions used to render the model calculations tractable. The objectives of this work are to:

- Validate the models for EMI performance in the marine environment and the assumptions that are made to simplify the model calculations, and
- Inform the models regarding parameter values appropriate to different sedimentary environments and the level of complexity that must be retained to support reliable EMI data inversion and target classification.

Our ultimate goal is to have fully validated models that can then be used to properly interpret and extrapolate test results of underwater EMI systems and delineate system requirements and specifications needed to meet underwater munitions response survey objectives.

The first part of this report documents results of the tank testing. Specific objectives of this phase of the project were to carefully measure and quantify the effects of:

- Electric field (current channeling) signals, and
- Signal distortion by propagation through salt water

on monostatic and bistatic TEM sensor performance as it relates to target classification. These are addressed in the Results and Discussion section under the Target Response heading. During the course of the testing we observed increased noise levels with some sensor configurations and have included a section on that issue as well.

The project plan included a Go/No-Go decision point following completion of the analysis of data from the tank tests. The results indicated that a salt water environment *per se* does not compromise the utility of advanced TEM sensors for target classification. We therefore proceeded with field measurements of the effects of bottom sediments and water column variability on the EMI response in various types of marine environment. These comprised a series of cruises along the York River estuary during the summer of 2016, described in the Field Tests section of the Technical Approach.

Results of the field measurements are discussed in the R/V Hull Interference and Background Response sub-sections of the Field Tests section of the Results and Discussion. Comparisons of the background response models (described in the first Appendix) with data as well as a discussion of the implications of our findings for underwater EMI systems are also included in the Results and Discussion section. We find that a four layer model comprising a non-conducting half-space (air) over a conducting water layer, combined with a shallow conducting sediment layer overlaying a deeper, more resistive half-space provides a good match to the data. Calculations indicate that the background response and its variation are not small compared to representative munitions signals at early times. However, the background response varies smoothly and can be effectively dealt with by filtering techniques similar to those used in munitions response surveys on land.

Technical Approach

Tank Tests

Testing was done at the Naval Research Laboratory's test facility at the Army Research Laboratory Blossom Point, MD facility. The basic test setup is shown in Figure 1. A 10 ft diameter by 11 ft deep (3.05x3.35 m) 6000 gallon (22.7 kl) industrial plastic tank was partially buried and filled with a salt water solution. Salinity varied from 0 to 35‰. During the course of the testing water temperatures ranged from less than 5°C to 25°C. At various times the electrical conductivity of the water was measured using a Hanna Instruments HI98304 DIST4 electrical conductivity sensor (using samples diluted with distilled water for conductivities greater than 2 S/m). At specific salinities, conductivity as a function of temperature was determined using standard tables and formulae [1]. It varied from 0.04 to 5.6 S/m during the course of the testing, depending on salinity and temperature. Most of the data were collected at 35‰, with conductivity in the range 3.2-4.5 S/m. The water in the tank was mixed with a removable pump each day before the start of testing to eliminate temperature and salinity stratification.

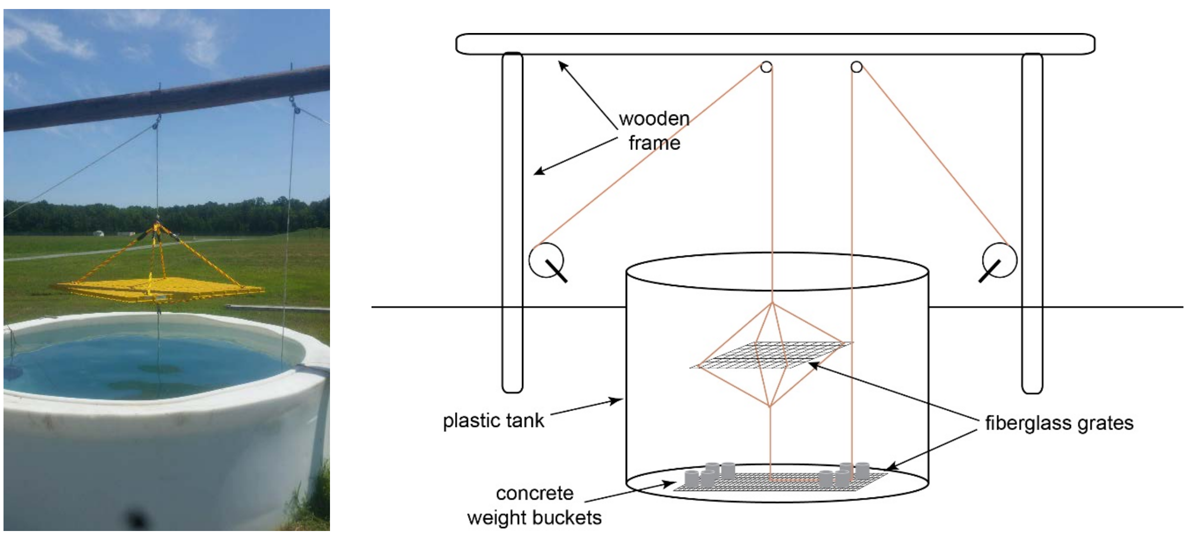

Figure 1. Basic test setup. Sensors and targets are attached to a fiberglass grate which can be raised above and lowered into the 6,000 gallon (10 ft diameter by 11 ft deep) plastic tank.

Sensors and targets were attached to a fiberglass grate which could be winched up above the tank or lowered down into the water. The basic test protocol involved repeating measurements with and without a target in the water and then again in air with the rig set beside the tank. This allowed background response contributions to be removed from the target response measurements and allowed for direct in water and in air comparison. For some of the tests the water in the tank was grounded using 6 AWG solid copper wire attached to a ground rod emplaced next to the tank. This had no noticeable effect on the noise seen by the sensors. However, the EMI response from the wire interfered with the target response measurements. All of the target response data referred to in this report was collected with the ground wire and rod removed.

A variety of different transmit coils were used in the testing to evaluate effects on noise and background response. Eight variants were tested with sizes ranging from 34 cm square to 1 m square. Some of the coils were isolated from the surrounding water by insulating enclosures and some (with lightly covered, insulated windings) were exposed to the water. The various configurations are listed in Table 1. The small, medium and large coils were hand wound using THHN 14 AWG stranded copper wire, which has a 0.38 mm (15 mil) thick layer of polyvinyl chloride (PVC) insulation covered by a 0.10 mm (4 mil) thick nylon jacket. The transmit coils were paired with standard TEMTADS 8 cm receive cubes [2] enclosed in either a small watertight Pelican case or a machined PVC pressure housing. In support of ESTCP project MR-201313, we also tested a 1 m square coil with a 10 cm receive cube assembled by Geometrics. That coil had 19 turns on a fiberglass frame and was covered with a coating of truck bedliner for waterproofing.

Table 1. Transmit coils tested in tank.

Coil	Size	Turns	Frame	Enclosure
TEMTADS PC	35 cm	25	Styrofoam	Pelican Case
TEMTADS PH	35 cm	25	Styrofoam	Delrin Pressure Housing
Small	34 cm	20	Plastic	None
Med Exposed	68 cm	16	Wood	None
Med Enclosed	68 cm	16	Wood	Wood & Polyurethane
Med Rectangular	61x91 cm (2x3 ft)	16	Plastic	None
Large	1 m	26	Fiberglass	None
EM61S	0.5x1 m	-	-	Plastic/Resin

Examples of the various coils are shown in Figure 2. The small coil is shown in the upper row of photographs in Figure 2 (a and b). It is 34 cm square with 20 turns over a height of 5.3 cm. The “exposed” medium coil is shown with the receive cube in the pressure housing in Figure 2(c). It has a 5 cm, 16 turn winding on a 68 cm square wooden frame. Figure 2(d) is a second version of this coil enclosed in a waterproof wood and polyurethane housing. Figure 2(e) shows the Geonics EM61 submersible (EM61S) coil. Detail of an 8 cm receive cube and its machined PVC pressure housing is shown in Figure 2(f). The standard TEMTADS transmit coil (35 cm square, 25 turns over 8 cm) with co-located three axis receive cube is shown in a watertight Pelican case in Figure 2(g) and Figure 2(h) shows the Pelican-encased TEMTADS coils in a typical bistatic (*i.e.* with a second receiver displaced from the transmitter) configuration with the second receive cube offset by 40 cm.

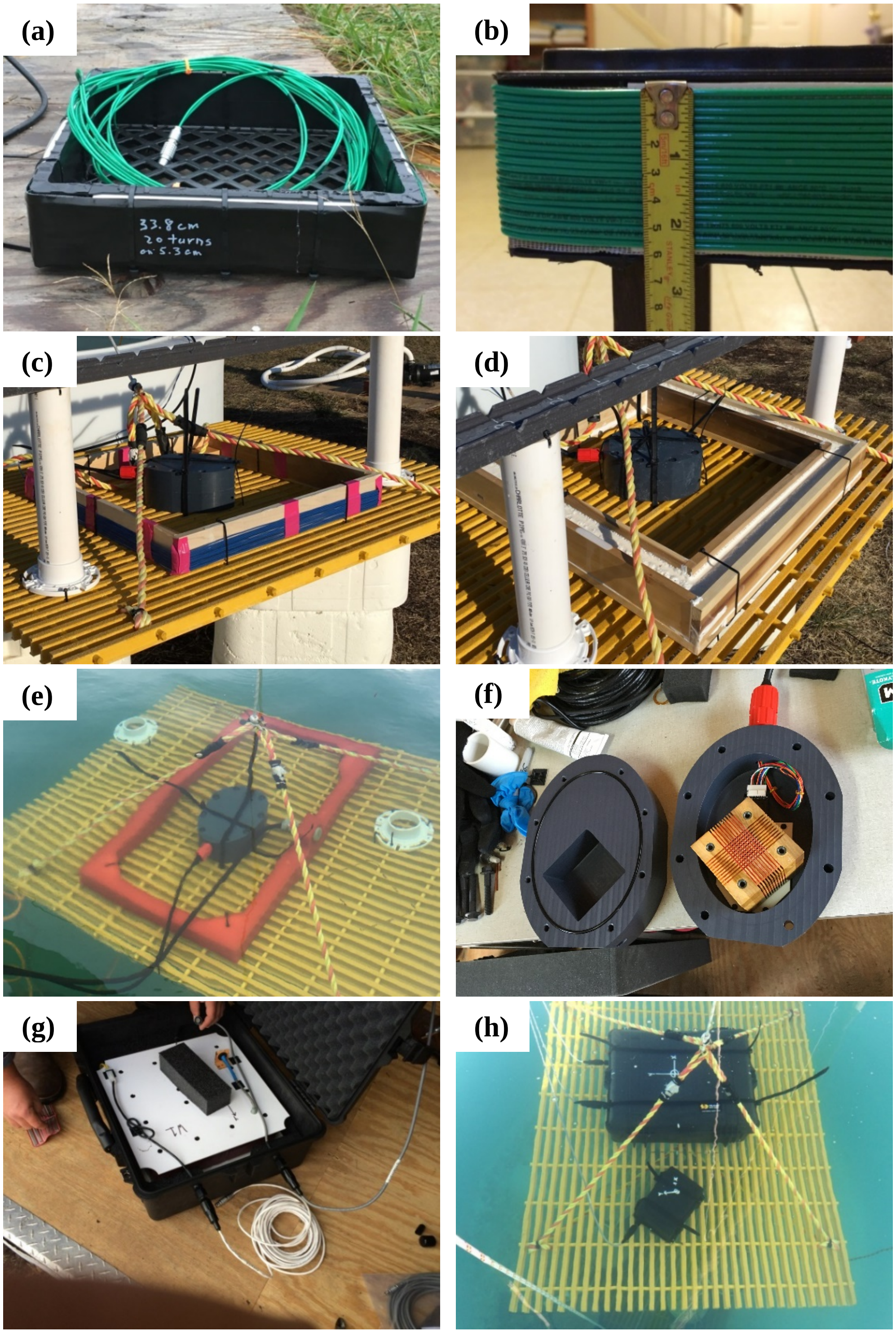

Figure 2. Transmit coils. (a) Small coil. (b) Small coil windings. (c) 67cm square coil with receive cube in PVC pressure housing. (d) 68 cm square coil encased in wood and polyurethane frame. (e) Geonics EM61S coil. (f) 8 cm receive cube and PVC pressure housing. (g) Standard TEMTADS transmit coil / receive cube pair in Pelican case. (h) Bistatic arrangement of TEMTADS transmit and receive coils.

The coils were driven with a new compact version (cDAQ) of the advanced EMI electronics developed by G&G Sciences. The data acquisition electronics were placed on a table roughly five meters from the tank. The acquisition computer was powered from an available 60 Hz AC line. The transmitter and receiver electronics were powered from a battery. The system is capable of generating a variety of bipolar transmit waveforms, as well as being flexible in stacking and time gating the measured transient decays. We used the standard TEMTADS cued static pulse duration of 25 ms. Peak transmit currents were between 5 and 6 A. Raw transients sampled at 250 kHz were recorded for noise studies. For background and target response measurements, roughly 200 decays were averaged and 121 logarithmically-spaced time gates (5% gate width) were recorded, the last 100 or so of which (corresponding to decay times greater than about 0.1 ms) are typically used for target classification.

Excluding checkout and sensor tests, 1089 data files were collected during 22 days of testing spread out over the period from July 2015 into March 2016. Table 2 gives the breakdown between noise measurements, background response measurements and target response measurements. Test objects included a 40 mm projectile, 81 mm mortar, 90 mm projectile, and 3-in Stokes mortar, as well as aluminum and steel spheres, cylinders and spheroids. The table includes data collected on corroded and bio-fouled 1x4 inch steel bar stock in support of SERDP project MR-2500 (Effects of Target Corrosion on Advanced EMI Signatures in Underwater Environments), but does not include 108 files of data collected with the Geometrics coil in support of ESTCP project MR-201313 (Underwater Advanced Time-domain Electromagnetic System).

Table 2. Breakdown of data collection.

Purpose	Number of files
Noise tests	193
Background response	205
Target response	691
Total	1089

Figure 3 shows examples of various test setups used to collect target response data. The photograph at top left (a) shows the 90 mm projectile on notched fiberglass rail 50 cm above medium rectangular coil with a co-located receive cube in the small Pelican case. The rail supports are PVC pipe. The rig is in the water at a depth of 1 m. Top right (b) is a 10.2 cm (4 inch) diameter aluminum ball on the rail 30 cm above the medium enclosed coil with receive cubes in the small Pelican case (left) and the machined pressure housing (right). The middle left photo (c) shows a bio-fouled steel bar on cups located between the receive cube and the inner edge of the medium rectangular coil. This geometry gives relatively strong electric field excitation along the axis of the bar. The middle right photograph (d) shows a bare steel bar on a grid secured over the center of a bistatic receive cube in the small Pelican case. The encased

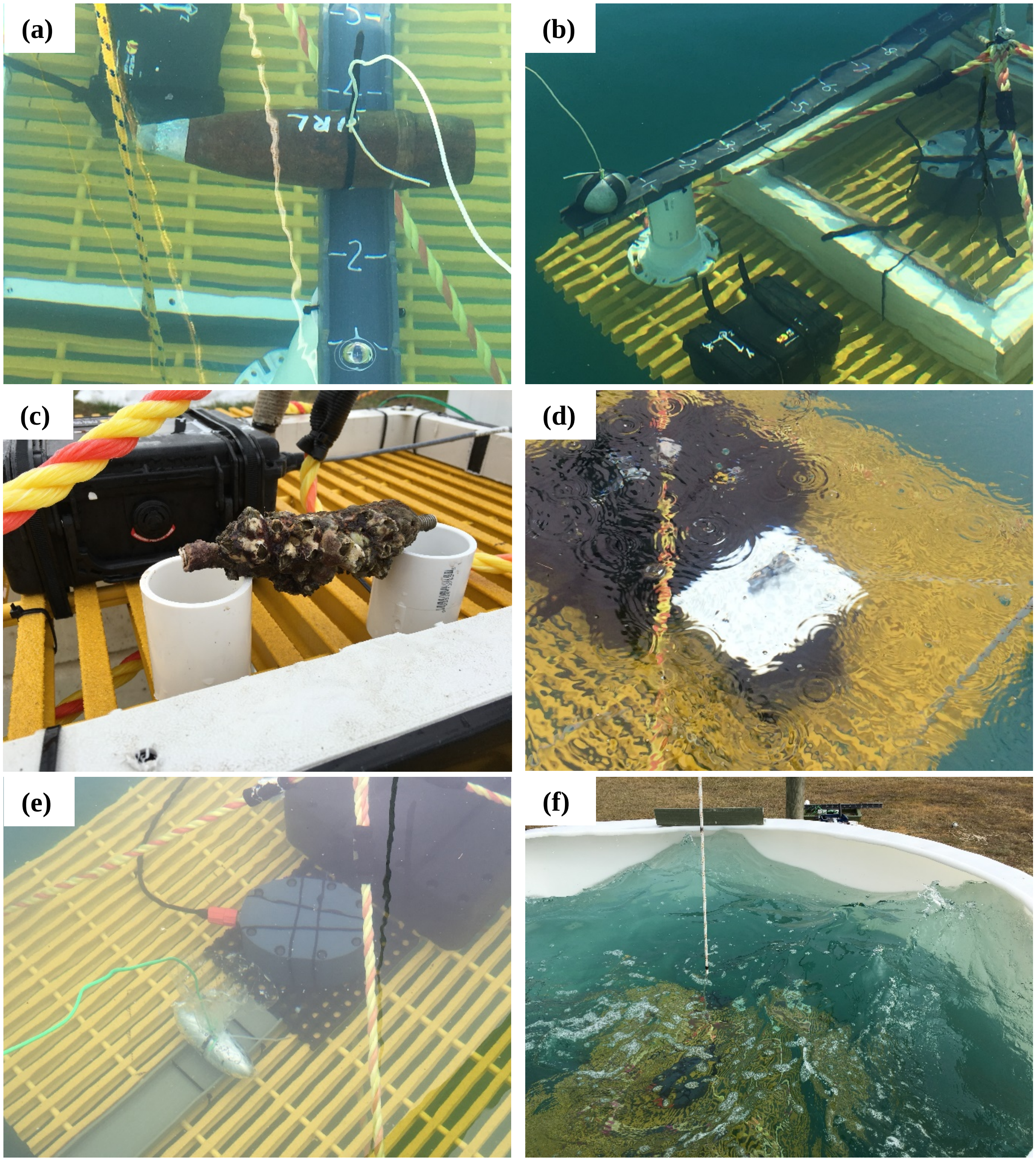

Figure 3. Test setup examples. (a) 90 mm projectile on rail 50 cm above medium rectangular coil with co-located receive cube in small Pelican case, (b) 4 inch aluminum ball on rail 30 cm above medium enclosed coil, (c) bio-fouled steel bar between receive cube and edge of medium rectangular coil, (d) bare steel bar on grid over bistatic receive cube on a rainy day, (e) aluminum spheroid wrapped in plastic bag (to suppress current channeling) with coils in pressure housings, (f) waves excited in tank to test effects on background response.

cube is offset 40 cm from the center of a standard TEMTADS transmit coil / receive cube (Tx/Rx) pair in the larger Pelican case. The lower left photo (e) shows a 6.67x6.67x20 cm aluminum spheroid wrapped in plastic (to suppress current channeling) on a notched fiberglass rail secured to the grate outboard of a bistatic receive cube in its pressure housing. A Tx/Rx pair is in the large pressure housing. The bistatic cube is centered 40 cm from the center of the Tx/Rx pair. Bottom right (f) shows waves excited in the tank to test effects of waves on the background response. The waves were resonantly excited using a large styrofoam block as a plunger. The crest-to-trough wave height is about 30 cm and the period of the waves is roughly 1 s.

Relevant theory used in our analysis and interpretation of the tank test results is included in the first Appendix.

Field Tests

Field tests focused on measurements of the background response and its variation with depth, along with supporting measurements of hydrographic and sediment properties at various locations along the York River. Decades of research by the Coastal Hydrodynamics and Sediment Dynamics Lab at the Virginia Institute of Marine Science (VIMS) have gone into characterizing the hydrography and sediments of the York River estuary [3]. The York overlies a deep sequence of sediment and sedimentary rock strata, the uppermost of which is a weakly cemented layer of mostly alluvial and estuarine sand and silt up to ~10 m thick, which overlies a quite firmly cemented layer of marine organism shell fragments and silty sand 40-50 m thick [4, 5]. Throughout most of the energetic parts of the estuary, physical and biological processes mix the sediments to depths of 25-200 cm, and the sediment porosity averages about 85% in this mixed layer [6].

Figure 4 shows the temperature and salinity during 2016 at the four long term monitoring sites run by VIMS in the Chesapeake Bay National Estuarine Research Reserve [4]. The Goodwin Islands (GI) are located on the southern side of the mouth of the York River. The Catlett Islands (CI) site is ~18 km upriver from the mouth. Taskinas Creek (TC) is located on the southern side of the river, ~38 km from the mouth, and Sweet Hall Marsh (SHM) is located in the tidal fresh-brackish transitional zone of the Pamunkey River, one of two major tributaries of the York River. Locations are shown by the white circles in Figure 5. The data were recorded at fifteen minute intervals. Water temperatures are comparable at the sites. Conductivity depends on both temperature and salinity. It is an increasing function of temperature at a fixed salinity. Year-long averages of specific conductivity (conductivity referenced to a temperature of 25 °C) at the four sites are 3.29 S/m, 3.26 S/m, 2.67 S/m and 0.16 S/m, respectively. Archie’s law [7, 8] provides a relationship between the electrical conductivity of the sediments and the conductivity of the pore water in the sediments. In Archie’s law the formation factor is the ratio the sediment resistivity to the pore water resistivity. Sediment conductivity/resistivity is controlled by the pore water conductivity/resistivity (a function of pore water salinity, temperature and pressure), the sediment fractional porosity, and sediment pore morphology (sediment fabric). It is usually assumed that the overlying water and pore water have the same conductivity. The exponent in Archie’s law is controlled by grain shape and pore morphology. With summer temperatures in the upper 20’s, the average values of the specific conductivity are probably indicative of the pore water conductivity at the sites.

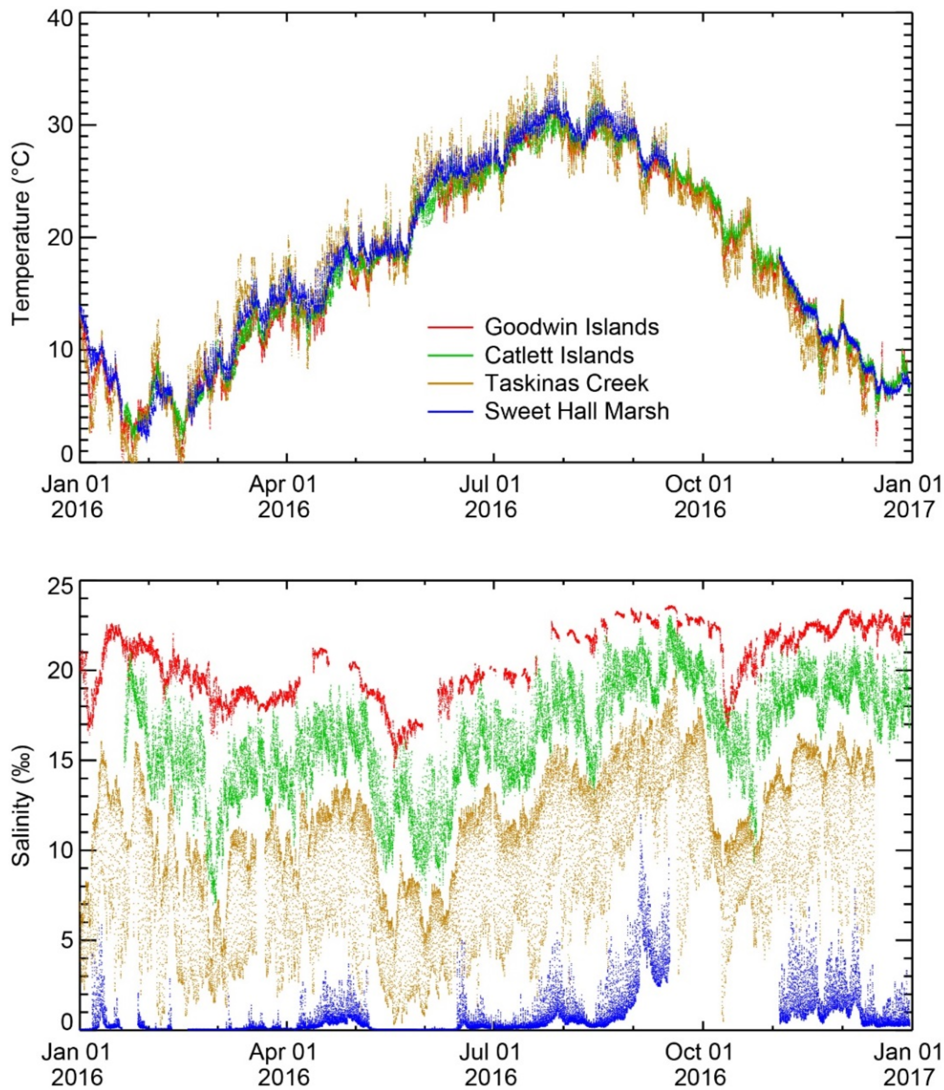

Figure 4. Temperature and salinity records at VIMS long term monitoring sites along the York River estuary.

Field data were collected at eight sites along the York River estuary. At four of the sites, the seafloor sediment type consisted of mostly mud and silt, and the others were more fine sand and sandy mud. Figure 5 shows the sites marked on the map with orange triangles. Three of the sites are located in the high salinity regime near the mouth of the river. They are identified as Goodwin Island (GI), Gloucester Point (GP) and Naval Weapons Station (NWS), located 4.2, 13.7 and 13.8 km upriver from the mouth of the York River. The mid-salinity regime stations are identified as Clay Bank (CB) and Ferry Point (FP), located 27.3 km and 31.7 km from the mouth, respectively. The Catlett Island monitoring site is midway between our GP/NWS and CP/FP test sites. The low-salinity regime stations in the Pamunkey River, the southern tributary of the York, are identified as West Point (WP), Pamunkey Sand (PS) and Pamunkey Mud (PM). They are located 56.1, 62.2 km and 67.6 km from the mouth of the York. Sweet Hall Marsh is just upstream from our PM site.

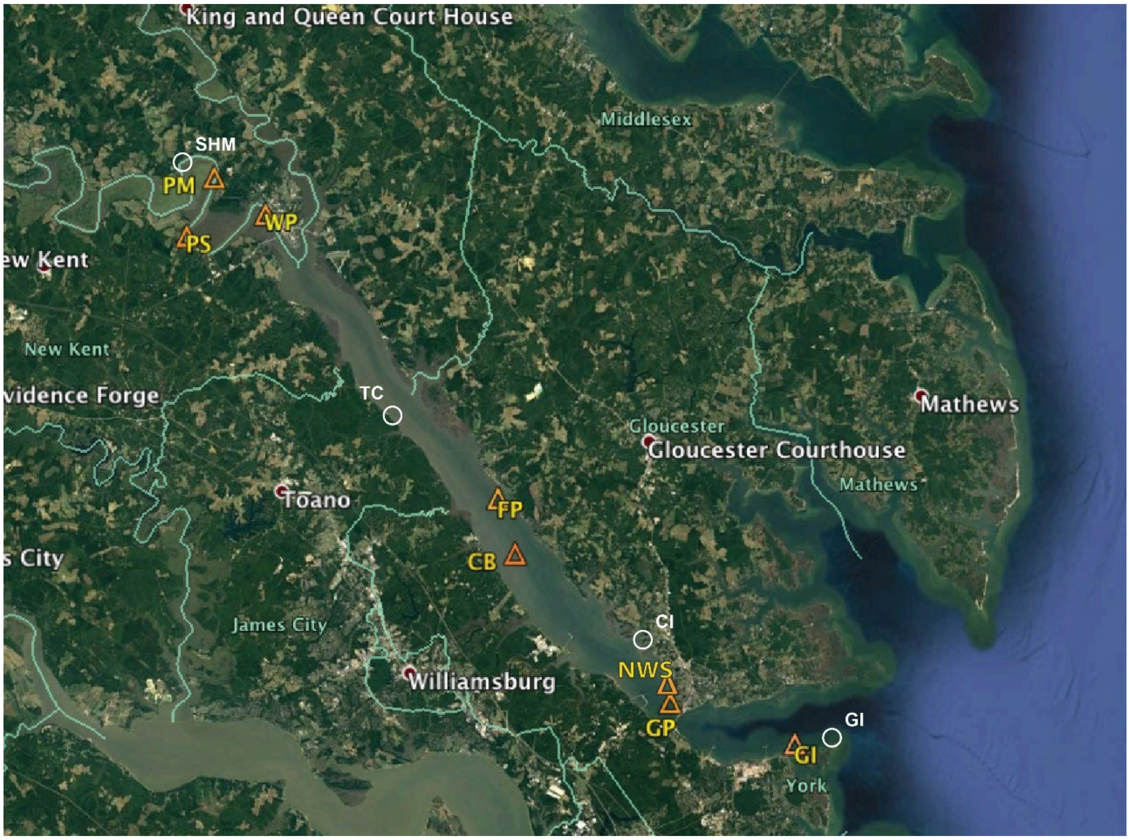

Figure 5. Study sites along the York River estuary, a tributary of the Chesapeake Bay, and into the Pamunkey River, the southern tributary of the York River. Site locations are marked with orange triangles. Locations of monitoring sites marked with white circles.

Two vessels were used for data collection. The R/V Elis Olsson, a 29 ft. Monarch (Figure 6, right), was used to deploy the TEM sensor and to collect water column velocity profiles. The R/V Heron, a 26 ft. Garvey (Figure 6, left) was primarily used to collect bottom sediment for site characterization, temperature and salinity profiles, and water samples for suspended solids concentrations at three depths in the water column. It was also used for the final TEM data collection at the Naval Weapons Station (NWS) site. The picture in the center shows the TEM sensors being lowered into the water.

Table 3 summarizes the data collections. The hydrographic and sediment data have been archived in the York River, Virginia Data Archive [9]. Red entries indicate work done on the R/V Elis Olsson and black entries indicate work done on the R/V Heron.

Table 3. Summary of data collection at York River sites.

Table 1.

YR160623 - YR160920 June 23 - Sep 20, 2016 SERDP EMI/Sediment Station Log

Cruise	Station	Date	Time EST	Location	Expected Sed Type	Station Code	Lattitude 37 deg N	Longitude -76 deg W	depth (m)	GOMEX Sub Cores		CTD Cast	TSS	ADCP	Hobo Water Level
YR160623		23-Jun	620	Clay Bank	Mud	CB	20.5176	37.5808	5.18			1			
	5656		648				20.5520	37.6609						1	1
YR160624		24-Jun	708	Clay Bank	Mud	CB	20.5200	37.5780	5.19			1			
	5657		720							GUST	Grain Size/Moisture				
	5658		742							GUST	Grain Size/Moisture				
	5659		806							X-ray	Magnetic Susp/Resistivity				
	5660		840							X-ray	Magnetic Susp/Resistivity				
	5661		915										3		
			917									1			
	5662		759				20.5825	37.6662						1	2
YR160701		1-Jul	610	Gloucester Pt	Mud	GP	15.1800	30.6420	4.6			1			
	5663		756							GUST	Magnetic Susp/Resistivity				
	5664									GUST	Magnetic Susp/Resistivity				
	5665		826							X-ray	Grain Size/Moisture				
	5666		846							X-ray	Grain Size/Moisture				
			1255				15.1860	30.6420	4.37			1			
	5667		1300										3		
	5668		617				15.1921	30.6347						1	1
YR160706		6-Jul	820	Pamunkey	Mud	PM	34.0320	51.3660	4.29			1			
	5669		825							GUST	Grain Size/Moisture				
	5670		839							GUST	Grain Size/Moisture				
	5671		852							X-ray	Magnetic Susp/Resistivity				
	5672		901							X-ray	Magnetic Susp/Resistivity				
	5673		915										3		
	5674		916							GUST					
			926				33.8460	51.3720	6.25			1			
	5676		850				34.1007	50.3470						1	1
YR160706_2		6-Jul	957	West Point	Mud	WP	32.8500	49.0620	4.16			1			
	5675		1001										3		
			1123				32.8200	49.0380				1			
	5677		1026				32.7771	49.0179						1	1
YR160714		14-Jul	636	Ferry Point	Sand/Mud	FP	22.5720	38.4780	4.12			1			
	5678		720							Grain Size/Moisture					
	5679		728							X-ray	Grain Size/Moisture				
	5680		759							GUST	X-ray				
	5681		758										3		
	5682		807							Magnetic Susp/Resistivity					
			841				22.5420	38.4660	5.53			1			
	5683		636				22.5455	38.4413						2	1
YR160721		21-Jul	728	Pamunkey	Sand/Mud	PS	31.9740	52.6140	3.46			1			
	5684		756							GUST					
	5685		820							GUST					
	5686		834							Grain Size/Moisture					
	5687		855												
	5688		904							X-ray					
	5689		912							Magnetic Susp/Resistivity					
	5690		920										3		
	5691		925							X-ray					
			949				32.0460	52.5420	4						
	5692		941				31.9817	52.5961						2	1
YR160721_2		21-Jul	1102	Ferry Point	Sand/Mud	FP2	22.5780	38.5320	6.75			1			
	5693												3		
YR160805		8-Aug	523	Goodwin Island	Sand/Mud	GI	13.7040	24.9900	4.4			1			
	5695		545							GUST	Grain Size/Moisture				
	5696		602							GUST					
	5697		610							Magnetic Susp/Resistivity					
	5698		615							Magnetic Susp/Resistivity					
	5699		619							X-ray	Grain Size/Moisture				
	5700		632										3		
	5701		633							X-ray					
			642				13.6980	24.9900	4.48						
	5706						No GPS							1	1
YR160920	5735	20-Aug	1033	Naval Weapons	Mud	NWS	15.4201	30.8492	5.9			1			1
	5736		1040												
	5737		1050										1		
			1057				15.4149	30.8396				1			

Figure 6. Left: R/V Heron collecting a box core at the second Pamunky River site. Center: TEM sensors being lowered into the water. Right: R/V Elis Olsson.

EMI data were collected using a co-located TEMTADS Tx/Rx pair in a Delrin housing and a second bistatic receiver in a PVC housing (see Figure 3e) offset horizontally ~35 cm from the center of the transmit coil. The sensors were mounted on a fiberglass grate which was lowered from the stern davit (Figure 6, center). An Onset HOBO water level sensor was mounted next to the TEM sensors to record sensor depth during deployment. At most sites, the TEM profiles were repeated after letting out the anchor line to allow the R/V to move 5-10 m to a slightly different location. Figure 7 shows the TEM sensor depth profile at the NWS station. There are on average 115 data samples at each depth. The sensors are on the bottom for the final data set.

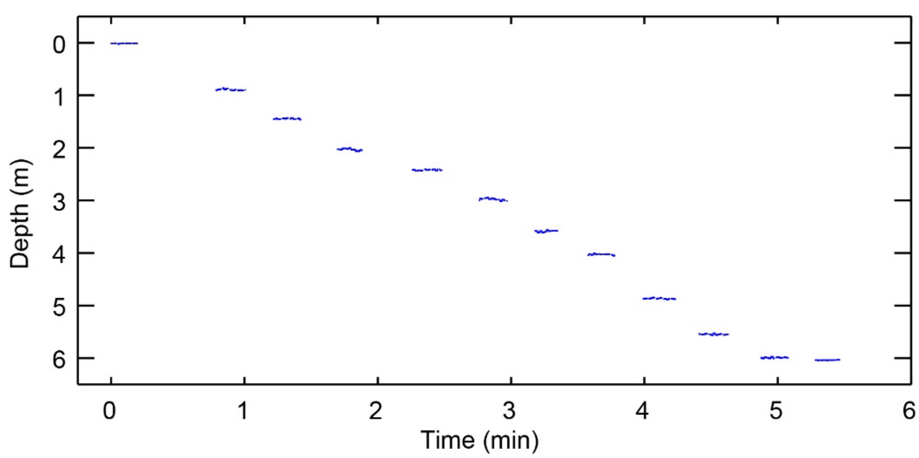

Figure 7. TEM sensor depth profile.

Ancillary measurements of water column and bottom sediment properties were collected to help classify and interpret the results. An Acoustic Doppler Current Profiler (ADCP) was mounted at the bow of the Ellis Olsson to measure current speed and direction from near surface to the bottom for the time the vessel was at anchor. On the supporting R/V, anchored about 30 meters away, conductivity/temperature/depth (CTD) profiles were collected twice, once when first arriving at a location and again toward the end of the sample period. Three water column samples were collected at each location and were later analyzed back at the lab for suspended sediment concentrations (Table 4 in the second Appendix). One sample was collected about a meter off the bottom, a second was collected about a meter from the surface, and the third was collected at a mid-depth.

A YSI Castaway-CTD was used to obtain conductivity-, temperature-, and depth profiles in the water column. The Castaway software, using the 1978 Practical Salinity Scale, derives salinity. Table 3 identifies which box core station the cast was taken coincident with and the maximum depth as recorded by the Castaway. The conductivity and temperature sensors of the Castaway are located in a flow-through channel along the back of the housing. The pressure sensor passes through the housing at the top of the battery cap. The system is hydrodynamically designed to free fall at a rate of about 1 m/s. A six-electrode flow-through conductivity cell with zero external field coupled with a rapid response thermistor attain high measurement accuracies. According to the manufacturer salinity and temperature accuracies are 0.1‰ and 0.05°C respectively.

The Castaway samples at a rate of 5 Hz and internally converts the raw CTD data into a processed profile for each cast. Pressure is corrected for the ambient atmospheric pressure by collecting pressure data at the start and end of the cast while the system is in the air. The air pressure is subtracted from the raw pressure data to get a measure of water pressure only. Since the Castaway is designed to be a flow through system, a rate of change versus time, basically the vertical speed of the system through the water, is calculated for each sample in the data file. If the rate of change in the pressure is less than 0.025 decibars per second, the system is considered to be stationary and the associated sample is discarded. (1 decibar ≈ 1 meter.) The conductivity data are de-spiked to remove erratic measurements near the water surface that can be caused by air bubbles in the conductivity flow cell or measurements made when the system is only partially submerged. After de-spiking, the software averages separately the temperature and conductivity from the down cast samples and the up cast samples into 0.3 decibar bins.

The plot on the left in Figure 8 shows the conductivity profiles at the different test sites. The corresponding temperature, conductivity and salinity data are tabulated in the second Appendix as Table 5.

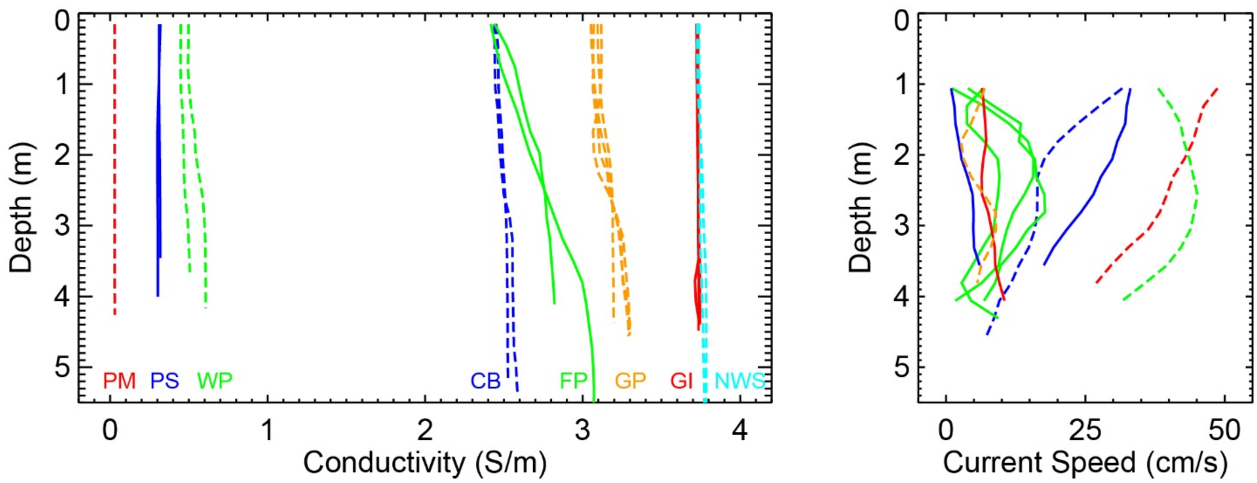

Figure 8. Conductivity profiles at test sites (left) and corresponding current profiles (right)

The lowest water conductivity was sampled at PM (0.03 S/m) and the highest conductivity at NWS (~3.8 S/m). These corresponded to salinities of 0.12‰ at 27°C at PM and 23.5‰ at 25.9°C at NWS. Stations for bottom sediment collection are normally visited ± 1 hour of slack tide. Upriver station times were originally chosen to occur within an hour before slack after ebb tide in order to sample the lowest salinities possible, and the stations times for locations at the river mouth were chosen to occur with in an hour of slack after a flood tide to obtain the highest salinities possible.

At each location, while the TEM sensors were deployed, a "burst" of data was collected with a SONTEK 1200 KHz Acoustic Doppler Current Meter mounted on the bow of the vessel. The burst was averaged for each depth to determine the average water velocity profile during the sample period. The data are included in the second appendix as Table 6. The current profiles are plotted on the right in Figure 8. At Ferry Point (FP), three bursts were taken on July 14th. These are differentiated by the start time of the burst. At Pamunkey Sand (PS), two bursts were collected on July 21st. These are also differentiated by the start time of the burst.

The average water velocity was less than 20 cm/s throughout most of the profile for the stations downriver of Ferry Point (FP). The exception was the top 2 meters at Clay Bank where the velocity increased to over 30 cm/s on the surface. At West Point (WP), upriver of FP, the velocity ranged 30-45 cm/s, with the depths between 2-3.5 meters being the highest. The highest velocities were measured in the Pamunkey, and both stations had a profile where the velocity decreased with depth. At PS the velocity ranged from 33 cm/s on the surface decreasing to 18 cm/s on the bottom. During the second burst collected at the same station, the velocity had dropped to less than 6 cm/s throughout the water column. The highest velocities measured were at Pamunkey Mud (PM) with 49 cm/s on the surface and 29 cm/s on the bottom.

Sediment samples were collected from the R/V Heron at six of the sites (CB, GP, PM, FP, PS and GI) using a GOMEX box core (Figure 6, left). The data collections at the other two sites

(WP and NWS), were not part of the original plan, and only supported bottom grabs of the top few cm of sediment. At muddy sites the GOMEX box core typically captures sediment to about 30 cm depth with the sediment water interface preserved. At sandier sites, even with more weight added, the box core typically does not penetrate as deep into the seafloor. Two sub-cores were typically taken from each same grab sample. The sediment from each site was analyzed back at the lab for grain-size distribution, percent moisture, magnetic susceptibility and electrical resistivity. Supporting analyses included Gust erodibility [10] and X-ray imagery. As expected, the “muddier sites” from each of the conductivity regimes show more erodibility than the ”sandier sites”. Results of the Gust erodibility and X-ray analyses can be found in the archived VIMS final report [11].

At most locations a pair of sub-cores extracted from separate box core sediment samples were combined and analyzed for total fixed solids (TFS), total volatile solids (TVS), moisture and grain size distribution (see Table 3). Each sub-core was extruded and sliced at 1-cm intervals. The corresponding intervals for both cores were consolidated and stored in airtight containers for later analysis at the lab. Immediately upon return to the lab, an aliquot of each sample was weighed in a pre-weighed tin dish and placed into a 103-105°C oven over night. The dried sample was weighed and returned to the oven for at least one hour and reweighed. This process was repeated until two consecutive weights agreed to within 0.0005 g. The dried weight divided by the wet weight x100 gives the percent total solids (TS). The percent of the weight lost upon drying is the water content of the sediment layer, also called the percent moisture (% moisture = 100-TS). The TS sample was then muffled at 550°C for at least 1 hr, placed in a 103-105°C oven to cool and weighed as above until a stable weight was found. The weight loss divided by the wet weight of the sample x100 gives the percent total volatile solids (TVS). This is sometimes used as proxy for percent organic matter present. Total Fixed Solids (TFS) can be found by subtracting TVS from the TS. Percent moisture, porosity, volatile solids and fixed solids for the samples are tabulated in the second Appendix in Table 7. Porosity is calculated from percent moisture assuming that the ratio of the density of the solids in the sediment to the density of the pore water is 2.6 [13]. Corresponding plots of these properties (except for porosity) at 1-cm intervals down core can be found in the archived VIMS Final Report [11].

Grain size, as percent >850 microns, sand, silt, and clay were determined by sieve and pipette methods [12]. An aliquot of each sample was sonicated for at least one hour, after the addition of 10 ml of a surfactant solution (51g Sodium Metaphosphate and 0.3g Sodium Bicarbonate/liter), to break up bonds between the individual particles. The sample was then wet sieved first through a 850-micron sieve to collect the fraction of sample including large shell, gravel, very coarse sand, and debris particles and rinsed into a small pre-weighted beaker. A second 63-micron sieve placed under the first captured the sand size fraction < 850 microns and was rinsed into a second pre-weighted beaker. The water that passed through the sieves, containing the silt and clay size material, was put into a graduated cylinder and diluted to 1 liter. Following [12], two fractions of this solution were pipetted and dried in two weighed tin trays. All four fractions were then dried in a 103-105°C oven until a steady weight was obtained. The percent of each fraction (>850 micron, sand, silt, and clay) was calculated by dividing the dried weight of that fraction by the total (x100). The fractions were then muffled in a 550°C oven, cooled in the 103-105 oven and weighed until a steady weight was obtained. The weight loss of each fraction divided by the total dried weight found above (x100) provides the percent organic matter for each fraction. The data are tabulated in the second Appendix as Table 8. Plots of the >850 micron, Sand, Silt and Clay fractions down core along with the percent organic material associated with each fraction can be found in the archived VIMS Final Report [11].

Goodwin Island (GI), stations 5696 and 5699 and Gloucester Point (GP), stations 5665 and 5666 are both from the high conductivity regime at the mouth of the estuary. GI is distinctly the "sandier" of the two with over 80% sand throughout most of the core. There is slightly more clay than silt in all of the layers. The top 4 cm has more silt and clay and percent moisture (28-31%) than the rest of the core (22-25% moisture). The top 2 cm also has the least amount of fixed solids (68-71%) as compared to the rest of the core (74-77%) and the most organic material, TVS, (0.8%) compared to 0.64-0.75% in the rest of the core. There is about the same amount of organic material associated with the clay fraction as with the silt fraction. The "muddier" of these two stations is GP. The total fixed solids range from 24-53%, less than GI throughout the core indicating more water is retained in the pore spaces of the sediment (73-44%). The site, however, is sandier further down core than expected for a "muddy site" (31-52% below 4 cm.) The percent sand increased throughout the core from surface to depth. There tends to be more silt than clay in the top 4 cm, ranging from 2.5-2.6% and 2.2-2.3% throughout the rest of the core, based on TVS

Claybank (CB), stations S5657 and S5658, and Ferry Point (FP), stations S5678 and S5679, are from the mid-conductivity regime in the middle reaches of the estuary. CB is the "muddy site" with less than 10 percent sand throughout the core and TFS ranging from only 28 -38%. The TVS range from 2.4-2.7% with most of the organic matter associated with the clay fraction, however organic material is also associated with the silt fraction throughout the whole core. FP, the "sandier site" for this regime is composed of over 75% sand throughout the core and as much as 90% in the top 4 cm. The TFS, consistent with being a sandier site, ranges from 53-77%. The TVS ranges from 0.7-1.6%, with most associated with the clay fraction.

Pamunkey Sand (PS), station S5686, and Pamunkey Mud (PM), stations S5669 and S5670, are from the low conductivity regime in the Pamunkey river, a tributary of the York. PM is the "muddy site", with less than 12% sand 2-4 cm in the core and is dominated by the silt fraction. There is a thin sandy layer on the surface of 43%, and below 4 cm the core gets sandier again (30-64%). The TFS profile reflects the layering of sand and mud, with the lowest in the muddy region (24-28 %), and 35-50% in the sandy regions. The TVS is the highest seen at any location and ranges from 2.1-3.0%. Most of the organic material is associated with the clay fraction. PS, the "sandier site" for this regime, is composed of over 85% sand throughout the core and as much as 96% in the 2 cm. The TFS, again consistent with being a sandier site, ranges from 64-

76%. The TVS ranges from 0.45-2.1% with most associated with the larger than 850 micron size class in the bottom 2 cm. This is the only place this holds true.

Box cores were not collected at the West Point (WP) and Naval Weapons Station (NWS) sites. Analysis of bottom grabs at these sites shows NWS to be one of the muddiest sites, while WP is intermediate between the "sandy" sites and the "muddy" sites.

Figure 9 summarizes some of the basic sediment properties at the test sites and illustrates their interrelationship. The plotted values are averages over the entire sample from each site. The plot on the left summarizes the grain size distributions using Shepard's ternary diagram [8, §4.1]. The dashed line corresponds to a clay/silt ratio of 0.68, which is the median value for the five least sandy sites (CB, NWS, GP, PM and WP). In the center and right hand plots mud includes both silt and clay. Porosity is calculated from the average percent moisture (by weight) assuming that the ratio of the density of sediment to the density of water is 2.6 [13]. Both porosity and the ratio of volatile to fixed solids correlate strongly with the amount of mud in the sediment. The muddier sediments have both a higher water content and a higher fraction of organic matter than the sandier sediments.

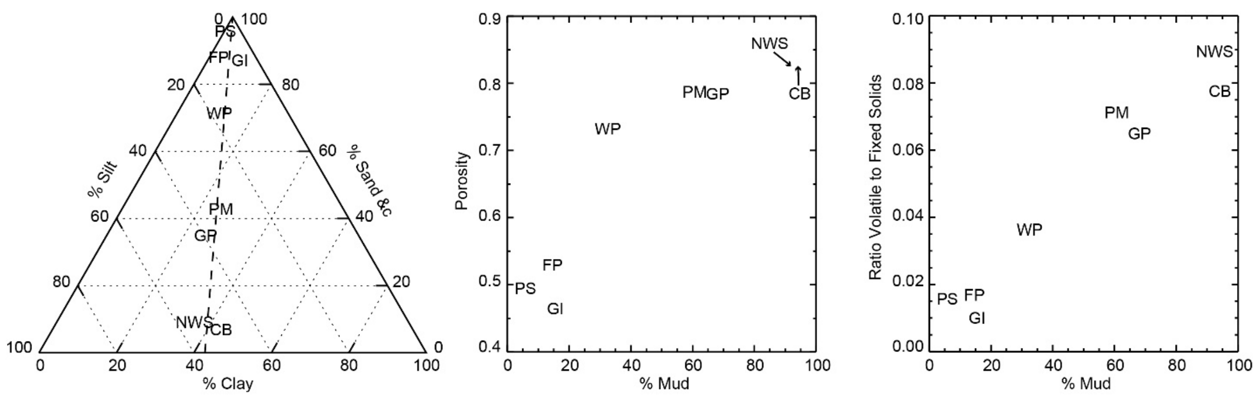

Figure 9. Basic sediment properties at the various test sites on the York River.

A custom resistivity meter and two Wenner-style resistivity probes for sediment resistivity measurements were obtained from Northwest Metasystems, Bainbridge Island, WA. The electronics and probes were designed to be similar to those described in [14]. The resistivity probes malfunctioned and we were not able to obtain relible data on the electrical conductivity of the sediment samples. (The measured values are included in Figure A1.17 and Tables A2.7A-B of the VIMS report [11]. They are inconsistent with previously measured sediment properties at similar sites along the York [15].) A commercially available in-situ sediment resistivity probe or a sediment resistivity imaging system should be used in any future tests. The box cores only yielded sediment samples from the upper 10 cm or so. In order to properly relate results of EMI background response measurements to sediment properties we shoud have deeper samples. At a decay time t, the signal from a TEM sensor near the bottom is responding to structures down to a depth $d = \sqrt{t/\pi\sigma\mu}$ below the bottom, where σ and μ are representative values of the electrical conductivity and magnetic permeability of sediments [16]. In non-magnetic sediments ($\mu = 4\pi \times 10^{-7}$ H/m) with $\sigma \sim 1$ S/m, the EMI penetration depth at 1 ms is $d \sim 3$ m.

The magnetic susceptibility of sediment samples from Glocester Point, Clay Bank and the Pamunkey River sites collected in 2015 was measured using a Bartington magnetic susceptibility core logging sensor [15]. In all cases, the susceptibility was of order 5×10^{-5} SI or less, which was at the noise level of the measurements. The York sediments are basically non-magnetic.

Results and Discussion

Noise

Relative to data collected in air, measurements made using the exposed transmit coils in salt water showed modifications to the transmit current waveform and the initial ring-down of the receiver voltage as well as increased noise levels. Full transient waveforms (*i.e.*, not logarithmically averaged) were recorded with the various coil configurations in air and in water to evaluate these effects. In all cases the receiver coils were isolated, either within the small Pelican case or the PVC pressure housing. Data collected when the transmit coils were isolated from the water (TEMTADS coil in the Pelican case, TEMTADS in the Delrin pressure housing, Geonics EM61 Submersible and medium coil enclosed in wood and polyurethane frame) were not much different than corresponding data collected in air, but significant differences between background responses in air and in water were observed with the other transmit coils.

Figure 10 shows the transmit current cutoff (left) and early time ring-down (right) in air (dashed) and in water (solid) for the 68 cm coil. The top plots are for the exposed coil and the bottom plots are for the same coil encased in a wood and polyurethane frame. The conductivity of the water was ~3.5 S/m. Note that the initial transients are delayed by ~0.028 ms relative to the transmit current cutoff. This has been characteristic of the TEMTADS electronics since the

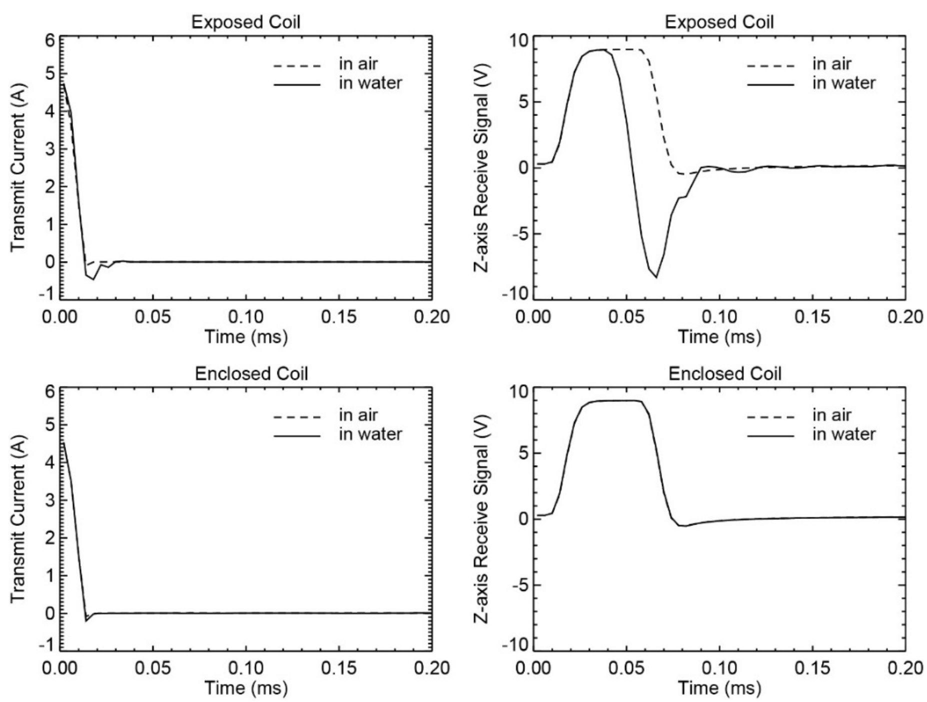

Figure 10. Transmit current cutoff (left) and early time response (right) for exposed 68 cm square coil (top) and enclosed coil (bottom). Dashed lines show transmit current and Z-axis receive signal in air, solid lines show corresponding quantities when the coils are immersed in salt water.

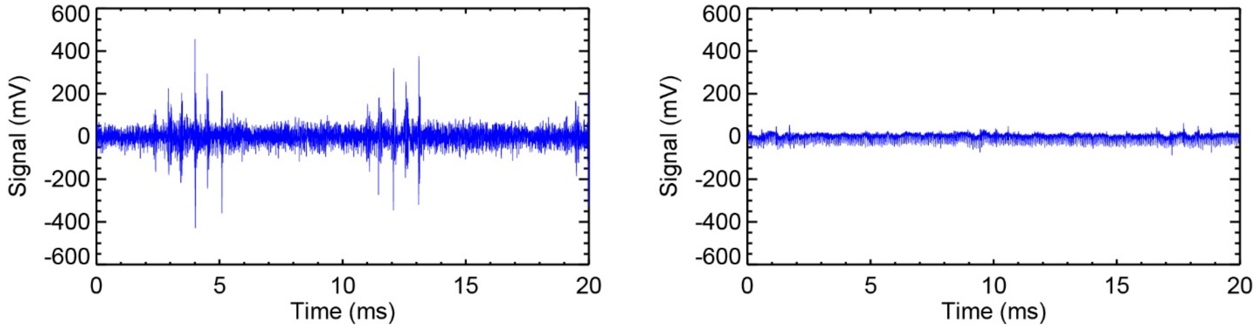

Figure 11. In-air background noise samples recorded one hour apart.

development of the original MR-200601 TEMTADS array [17]. The in-air and in-water cutoff waveforms and initial transients are indistinguishable for the enclosed coil. When the exposed coil is immersed in water, the cutoff acquires a very slight delay and an overshoot relative to the in-air cutoff waveform. The initial transient is significantly modified. Note that with the cDAQ signals are capped at ±10 V. To varying degrees all of the coils show similar behavior depending on whether they are exposed or enclosed. The noise at the receiver also depends on whether or not the transmit coil is exposed or enclosed.

The background noise at our test site is somewhat variable. Examples are shown in Figure 11. The traces are background noise samples recorded in air following transmit current cut-off with the small coil. The data were collected one hour apart on the morning of December 18, 2015. Blossom Point is an active test range and presumably the background electromagnetic noise changes depending on whether or not various emitters are active at the time. The transient EMI noise levels are affected by exposure to the salt water. Figure 12 is a plot of root-mean-square (RMS) noise levels in water *vs*. corresponding noise levels in air measured using the various transmit coils with co-located Z-axis receivers (in this plot the data are not normalized by the transmit current). Dotted lines correspond to fixed ratos of noise in water to noise in air. For some of the tests, the water in the tank was grounded using 6 AWG solid copper wire attached to a ground rod next to the tank. This had no noticeable effect on the noise seen by the sensors, and most of the tests were conducted with the grounding apparatus removed. Corresponding in-air and in-water noise values are from sequential data files with minimal time differences between the measurements. The RMS levels are taken from full transient waveform (ungated) data starting 3 ms after the transmit current cutoff. Noise levels for exposed transmit coil configurations are plotted with circles, while stars correspond to enclosed transmit coils. The noise measured in water is consistently higher than the corresponding noise in air, sometimes by quite a substantial margin. This is not observed for the receive cube axes which are not aligned with the transmit coil.

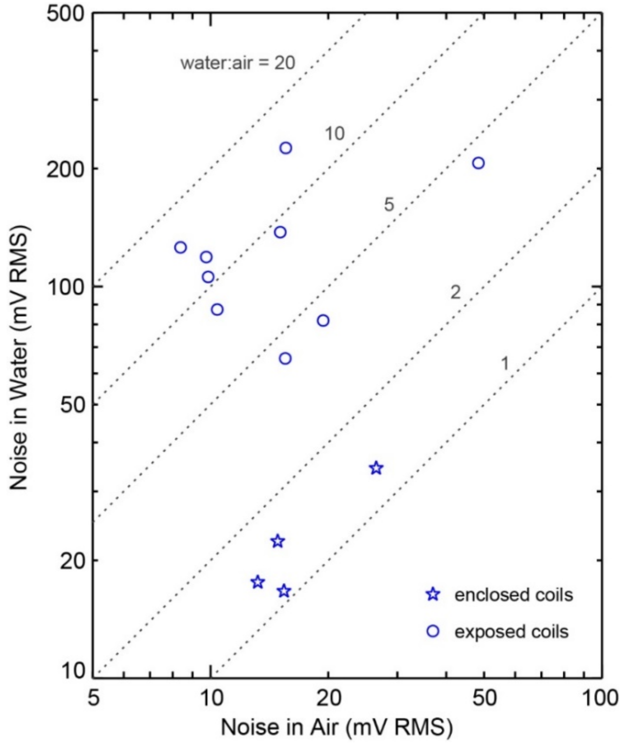

Figure 12. RMS noise measured in air and in water for the various transmit coils.

Isolating the coils from the surrounding water seems to suppress whatever coupling mechanism is at work and to minimize the excess noise in water. The median ratio of in-water noise to in-air noise for measurements with the exposed coils is 9.1, while the median ratio for the enclosed coils is 1.3. Exposure to nearby salt water modifies the capacitance of a coil [18, 19], affecting its resonant frequency and Q-factor [20,21]. This can affect the coil's noise characteristics. Such effects are significantly reduced if the coil is in an insulating cavity [22].

The sensor electronics package is an integral part of the effect. We do not see elevated noise levels when the transmit coil in the water is unplugged and another coil removed far from the tank plugged in in its place. Furthermore, there is no increase in the noise when the pins on the connector on the leads coming from the coil in the water are shorted.

Exposure to the water amplifies the noise without really changing its character. Figure 13 shows noise spectra in air (red curves) and in water (blue curves) for the 68 cm coils. (Construction details are shown in Figure 14.) Spectra for the exposed coil are in the plot on the left and those for the coil encased in the wood and polyurethane enclosure are on the right. We see the same mix of broad- and narrow-band noise, but with elevated levels in water.

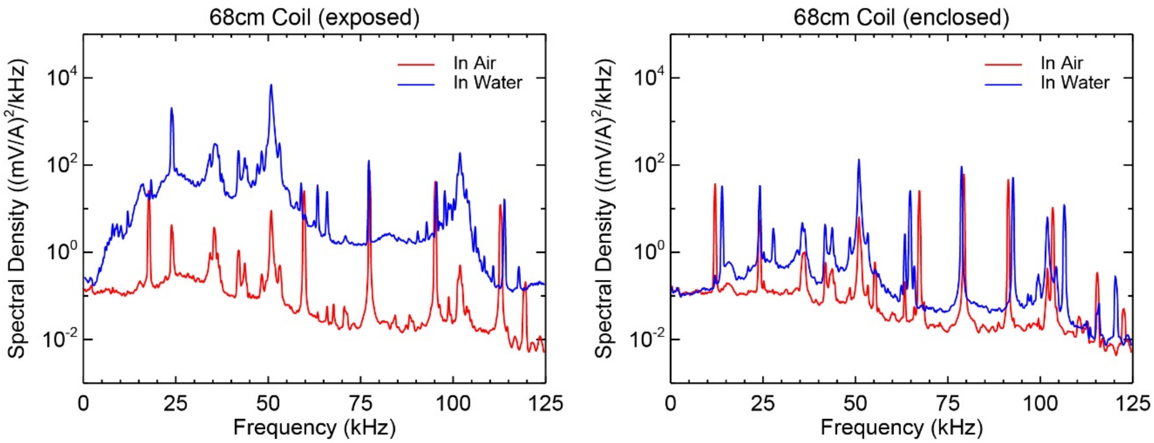

Figure 13. Noise spectra with 68 cm Tx coil in air (red) and in water (blue). Exposed coil on the left, coil encased in wood and polyurethane enclosure on the right.

Figure 14. 68 cm exposed coil (left) and identical coil placed inside a wooden frame (center) which was subsequently filled with polyurethane casting resin (right).

Tank Background Response

Relevant theory for the expected background response in the tank is developed in the first Appendix. Calculating the background response in an unbounded conducting medium is straightforward, but not so for the background response in a tank. We cannot obtain a workable analytical solution which accounts for both the tank sidewalls and the top and bottom simultaneously. We can get solutions which account separately for the sidewalls or for the top and bottom: an infinitely long circular cylinder or an infinite horizontal slab. By considering these effects we can get some idea regarding the net effect of the complete set of boundaries: sidewalls, top and bottom. During ESTCP project MR-200508 it was determined that in the test area the electrical conductivity of the soil is of order 10^{-2} S/m and the magnetic susceptibility is of order 10^{-4} SI [23]. For purposes of calculating boundary effects, we consider the volume surrounding the tank (air and soil) to be non-conducting and non-magnetic.

A sensor in the tank starts seeing the region outside the tank at times of order $\tau = \sigma\mu_0 l^2$, where σ is the electrical conductivity of the water, μ_0 is the magnetic permeability and $l = 1.5$ m is the characteristic dimension of the tank. With $\sigma = 4$ S/m, $\tau = 0.011$ ms. Referring to Figure 34, beyond that time the background signal perturbation from the sidewalls is the same strength as the background response for an unbounded medium but of opposite sign: the region outside the tank is driving the response. This suggests that we should not see much of a background response in the tank with our TEM sensors, which do not provide useful data before about 0.1 ms. We did a lot of careful differencing of corresponding measurements taken in air and in water and found no consistent background responses above noise levels. Figure 15 shows results for the TEMTADS sensors encased in a watertight Pelican case. There is no background response above noise levels. The TEMTADS coil in the Delrin pressure housing does not see a background response above noise level either.

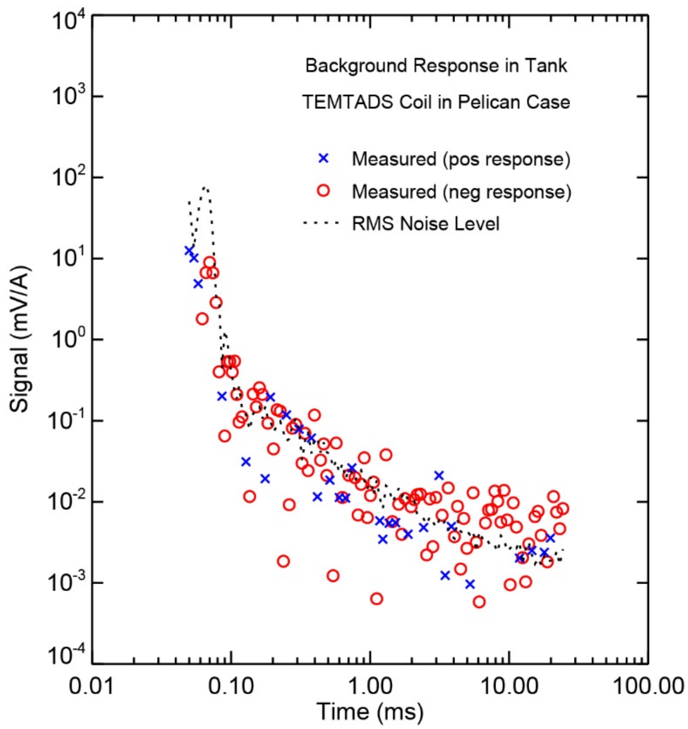

Figure 15. Background response in the tank measured with TEMTADS sensors in a waterproof Pelican case. Symbols show the measured background response obtained by diffeeencing in-air and in-water measurements, blue x's for positive signals and red o's where the difference is negative. The dashed line shows the RMS noise as a function of time gate.

Waves on the surface of the water are a potential source of noise because the background response varies with the distance between the sensors and the surface, especially at early times. We used a large Styrofoam block as a plunger to resonantly excite waves in the tank. Figure 3(f) is a photograph showing the waves during one of the test runs. The crest-to-trough wave height is about 30 cm, and the wave period is roughly 1 s. Figure 16 compares the RMS variability of the background response when there are surface waves in the tank (solid curve) and when the tank is quiescent (dashed curve). In each case the RMS background variability was calculated from a roughly 20 s series of background shots at 0.1 s intervals (25 ms decays with no stacking) using the 68 cm (exposed) transmit coil. There is no significant difference with and without waves. As noted above, in the tank the background response is very weak at best. Furthermore, the waves are necessarily short-crested and have relatively short wavelengths due to the size of the tank and the way in which the waves were produced. At times of order 0.1 ms the EMI response tends to average over scales of about 4½ m. This is significantly greater than the surface wavelength in the tank, smoothing out any effect of the waves. Longer waves and swell on a natural body of water would likely have a more noticeable effect.

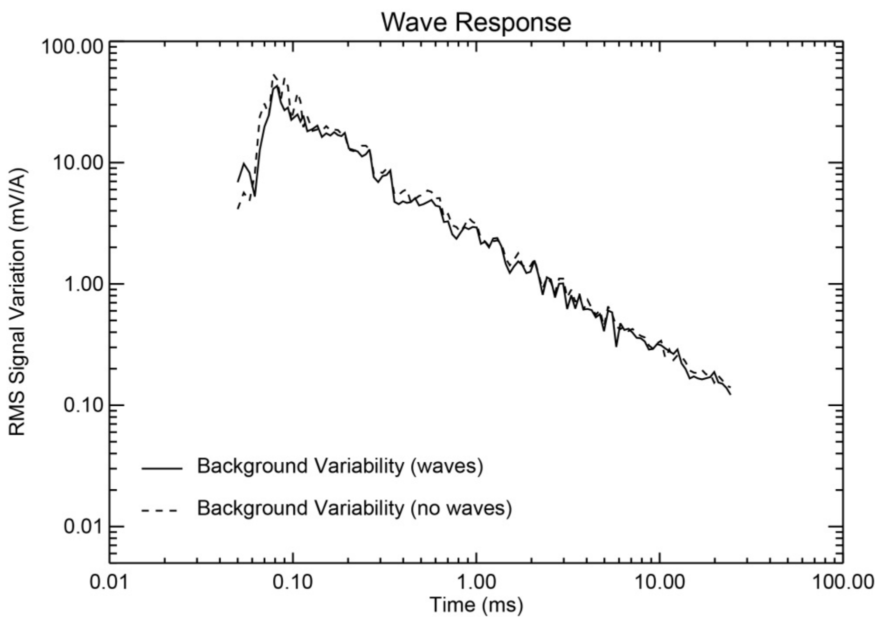

Figure 16. RMS background variability in quiescent tank (dashed line) and with surface waves (solid line).

Target Response

A salt water environment distorts a target's EMI response relative to the response on land. This distortion is due to: (a) attenuation and phase shifts experienced by the primary and secondary magnetic fields when the surrounding medium is electrically conducting and (b) electric field contributions to the response. The latter effect arises because changes in the magnetic field of the transmit coil create electric fields and associated currents in a conducting medium. With a circular transmit coil, the electric field lines form circles around the coil axis, as opposed to the magnetic field lines which thread the coil. The geometry is distorted if the coil is rectangular, but the basic picture is unchanged. The electric field is strongest in the plane of the coil and weakest directly above and below the coil, again as opposed to the magnetic field which is strongest directly above and below the coil. Currents driven by the electric field in the seawater will interact with any nearby target, inducing an electric field signal (the current channeling response) in addition to the magnetic field signal from eddy currents induced in the target by the primary magnetic field. The current channeling effect is similar to how magnetic flux is gathered or channeled by a magnetically permeable object: the currents flowing in the salt water are gathered or channeled into the conducting object. This induces a secondary electromagnetic field component which adds to the signal at the receive coil.

EMI target responses are distorted in a conducting medium, but at ranges out to a meter or so the effects of the conducting background on the target response are limited to decay times of order $\tau \sim 0.01$ ms. Because of variability in the early time ring-down, TEMTADS-type coils and electronics generally do not give reliable measurements of the response in air or in water for decay times much earlier than about 0.1 ms, so we do not expect to see much distortion due to propagation effects. EMI responses for a variety of test objects – spheres, spheroids, cylinders and inert ordnance items – were measured in the tank and compared with corresponding responses measured in air beside the tank. Test setups involved placing targets at various positions along a rack fixed above the sensor or in a holder attached to the grate and repeating measurements with the target in place and removed with everything in the tank and again with everything pulled out and set on blocks beside the tank. Some of the test geometries were chosen to focus on electric field effects. Results from these are presented in the subsection on electric field response directly below. The response to electric fields in the water tends to be weak compared to the standard eddy current response associated with magnetic fields from the transmit coil and restricted to early times. For most of our tests we saw no significant, repeatable differences between the responses measured in air and in water. These results are summarized in the subsequent subsection on magnetic field response.

Electric Field Response

Since the electric field is strongest in the plane of the coils, we looked for electric field effects using sensor-target geometries like that shown in Figure 3(e). Results of one simple test are shown in Figure 17. It compares the responses in air and in water for a pair of 6.67x6.67x20 cm spheroids, one aluminum and one steel. The conductivity of the water was about 4 S/m. Red dashed curves show the response (background subtracted) in air and dark blue curves show the corresponding response in water. The responses were measured with the Z-axis receiver of a bistatic cube displaced 35 cm from the center of a standard TEMTADS transmit/receive pair in the large pressure housing. The target is 30 cm from the center of the receive cube and the geometry is roughly co-planar. The RMS noise (based on shot-to-shot background response differences in water) is shown by the dotted curve. The responses in air and in water for the steel target are indistinguishable, but there is a clear difference above noise from about 0.07 ms to 0.5 ms between the responses in air and in water for the aluminum target. The light blue curve shows the in-water response for the aluminum target when it was wrapped in a plastic bag to suppress any channeling of currents through the target, and it is indistinguishable from the response in air.

We have repeated this test with different targets (various spheres and oblate as well as other prolate spheroids) and with slight variations on the geometry. We have consistently come up with the same result. For bare aluminum targets the response in water differs from the response in air at early times. The air-water difference goes away when the target is electrically insulated from the water by wrapping it in a thin plastic bag. A similar effect was observed in tests with wrapped and bare targets conducted for SERDP Project MR-1321 with a frequency-domain sensor [24]. We do not see a comparable effect with bare steel targets.

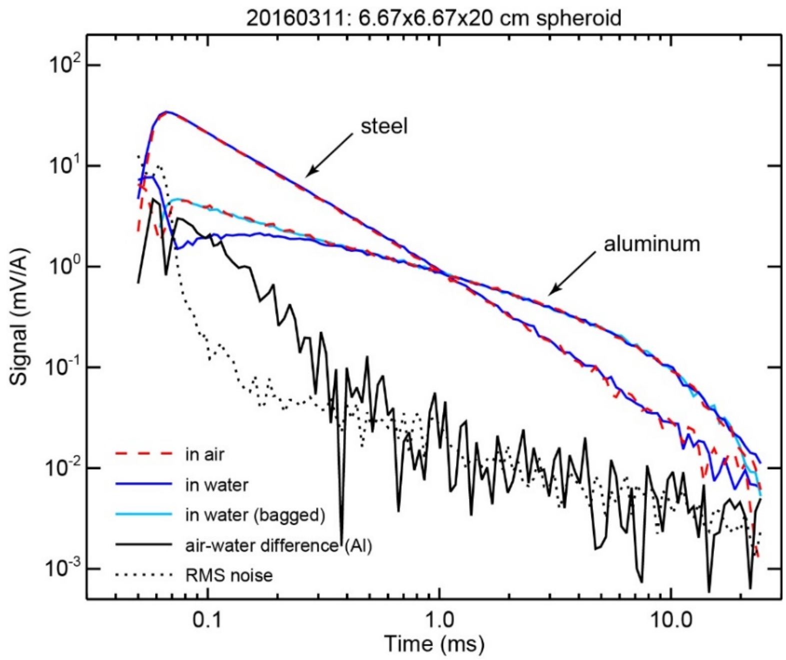

Figure 17. Responses in air and in water for aluminum and steel spheroids. See Figure 3(e) for geometry. The light blue curve shows the in-water response for the aluminum target when it is wrapped in a plastic bag.

This electric field effect is sometimes referred to as the current channeling response [24]. It exists because the water conducts electricity and the electric field creates background currents in the water. If the target is a good conductor and is in electrical contact with the water then these currents are channeled through the target much like the magnetic flux is concentrated by a magnetically permeable target. In order to verify the electric field scaling for this effect, we measured responses of a similar but larger (10x10x30 cm) aluminum spheroid on a rail centered 21 cm above the sensors. The 3-axis mono-and bistatic responses in air and in water were measured with the target at horizontal ranges of 41-91 cm from the center of the transmit coil (6-56 cm from the center of the bistatic receive cube) in 10 cm increments. The target orientation was the same as in Figure 3(e), so the electric field is aligned with the long axis of the target. The outboard receive cube was rotated by about 10° relative to the transmit/receive pair so there is a slight mixing of transverse and axial responses for the bistatic X- and Y-axis signals.

In direct analogy to the standard eddy current response [25] we may represent the response to the electric field in terms of a polarizability tensor ($\boldsymbol{\mathcal{P}}$). The voltage signal at the receiver is then given in terms of the transmit current I_0 and the conductivity of the water σ by

$$V(t) = \sigma\mu_0^2 I_0 \boldsymbol{G}_R \cdot \left(\boldsymbol{G}_T \frac{d\boldsymbol{\mathcal{P}}}{dt}\right)$$

plus whatever gain factors accrue from multi-turn coils, pre-amps, *etc.* $\mu_0 = 4\pi \times 10^{-7}$ Vs/Am is the background permeability, while $\boldsymbol{G_R}$ and $\boldsymbol{G_T}$ are receive and transmit coil response functions

$$\boldsymbol{G}(\boldsymbol{r}) = \frac{1}{4\pi}\iint \frac{\boldsymbol{r} \times d\boldsymbol{A}}{r^3},$$

where $\boldsymbol{r}$ is a vector from the transmit or the receive coil to the target and the integral is over the area enclosed by the coil. Details are in the first Appendix in the section on electric field effects. Published analyses of current channeling effects for underwater EMI have assumed that the target is a perfect conductor [26, 27]. That may not be an apt model for interpreting our results; it certainly is not for the eddy current component. For that we need to use a model which properly accounts for the diffusion of the fields into the target after the primary field cutoff [28].

That said, if we are indeed dealing with electric field effects, then we can determine the polarizability empirically by inverting the air-water response differences from the rail data and examine the residuals for consistency with the basic model. Figure 18 compares the rail data with the electric field model. The plot on the left shows the polarizability extracted from the data. The solid portion of the curve highlights the time range 0.07-0.5 ms, where we think that the signal to noise ratio supports the analysis. The plot on the right compares the measured signal strength

$$\frac{V}{I_0 d\mathcal{P}/dt}$$

for the time interval 0.07-0.5 ms with the signal strength

$$\sigma\mu_0^2 \boldsymbol{G}_R \cdot \boldsymbol{G}_T$$

calculated using the electric field response model. The model does not take into account any effects of the tank walls or the water surface. However, the data do appear to be consistent with the model. This would not be the case for the magnetic field (eddy current) model, where the coil response function is

$$\boldsymbol{C}(\boldsymbol{r}) = \frac{1}{4\pi}\int \frac{d\boldsymbol{s} \times \boldsymbol{r}}{r^3}.$$

Here the integral is around the loop rather than over the area enclosed by the loop [25]. Contributions from opposite sides of the loop tend to cancel so that the numerator depends more on the size of the loop than the distance to the target, leaving an overall r^{-3} dependence on range which is strongest above and below the loop. With the electric field response function the numerator scales with range, resulting in an overall r^{-2} dependence which is strongest off to the side.

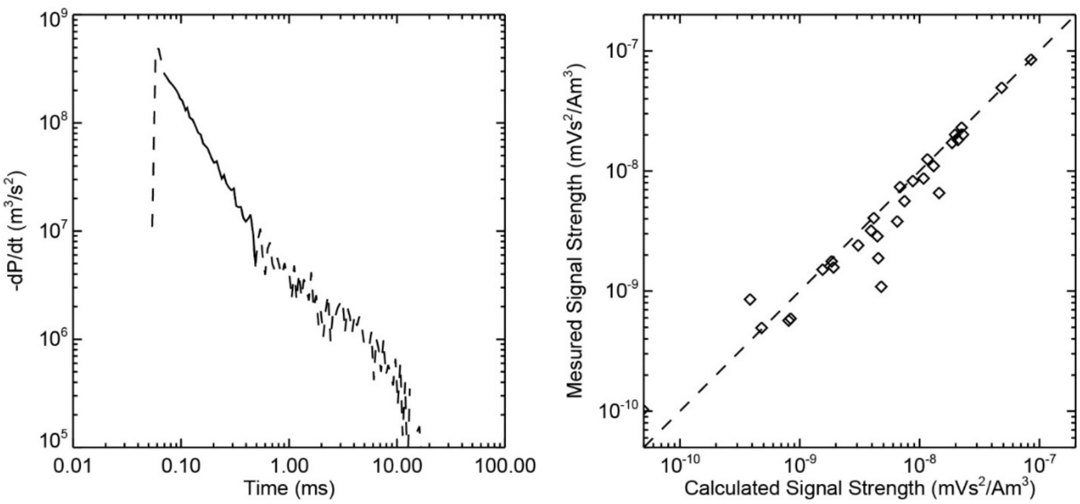

Figure 18. Electric polarizability for 10x10x30 cm aluminum ellipsoid calculated from rail data (left) and measured *vs.* calculated signal strength (right).

Magnetic Field Response

We collected mono- and bistatic multi-axis target response data in air and in water for a variety of test objects (40mm and 90mm projectiles, 81mm and 3-in Stokes mortars, aluminum and steel spheres, cylinders and spheroids). In most cases there was no discernible difference between the responses in air and in water. Figure 19 - Figure 22 show examples for different targets and test setups. In-water responses (with the background response subtracted) are shown by the solid curves and corresponding in-air responses by the dashed curves. The convention in these plots is that blue curves denote positive signals while red curves denote negative signals. In each figure, the top row shows the Z-axis response, the middle row the X-axis response, and the bottom row the Y-axis response. Examples of test setups are pictured in Figure 3. The particular test setups for each of the measurements shown in Figure 19 - Figure 22 are described in each of the figure captions. Except for measurements where the actual shape of the response is especially sensitive to small air/water target positioning differences, the responses in air and in water are the same. The exceptions are found in the lower right plot in Figure 19 and in the middle left and lower right plots in Figure 20. In these cases, the response involves a balance between oppositely-signed axial and transverse polarization components whose respective strengths vary with target location. For the in-water measurements, the target was lowered onto the rack by a string. The rack has notches for positioning along its length, but with the large ordnance items the cross-rack positioning is not precise enough to precisely capture this balance.

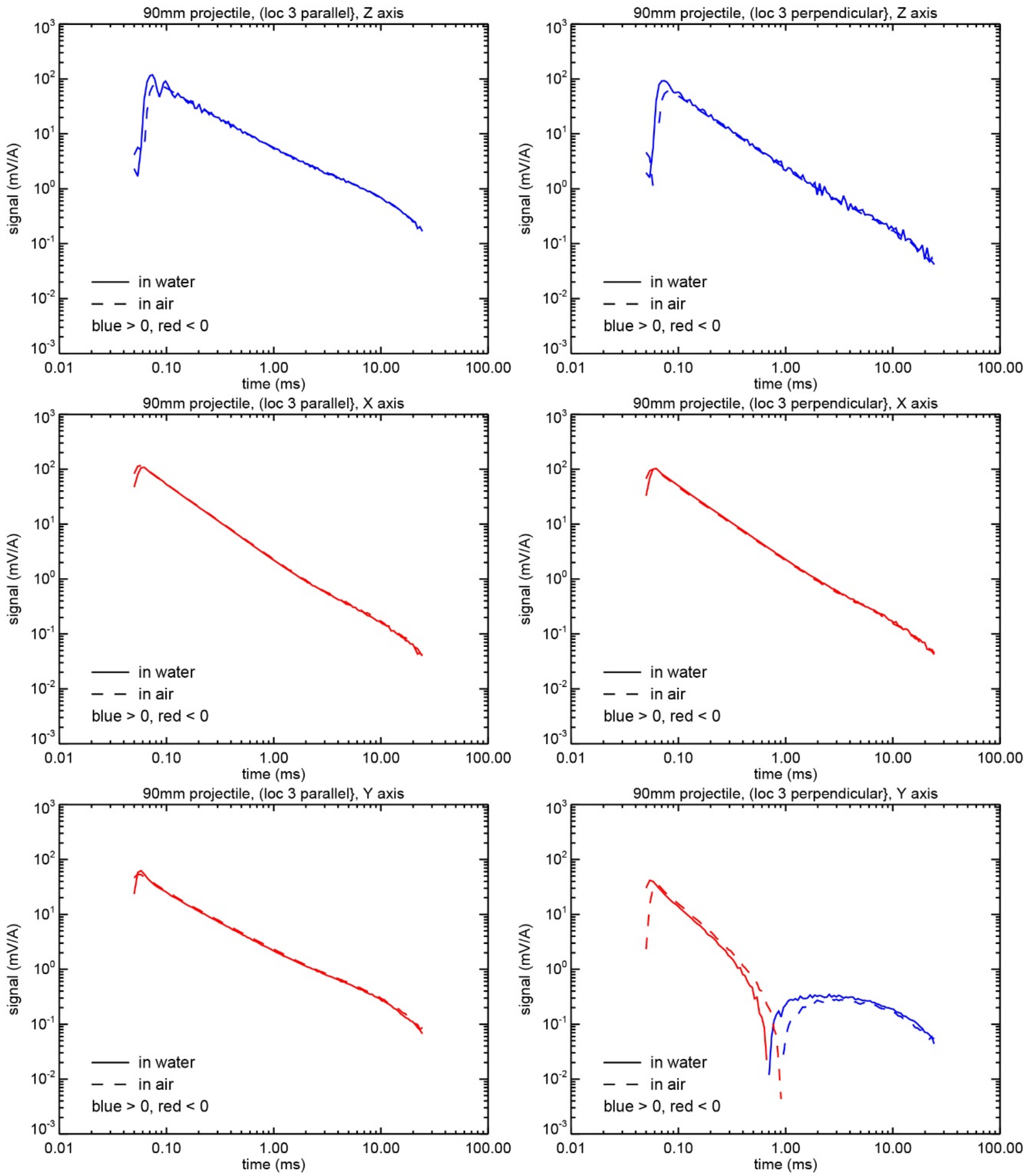

Figure 19. 90mm projectile response data collected using the medium rectangular Tx coil with a standard 3-axis Rx cube. Solid and dashed curves show the in-water and in-air responses, respectively. The target was positioned on a rack 50 cm above the coils. The test setup is shown in the upper left photo in Figure 3. Parallel and perpendicular refer to the target orientation relative to the rack.

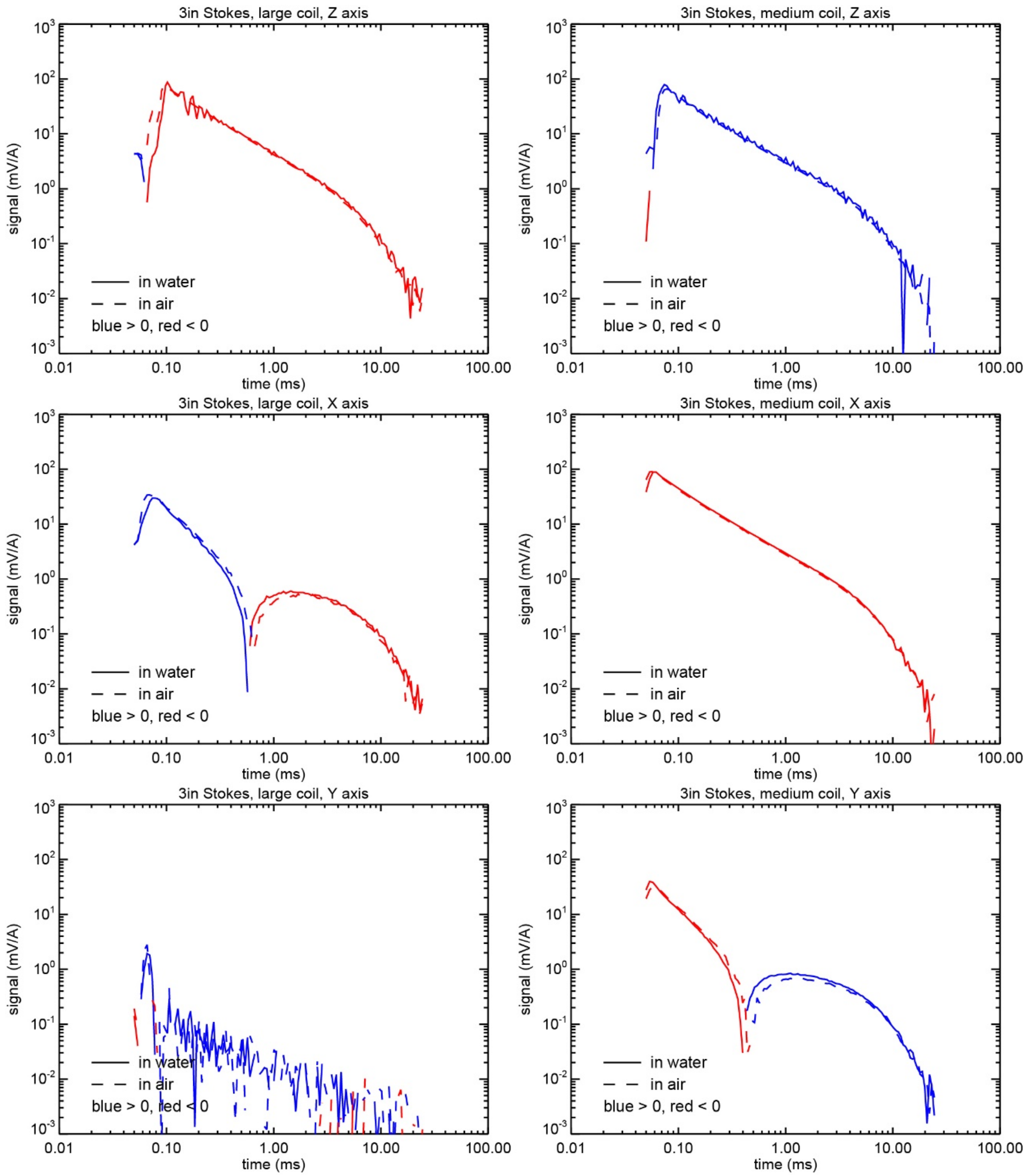

Figure 20. Response data for a 3-in Stokes mortar collected using the medium rectangular Tx coil (right column) and the large Tx coil (left column) with a standard 3-axis Rx cube. Solid and dashed curves show the in-water and in-air responses, respectively. The target was positioned on a rack at a height of 50 cm for the medium coil and 70 cm for the large coil. The test setup for the medium coil is shown in the upper left photo in Figure 3. The setup for the large coil is similar but the mortar is at a location and orientation where the Y-axis response is very weak..

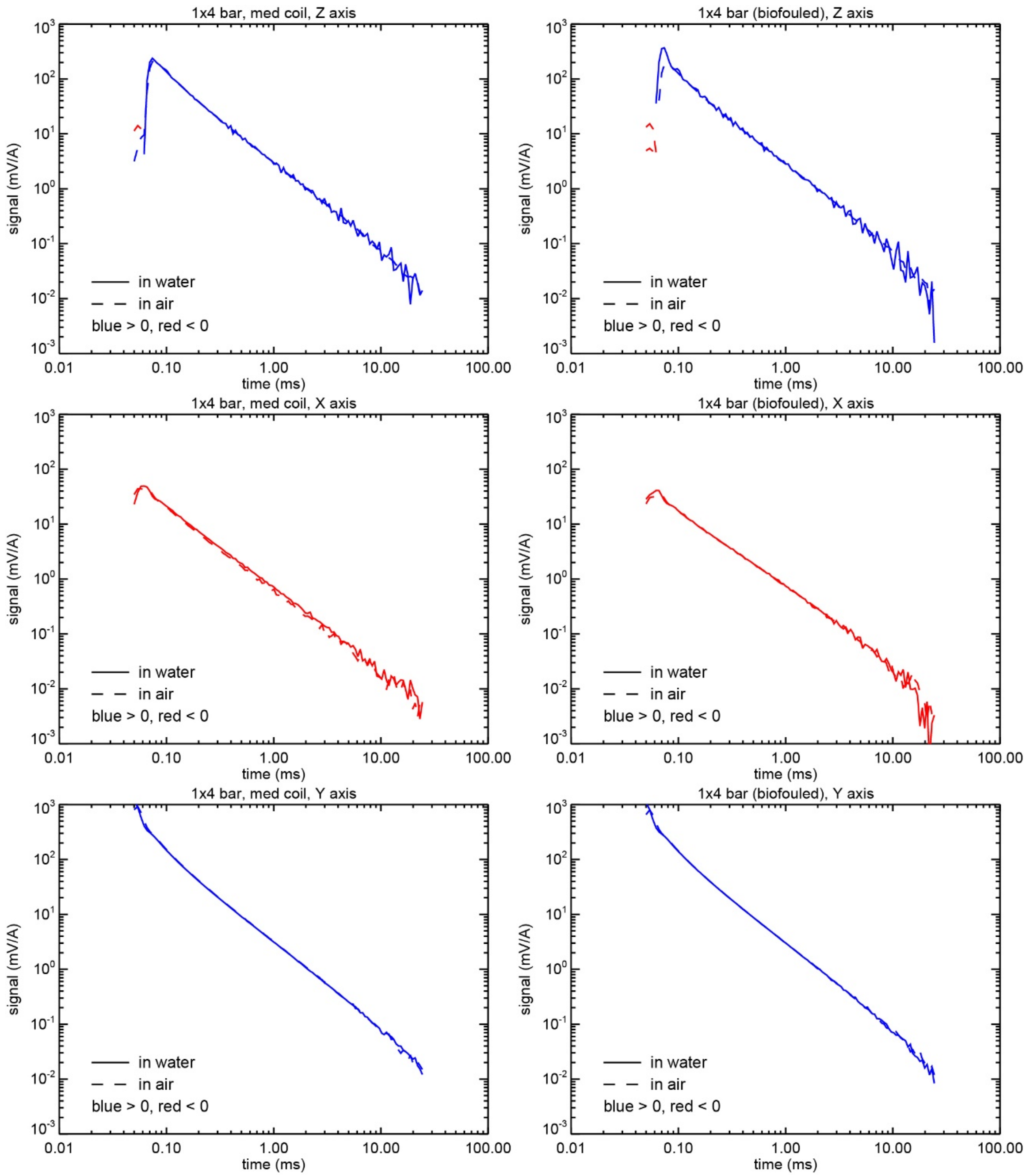

Figure 21. Response data for 1-in dia. by 4-in long steel rods collected using the medium rectangular coil with a standard 3-axis Rx cube. Solid and dashed curves show the in-water and in-air responses, respectively. The test setup is shown in the middle left photo in Figure 3. The responses on the left are for a bare, sanded bar and those on the right for the bio-fouled bar shown in the photo.

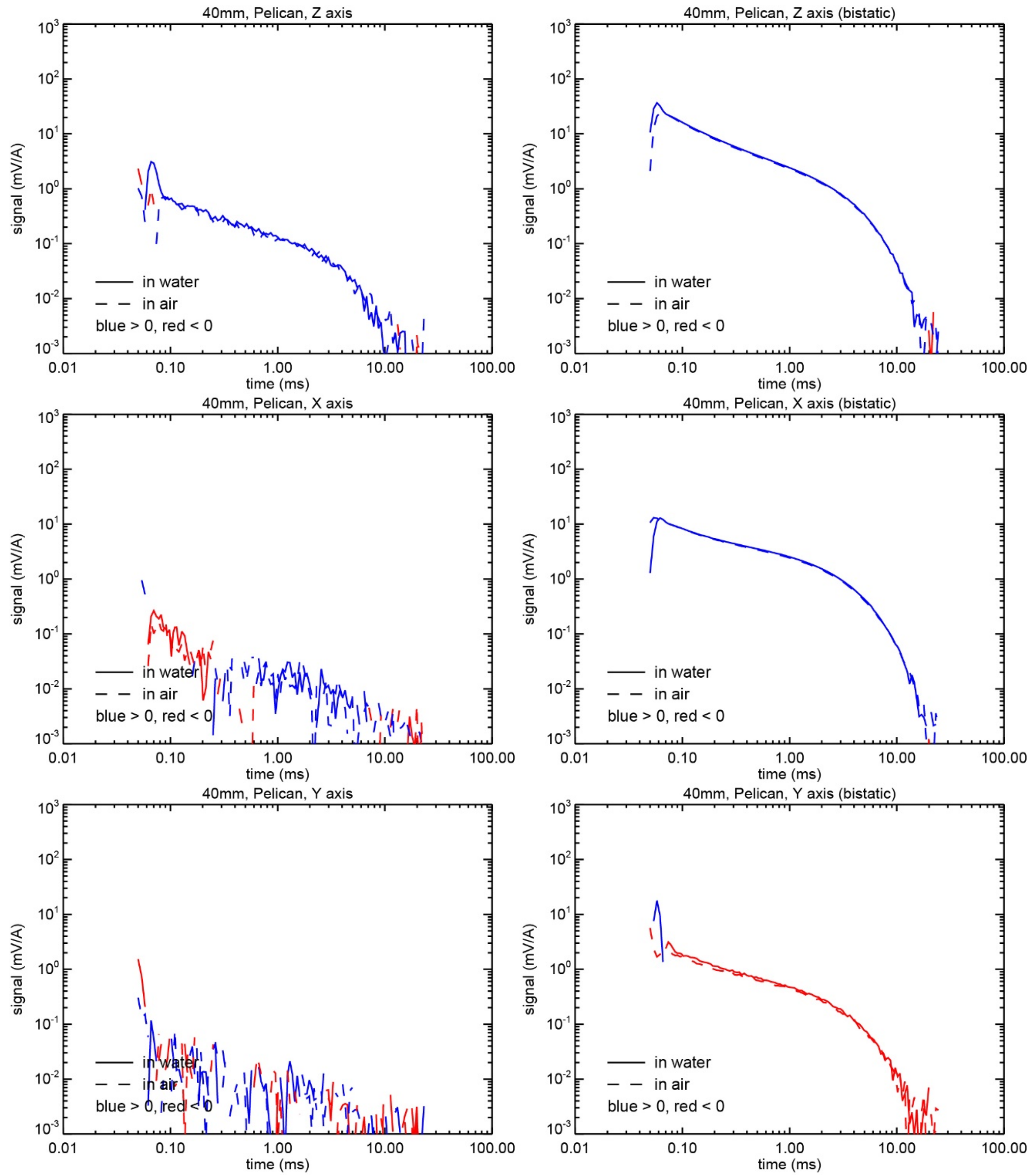

Figure 22. Bistatic response data for a 40 mm projectile collected using a standard TEMTADS Tx/Rx cube pair and a separate Rx cube offset 40 cm. Both were in Pelican cases. Solid and dashed curves show the in-water and in-air responses, respectively. The target was in a PVC cup outboard of the bistatic Rx cube. The monostatic response is shown on the left and the bistatic response on the right.

Differences between measured responses in air and in water for a cross-section of targets and test geometries are plotted *vs.* signal to noise ratio (SNR) in Figure 23. We have only included data from tests which were not specifically targeting the electric field response. The air-water signal difference is the average over time gates t_i from 0.1–10 ms of the ratio of the magnitude of the difference between (background subtracted) target responses in air and in water to the magnitude of the response in air:

$$\delta_{AW} = \frac{1}{n}\sum_{i=1}^{n} \frac{\left|\frac{1}{\alpha}\{S_W(t_i) - B_W(t_i)\} - \{S_A(t_i) - B_A(t_i)\}\right|}{|S_A(t_i) - B_A(t_i)|}$$

where S_A and S_W are measured target responses in air and in water, and B_A and B_W are corresponding background responses in air and in water. To compensate for small variations in positioning of the target between in-air and in-water measurements, the target response in water is scaled. The scaling parameter α is the median (over time gates) value of the ratio of the amplitude of the response in water to that in air:

$$\alpha = median_{(i)} \left\{\frac{S_W(t_i) - B_W(t_i)}{S_A(t_i) - B_A(t_i)}\right\}.$$

This scaling is the same as that used in our standard classification algorithm [29]. These adjustments are generally very small: the median air-water amplitude difference is 4.3% for the data in Figure 23. The signal to noise ratio is the magnitude of the average over time gates of the ratio of background corrected signal to the standard deviation of the background responses at each time gate:

$$SNR = \left|\frac{1}{n}\sum_{i=1}^{n} \frac{S_W(t_i) - B_W(t_i)}{stdev\{B_W(t_i)\}}\right|.$$

The dashed line in Figure 23 shows the relationship $\delta = 1/SNR$, which is what one would expect if there is no significant distortion of the signals in water. With the exception of the very low SNR data and a cluster of outliers with SNR values ranging from about 10 to 50, the data appear to follow this trend. The outliers correspond to measurements where the actual shape of the response is especially sensitive to small air/water target positioning differences. Examples are those shown in the lower right plot in Figure 19 and in the middle left and lower right plots in Figure 20. In these cases, the response involves a balance between oppositely-signed axial and transverse polarization components whose respective strengths vary with target location. For the in-water measurements, the target was lowered onto the rack by a string. The rack has notches which fixed the location of the aluminum ball quite well, but with the large ordnance items the positioning lacks the same precision.

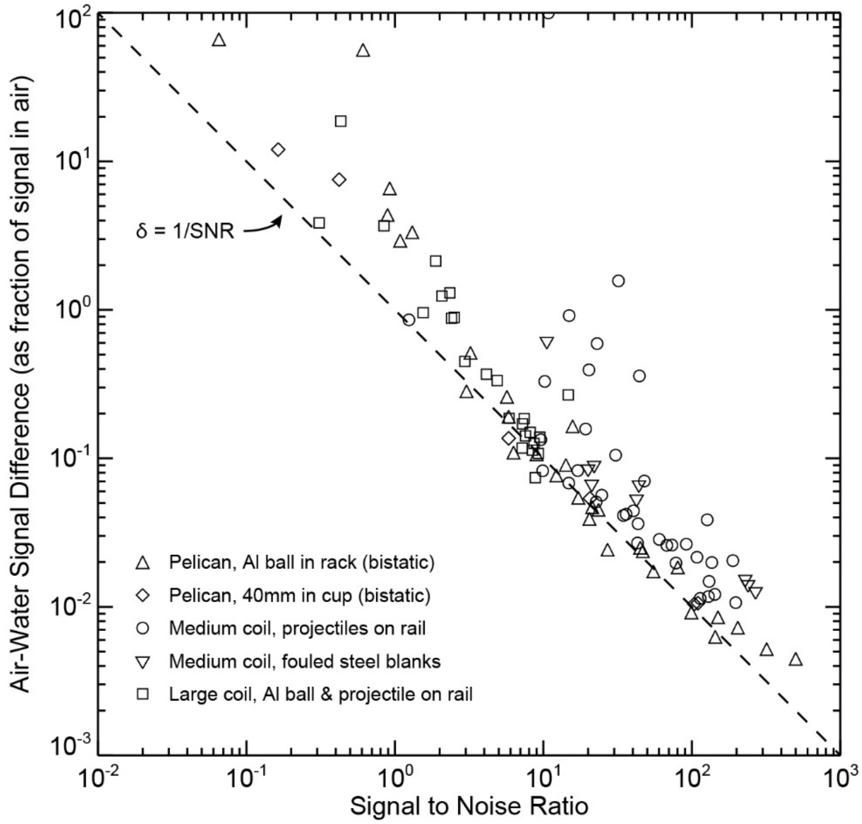

Figure 23. Deviations between in-air and in-water target response as a function of signal to noise ratio.

Field Tests

R/V Hull Interference

Most of the EMI data were collected from the R/V Elis Olsson which has a steel hull. Initial tests with the TEM sensors floating on the surface at various distences from the R/V suggested that the influence of the Olsson's hull on the EMI measurements would not be significant. We took the R/V Heron, which has a fiberglass hull, out for the final data collection, and found that in fact near-surface EMI data collected from the Elis Olsson had been affected by the hull. Figure 24

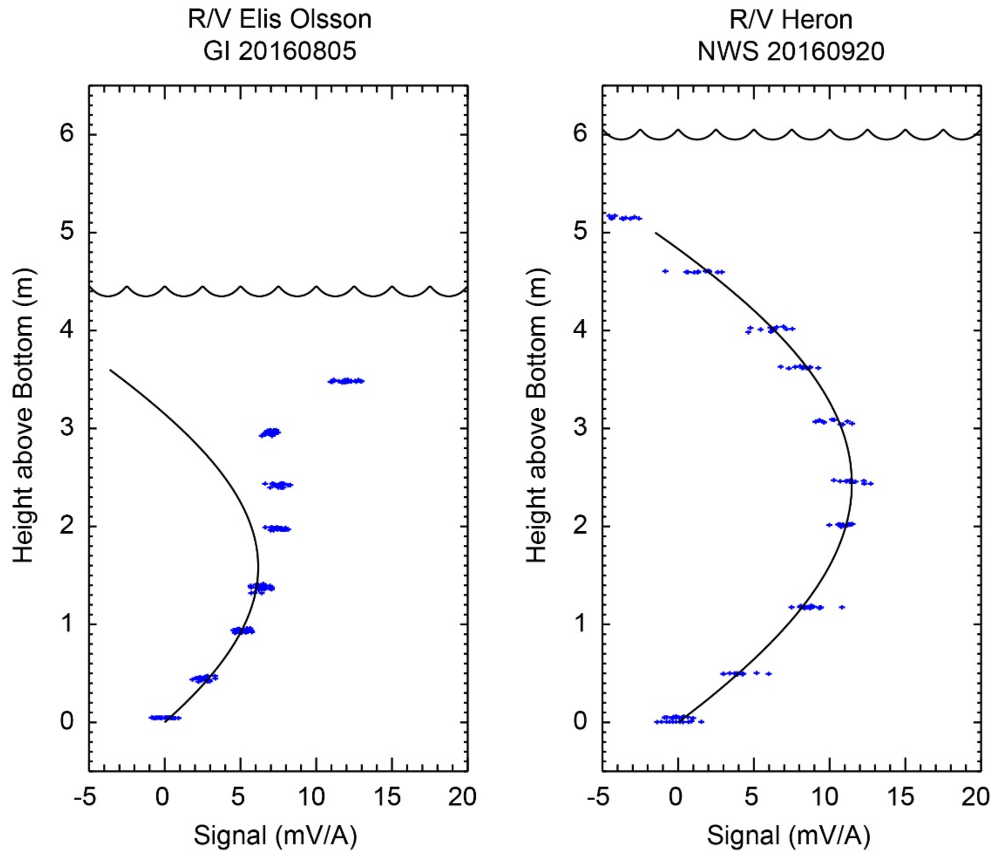

Figure 24. Background response *vs*. depth data collected from the R/V Elis Olsson (left) and the R/V Heron (right).

compares background response data at 0.1 ms decay time collected from the two R/Vs. The data from the Elis Olsson is on the left and the data from the Heron is on the right. Data points are one second signal averages. For comparison, the signals are referenced to 0 mV/A at the bottom. The wavy line at the top of each plot represents the water surface. The curves show the expected response *vs.* depth calculated using the models described in the first Appendix. We start seeing signal contributios from the steel hull when we the sensors are within about 3 m of the surface. There is no obvious effect from the R/V Heron's hull. EMI sensors must be near the bottom (~1.5 m) to reliably measure the response of munitions targets on or buried in the bottom. We are primarily interested in the background response in this regime. Referring to Table 3, with the exception of the Pamunkey Sand site the water depths were all greater than 4 m, so we expect that the background response data in the bottom 1.5 m of the water column are generally reliable.

Background Response

The background response near the bottom at 0.1 ms decay time for all of the sites is plotted in Figure 25. From left to right the plots are for the X-, Y- and Z-axis response. Blue symbols are for the monostatic response, red symbols are for the bistatic. The horizontal lines through the data points show the RMS noise (±1 standard deviation). In each plot the data are referenced to 0 mV/A at the bottom to eliminate the background contribution from the sensor and its electronics. The Clay Bank (CB) data are suspect. There is an obvious anomaly at 1.3 m above the bottom in the first cast, and in the second cast the monostatic X- and Z-axis responses are comparable, which should not be the case.

There is a clear background signal in the Z-axis (aligned with the Tx coil axis) response at the higher salinity sites (GP, FP, GI, NWS), but none in the orthogonal axes. There are a few exceptions. One or two of the profiles at WP, PM and PS show horizontal axis responses comparable to vertical in the bistatic response. Curiously, these are the stations with the strongest currents (see Figure 8, right). In general, the monostatic and bistatic signals are comparable. The

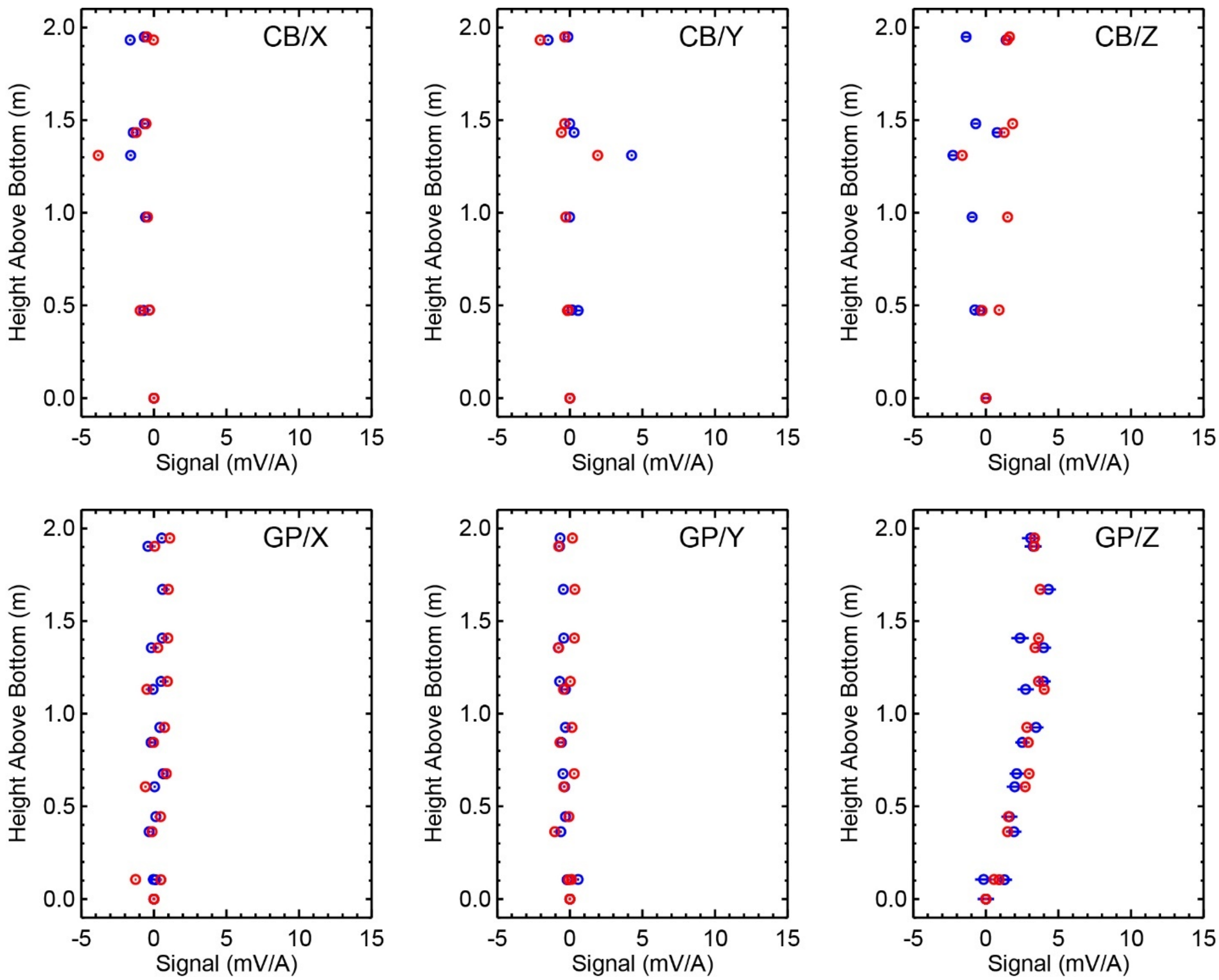

Figure 25. Near-bottom X-, Y- and Z-axis background response at 0.1 ms decay time for the CB and GP sites. Blue symbols are monostatic response, red symbols bistatic. Horizontal lines through data points show RMS noise.

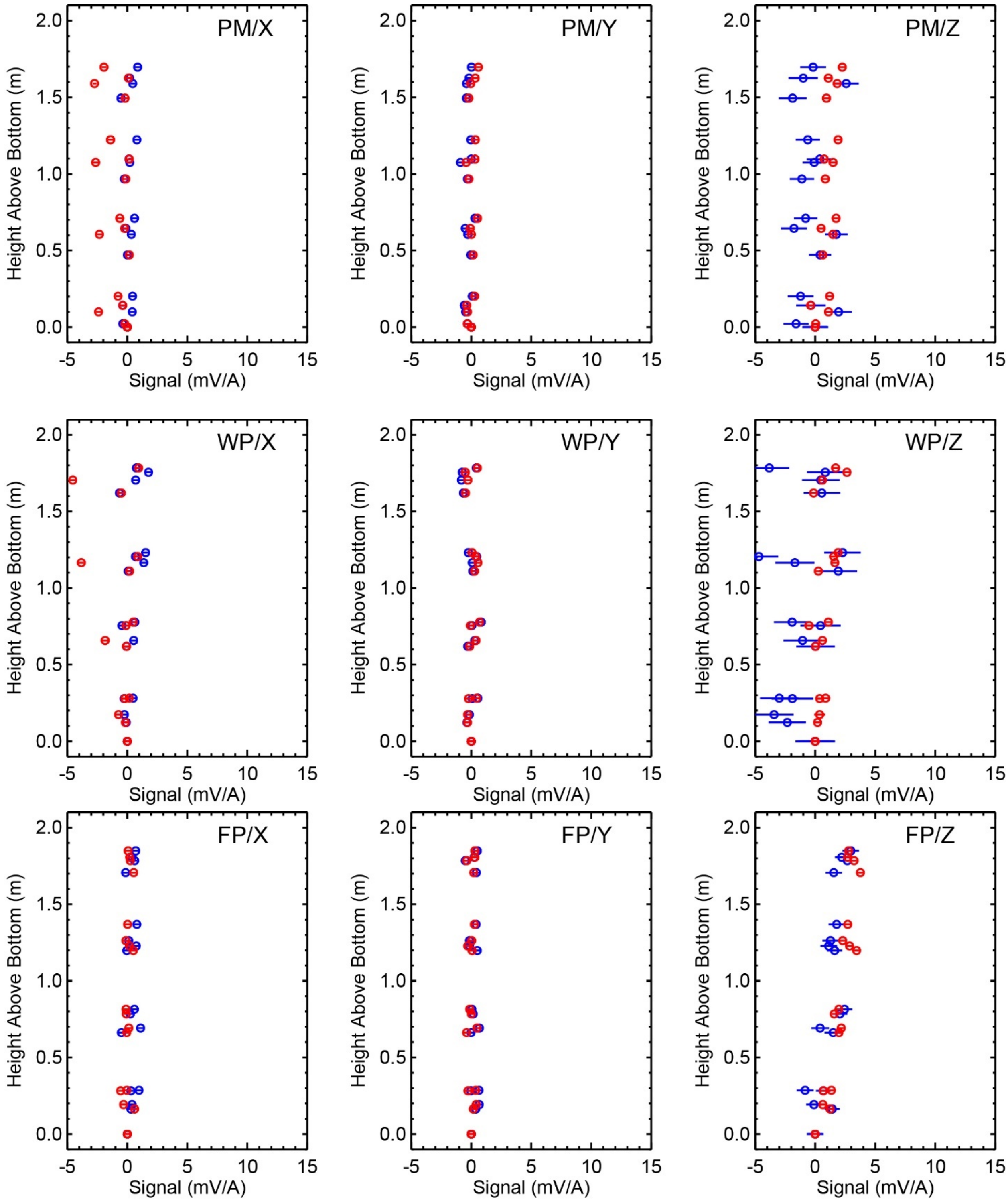

Figure 25, Continued. PM, WP and FP sites.

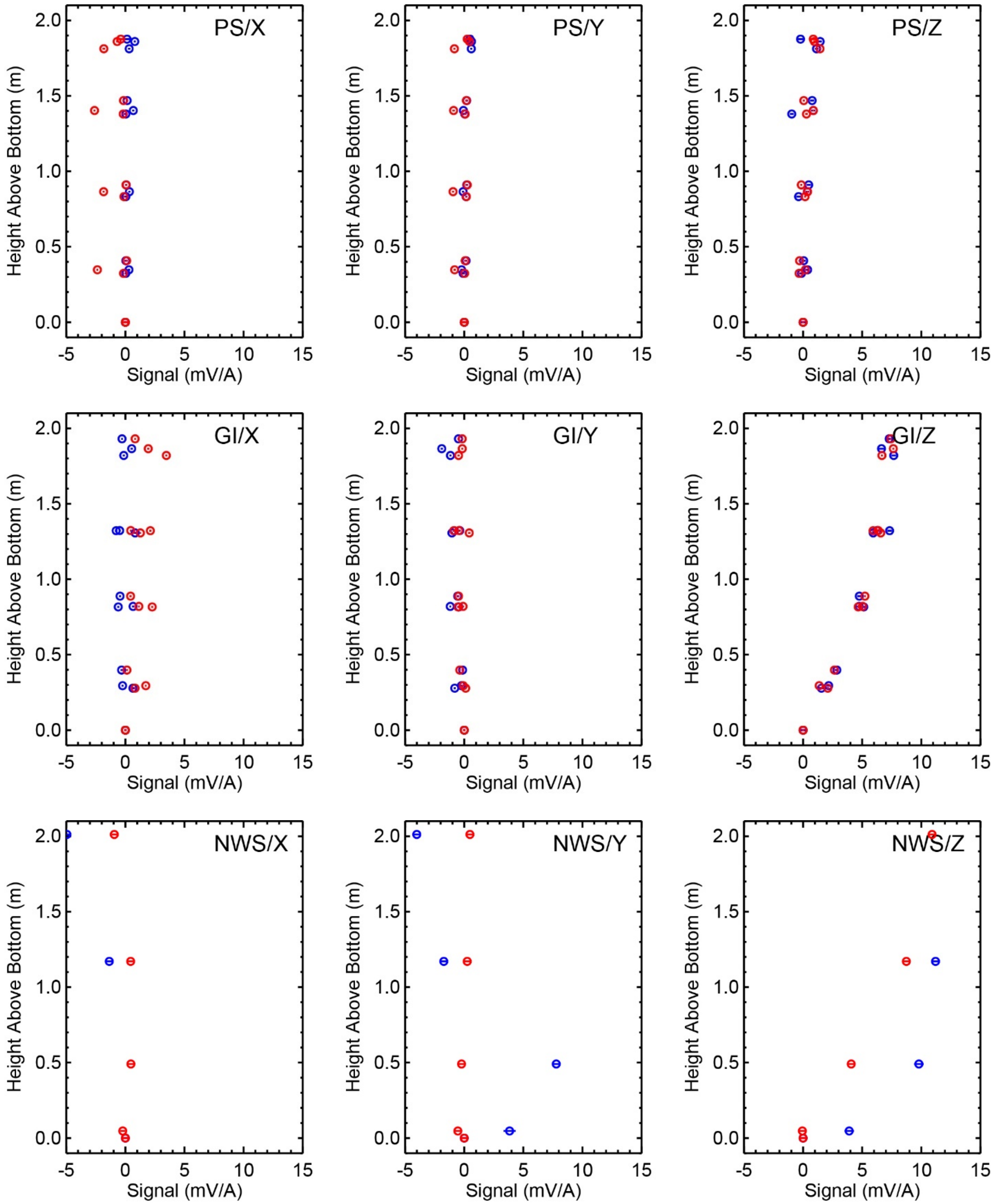

Figure 25. Continued. PS, GI and NWS sites.

main exception is NWS. There had been a long break prior to that data collection, and the state of the Tx/Rx pressure housing was not verified prior to use. When it was opened later we found that there had been a water leak. This appears to have affected data from the co-located Rx cube (note the X- and Y-axis monostatic responses). The bistatic data seems okay. Typically the signal *vs.* depth profiles show concave curvature to the left with height above the bottom. The PS profiles show convex curvature, likely due to hull interference from the R/V Elis Olsson. PS was the shallowest site, with an average depth for the TEM profiles of just 3.86 m.

For the remainder of this section, we focus on the near bottom gradients of the background response. As noted above, the measured response includes contributions from the sensor and its electronics as well as the background environment. The first is not fixed, but variable [30 ,31]. It can’t be known a priori to the necessary accuracy and must be measured in real time. When EMI sensors are used for munitions classification on land this background has to be subtracted out in order to reveal the munitions signature. This entails either taking background measurements at “clean” locations when static cued data are being used or by using a running median from apparently clean sections when dynamic survey data are being used. Here, we do not have a “clean” place to measure the sensor background. By differencing measurements taken closely together in time we can cancel out the sensor’s inherent background signal. For towed underwater sensors the background gradients are interesting in themselves since there is usually some up and down motion along the sensor trajectory. This will be addressed in a later section.

The background response decays rapidly with time. Figure 26 shows the decay of near bottom background response gradients from the four casts at the Gloucester Point (GP) site. The monostatic Z-axis response is on the left and the bistatic Z-axis response on the right. Blue curves are the background response gradient from ~10 cm to ~90 cm above the bottom. The gradient is positive in the solid portions of the curves and negative in the dashed portions. The red curves show RMS noise levels. The black curves show a t^{-4} decay, adjusted for the standard 0.028 ms delay in the TEMTADS sensors’ response. These curves are the same in both plots. The bistatic response is less noisy than the monostatic response. It is also less affected by ringdown at very early times. The t^{-4} decay is significantly faster than the $t^{-5/2}$ decay in an unbounded conducting medium (see the first Appendix). Based on our models, this type of behavior is to be expected (see next section). Indeed, it was noted in [32] that in real-world bounded, structured media the characteristic $t^{-5/2}$ decay gets modified, typically resulting in a steeper decay depending on decay time, water depth, etc. Differencing the response from two points at different distances from a boundary exacerbates this.

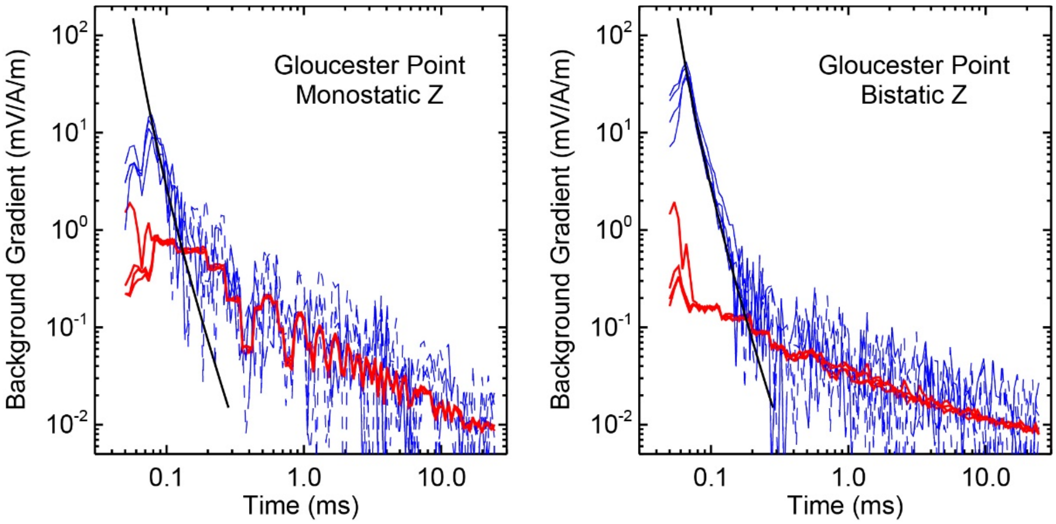

Figure 26. Near bottom background response gradients (~10 cm to 90 cm above the bottom) at Gloucester Point (blue curves). Red curves are RMS noise levels. Black curves show t^{-4} dependence adjusted for the TEMTADS sensor 0.028 ms delay.

The near bottom background response gradients at 0.1 ms and 0.15 ms at the various sites are plotted against the electrical conductivity of the water in Figure 27. The plot includes both monostatic and bistatic response for all of the sites except CB and NWS. As noted above the CB data are suspect. They show an obvious anomaly at 1.3 m above the bottom in the first cast, and in the second cast the monostatic X- and Z-axis responses are comparable, which should not be the case. The NWS site is deeper than the others, which increases the near bottom gradient relative to the shallower stations. This can be seen in Figure 24: the Goodwin Island (GI) and NWS sites have comparable conductivity but NWS is deeper than GI (6 m vs. 4.4 m) and has a stronger background response. At sites included in Figure 27, the depths ranged from 3.9 m to 4.4 m with an average of 4.2 m. Although there is a considerable amount of scatter, especially at the noisier sites (WP and PM), the trend of increasing background response with conductivity is obvious. The curves show three layer (air-water-sediment) model results for a nominal 4.4 m depth and 75% conductivity contrast between the water and the sediment. This is good enough to reproduce the general trends but, as discussed in the next section, more sophisticated multi-layer models with site-specific parameters are needed to get the details of background response variations right.

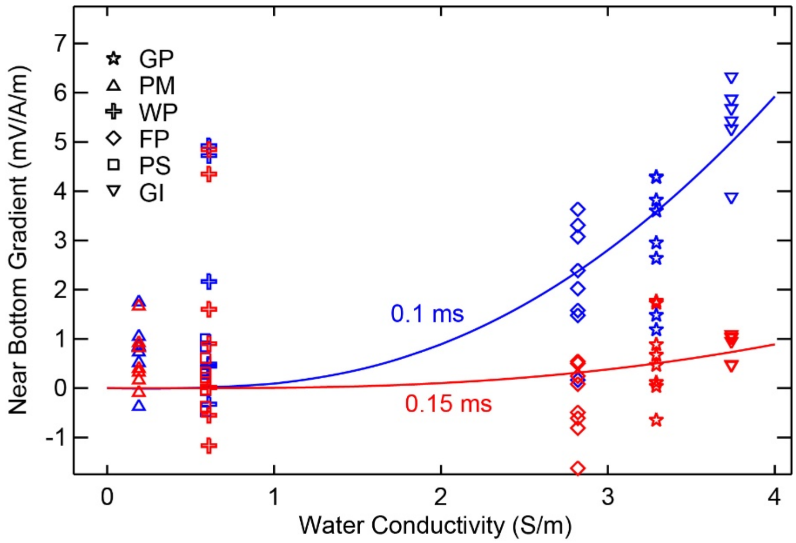

Figure 27. Near bottom background response gradient at 0.1 and 0.15 ms decay for the different test sites plotted *vs.* the electrical conductivity of the water. The curves show the expected variation with a 75% conductivity contrast between the water and the sediments.

Model Comparison

Standard practice in EMI inversion to determine sediment properties employs multi-layer models which can account for the variation in porosity, pore water conductivity and magnetic susceptibility with depth in the sediments [7, 33, 34, 42]. The derivation of the multi-layer model used here is included in the first Appendix. It accounts for the electrical conductivity and magnetic susceptibility in the air, water and sediment layers. The models can accommodate any number of sediment layers with different electrical conductivity and frequency dependent magnetic susceptibility [43] as appropriate.

The EMI data were collected from the R/V Heron at the NWS site, so for this data set we have a complete profile from the surface to the bottom. The simplest model that can accurately reproduce these data has four layers: air, water and two sediment layers. Figure 28 compares the data at 0.1 ms decay time with three (left) and four (right) layer model calculations (see the first Appendix). The red symbols are the measured background profile (in this case averages over all data collected each depth) and the curves are model calculations using a water depth of 6 m and a water conductivity of 3.75 S/m. We show results for three layer model calculations using bottom conductivities of 1.5, 2.0 and 2.5 S/m in the plot on the left. The three layer model cannot get the correct profile curvature below 3 m depth. The curve in the plot on the right shows the best four layer model fit to the data, using a least absolute deviation objective function. The sediment model that results from this inversion of the profile data consists of a 1.6 m thick layer with a conductivity of 2.5 S/m overlying a 1.25 S/m half-space.

This four layer model appears to be a good match, and is consistent with the geology. The York River overlies a deep sequence of sediment and sedimentary rock strata, the uppermost of which is a weakly cemented layer of mostly alluvial and estuarine sand and silt up to ~10 m thick, which overlies a quite firmly cemented layer of marine organism shell fragments and silty sand 40-50 m thick [4, 5]. At a decay time t, the signal from a TEM sensor near the bottom is responding to structures down to a depth $d = \sqrt{t/\pi\sigma\mu}$ below the bottom, where σ and μ are representative values of the electrical conductivity and magnetic permeability of sediments [16]. In the first few tenths of a ms we are only seeing a few meters into the 10 m thick layer of unconsolidated to weakly cemented sediments. Throughout most of the energetic parts of the estuary, physical and biological processes mix the sediments to depths of 25 - 200 cm, and the sediment porosity averages about 85% in this mixed layer [6]. Our 1.6 m upper layer probably corresponds this mixed region. The bottom sediment grab from the NWS site had 82% mud and a moisture content of 65% by weight. Assuming that the density of water is 1.015 gm/cm^3 and the sediment density is 2.65 gm/cm^3 [13], this corresponds to a porosity of 85%. Archie's Law [7, 8] is an empirical relationship which provides a useful conversion between the porosity (φ) and sediment conductivity (σ_s) for a given pore water conductivity (σ_w). To first order

$$\sigma_S = \sigma_W \varphi^m.$$

Using the value of m = 1.8 for muddy sediment [7] with a porosity of 0.83 and the 2016 average specific conductivity of 3.26 S/m from the long term monitoring site at Gloucester Point (within a few km of the NWS site). Archie's Law gives a sediment conductivity of 2.33 S/m, consistent with the upper layer conductivity (2.5 S/m) that we obtained by inverting the TEM data. In our lower layer (below 1.6 m) the 1.25 S/m conductivity would then correspond to a drop in porosity to less than 60%.

As noted previously, the background response decays rapidly in time. Figure 29, which shows calculated background response profiles for the NWS site at decay times of 0.1 ms, 0.12 ms, 0.15 ms and 0.2 ms, illustrates the trend with time.

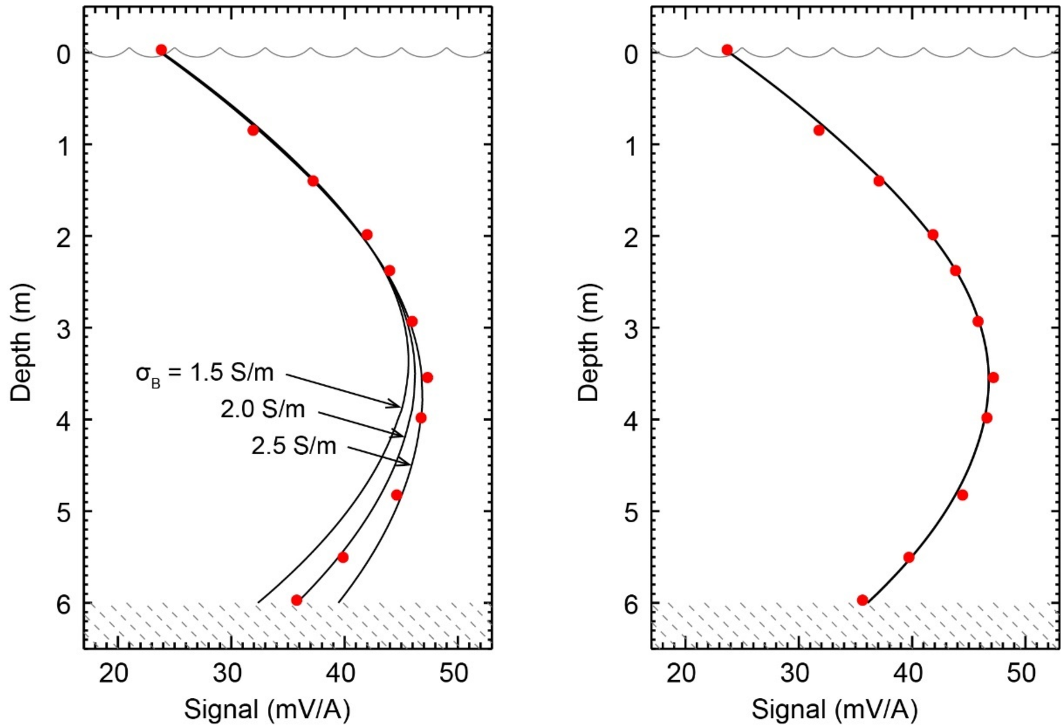

Figure 28. Measured NWS background response (0.1 ms) profile compared with three (left) and four (right) layer model calculations.

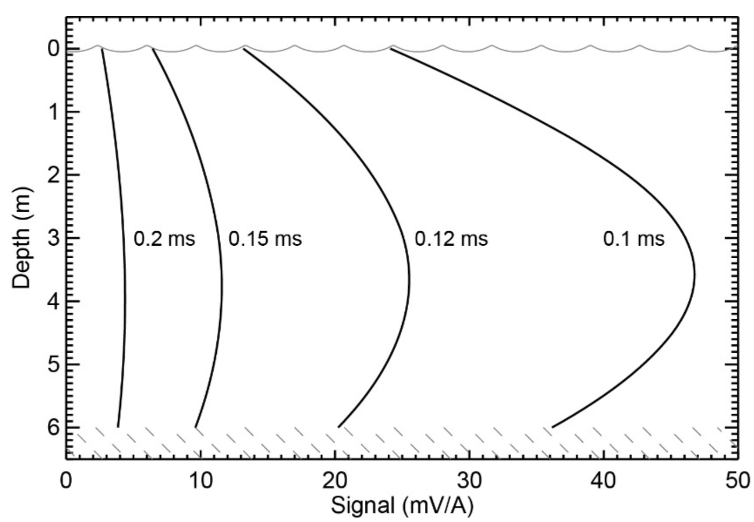

Figure 29. Calculated NWS background response profiles at decay times from 0.1 ms to 0.2 ms.

Impact on Underwater EMI Systems

If not properly compensated for, background variability of this magnitude could affect the detection and classification performance of an underwater TEM array. When EMI sensors are used for munitions classification on land, the background has to be subtracted out in order to reveal the munitions signature. This entails either taking background measurements at “clean” locations when static cued data are being used or using a running median encompassing apparently clean sections when dynamic survey data are being used. The same applies for underwater systems.

The Marine Berkeley UXO Discriminator (MBUD) system (SERDP projects MR-2228 and -2321) sought to reduce background effects by using differential receivers just as with the original BUD system demonstrated in ESTCP project MR-200838. However, with differential receivers the components of the sensing loops can change slightly in response to temperature variations and mechanical stresses on the sensor platform, and the corresponding differences of the transient signals can become a significant source of noise. Cued underwater systems such as that being demonstrated in ESTCP project MR-201313 could proceed as on land and take a background shot at some (presumably clean) location near the target to use in removing the background response. Towed systems such as the Marine Towed Array (MTA) being upgraded and demonstrated in ESTCP project MR-201610 have to deal with sensor depth variations as well as any spatial variability of the bottom in adaptively removing the background response. This is where problems could develop.

Figure 30 shows the MTA trajectory during a 400 m portion of a transect line in the Potomac River off Blossom Point, MD. The data were collected in October, 2007 during one of the ESTCP project MR-200324 demonstrations of the MTA magnetometer array [35]. The blue curve shows the MTA depth, and the hatched region shows the bottom profile. The tow speed during this portion of the transect line was 2.2 m/s. The bottom is gently sloping with a slight undulation having an amplitude of around 10 cm at a wavelength of about 100 m. Sediments at the demonstration site were described as varying from extremely soft muck that may be several feet deep, to soft or hard sand [35]. We do not have data on the electromagnetic properties of the sediments and their spatial variability, but we can estimate the background response variability due to variations in water depth and sensor height along the trajectory. Simple three layer model calculations like those used to calculate the general background response trends in Figure 27 should suffice.

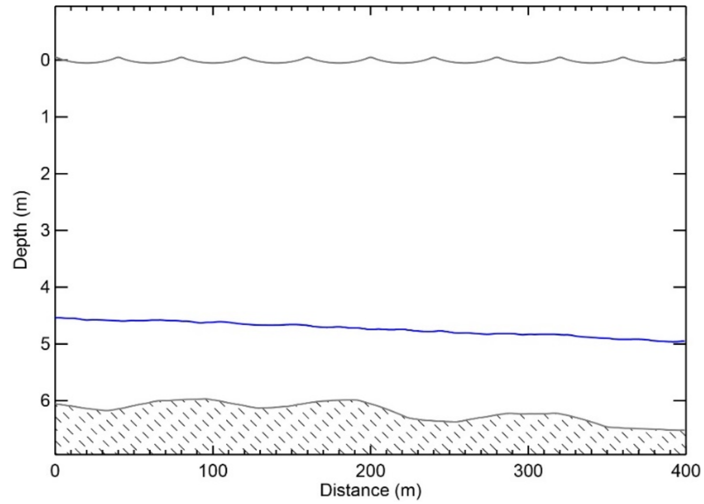

Figure 30. MTA trajectory during part of a transect line in the Potomac River off Blossom Point, MD. Blue curve shows MTA depth, gray hatched region shows the bottom profile.

Data collected duing VIMS cruises on the Potomac River during the late summer and fall of 2005 and 2006 [36] indicate that the salinity at the Blossom Point site during the time of the demonstration would be ~8.5‰, corresponding to a conductivity of ~1.3 S/m at 20° C. Surface sediment samples collected during those cruises at a site close to Blossom Point yielded ~95% mud with a moisture content of 65-70% by weight, comparable to our muddier sites on the York (see Figure 9). This is all consistent with information on this area published in the Environmantal Atlas of the Potomac Estuary [37]. We used the basic three layer model with a 75% conductivity contrast to calculate the background response for the MTA EMI array being developed in ESTCP project MR-201610, which has a large (1.06 m by 4.68 m) outer transmit coil surrounding pair of smaller (1.0 m by 2.28 m) transmit coils with six receive cubes (Figure 31). Each of the transmit coils has 24 turns with a peak transmit current of 20 A.

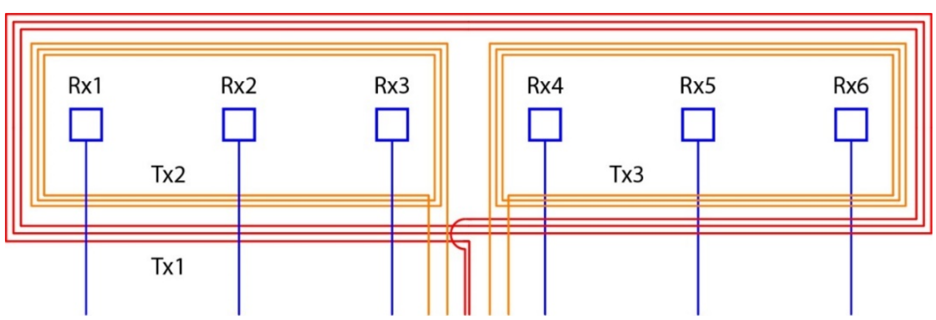

Figure 31. MTA EMI array configuration.

Figure 32 shows modeling results comparing the peak signal from a 105 mm projectile lying flat on the bottom with the variation in background response over the trajectory. The projectile passes 1.5 m below Rx 2, and the signal is the Z-axis response in Rx 2 due to Tx 2. At early times (to about 0.3 ms), the overall background variation is greater than the projectile's signal. Referring back to Figure 30, changes in depth and array height above the bottom occur on scales of tens of meters. On land, we deal with smooth variations in the background response on scales larger than the signal extent by applying a median filter to the data. Figure 33 shows the median filtered MTA EMI array background response at 0.1 ms (top) and 0.2 ms (middle) compared with the signal from the 105 mm projectile. The projectile is lying flat on the bottom at a distance of 220 m into the trajectory. The median filter is 10 m long. It reduces the signal strength by 2%. The filter removes the background response except for some hiccups at places where the array height above bottom changes of abruptly. (The bottom plot shows the array height above the bottom with the areas where there are anomalies in the filtered background highlighted in red.) Presumably these are driven by the response of MTA depth control system at these places. Correspondingly similar anomalies occur at the same places for median filtered MTA height above the bottom.

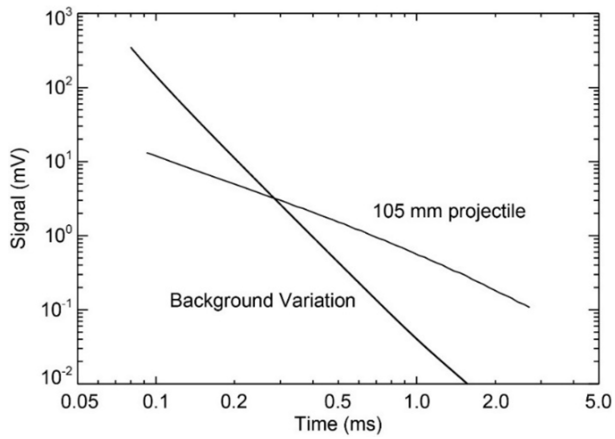

Figure 32. Model calculations comparing the MTA EMI array signal from 105 mm projectile with the variation in background response over the trajectory shown in Figure 30.

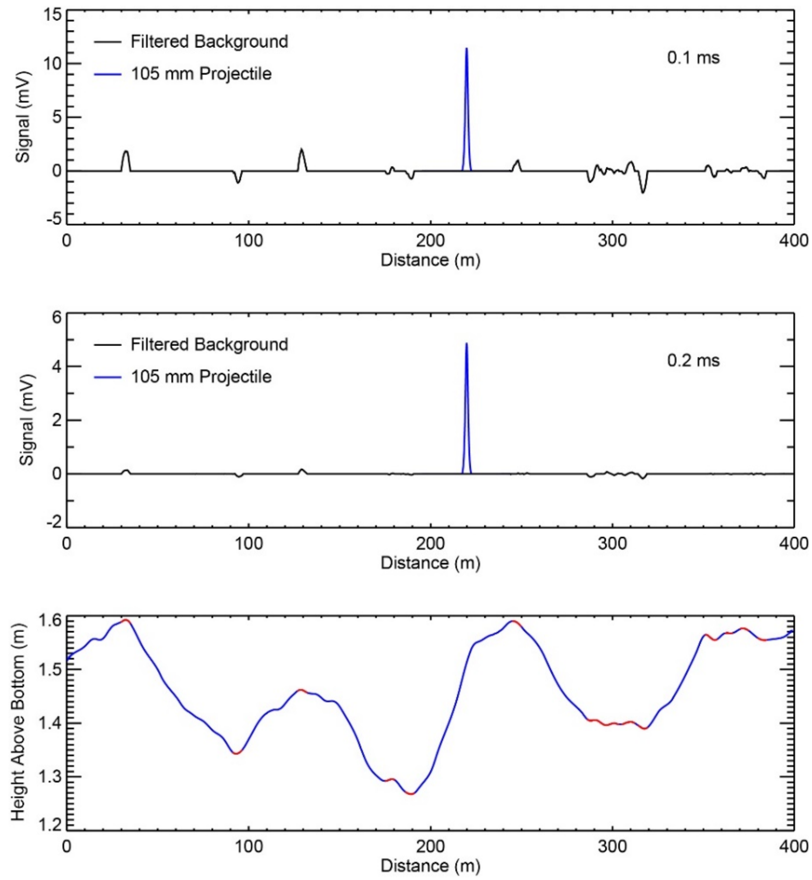

Figure 33. Median filtered MTA EMI array background response at 0.1 ms (top) and 0.2 ms (middle) compared with signal from 105 mm projectile at 220 m into the trajectory. Bottom plot shows the array height above the bottom, with areas where there are anomalies in the filtered background highlighted in red.

Conclusions

Over the period from July 2015 into March 2016 we collected more than 1000 data files on background and target response in a large (3.05 m diameter by 3.35 m deep) salt water tank. Most of the data were collected at a salinity of 35‰, with conductivity in the range 3.2-4.5 S/m depending on water temperature. There is nothing in the data to suggest that a salt water environment *per se* would compromise the utility of advanced TEM sensors for target classification.

A variety of different transmit coils were used to evaluate effects on noise and background response. Relative to data collected in air, measurements using transmit coils whose windings (which had PVC insulation) were exposed salt water showed modifications to the transmit current waveform and the initial ring-down of the receiver voltage as well as increased noise levels. We believe that these effects are due to leakage capacitance which arises when the coil windings are exposed to seawater [18]. The noise measured in water is consistently higher than the corresponding noise in air, sometimes by quite a substantial margin. Isolating the coils from the surrounding water suppresses the effect. The median water-to-air noise ratio for measurements with exposed coils is 9.1, while the median ratio for potted coils is 1.3.

In the tank, the background response to the water is modified by reflections from the top, bottom and side walls and ultimately is dominated by response from regions outside of the tank. Simple models predict that at the decay times accessible with our TEM sensors ($\gtrsim$ 1 ms), we should not see a signal from the water in the tank. Data collected using different transmit coils which were exposed to the water were consistent with this conclusion. There was no consistent background response above noise levels in the tank. Sensor noise, rather than background response, proved to be the limiting factor for our target response measurements.

A target's EMI response in an electrically conducting medium is a bit different from what we have come to expect on land. This is due to attenuation and phase shifts experienced by the primary and secondary magnetic fields when the surrounding medium is electrically conducting and electric field contributions to the response. Most of our tank testing focused on target responses and whether or not they are sufficiently modified in a salt water environment to adversely affect classification performance. The basic test protocol involved carefully measuring and comparing target and background responses in air and in the water. On the whole we found nothing to indicate that a salt water environment compromises the utility of advanced TEM sensors for target classification.

We did observe relatively weak electric field contributions to the early time response for bare aluminum targets located off to the side of the transmit and receive coils. This is where the electric field is strongest relative to the primary magnetic field. The effect went away if we insulated the target from the salt water by wrapping it in a thin plastic bag, and was not observed with bare steel targets or with inert ordnance items. Even for bare aluminum targets, it was not a significant factor for most sensor-target geometries. With the exception of test setups specifically targeting electric field effects, we found no significant differences between measured responses in air and in water for the different test items (various spheres, spheroids, cylinders and inert ordnance items) and test geometries.

During the summer of 2016 we conducted a series of cruises along the York River estuary, measuring EMI background response and its variation with depth along with supporting measurements of hydrographic and sediment properties. Water depths at the measurement sites varied from 4 m to 6 m, salinities from <1‰ to 23‰, and bottom sediments from mud and silt to sandy mud. Two vessels were used in the field exercises: the R/V Elis Olsson, a 29 ft. steel-hulled Monarch and the R/V Heron, a 26 ft. fiberglass-hulled Garvey. TEM profile data were collected by lowering NRL TEMTADS sensors from the R/V's stern davit. The steel hull affected data from roughly the upper 2 m of the water column.

The TEM profile data were compared with multi-layer (air, water and layered sediments) models for the background response with generally satisfactory results. There was a significant background response at early times ($\lesssim$ 0.25 ms) at the higher conductivity ($\gtrsim$ 2S/m). Near-bottom gradients of the background response decay rapidly, roughly as t^{-4}. Three layer models (air and water overlying a conducting half-space) can explain the general trends in the data but are unable to reproduce the details. We found that a four layer model (air, water and a shallow sediment layer overlying a deeper, less conductive half-space) was adequate to reproduce the measured profile. Inversion of the TEM data using a four layer model yielded a sediment model which was consistent with known sedimentary structure.

Calculations indicate that the background response and its variation are not small compared representative munitions signals at early times. However, when the background response varies smoothly it can be effectively dealt with by filtering techniques similar to those used in munitions response surveys on land.

Appendix. Modeling

This appendix includes mathematical details and derivations of models used in the analysis and interpretation of our test data. The first section deals with fields in and background response from an unbounded conducting medium. The next two deal with boundary effects: reflections from the tank sidewalls and reflections from the bottom and the water surface. The following section extends the analysis to multi-layered sediment models. The last section addresses the target response to electric fields in the tank.

We cannot obtain a workable analytical solution which accounts for both the tank sidewalls and the top and bottom simultaneously. We can get solutions which account separately for the sidewalls or for the top and bottom: an infinitely long circular conducting cylinder or an infinite horizontal slab. By combining the effects we can get some idea regarding the net effect of the complete set of boundaries: sidewalls, top and bottom. Because the electrical conductivity of the soil is of order 10^{-2} S/m and the magnetic susceptibility is of order 10^{-4} SI in the test area [23], for purposes of calculating boundary effects we may consider the volume surrounding the tank to be non-conducting and non-magnetic.

Calculating sidewall effects for a cylindrical tank becomes tractable if we consider a circular current loop centered on the tank axis. Testing was done with square or rectangular coils, but the circular loop remains a useful approximation. The largest differences between the sidewall fields for a square or rectangular loop and for a circular loop having the same area occur in the plane of the coil. For the 1 m square coil in a 3 m diameter tank, the maximum difference is 3% of the field for a circular coil. For the 2 ft by 3 ft and the 35 cm coils the corresponding values are 8% and 0.1%. The signal for co-located transmit and receive coils is a function of the magnetic flux through the center of the coils. In the absence of boundaries, for the square loops this is 1.6% larger than for equivalent circular loops. For the 2:3 aspect ratio rectangular coil it is 5.6% larger than for the equivalent circular loop. Considering the other sources of error in the experiments we do not feel that these differences are very significant.

Background Response

The vector potential for the magnetic field due to a current loop of radius a in a conducting medium is given by

$$\nabla^2 \boldsymbol{A} - \sigma\mu \frac{\partial \boldsymbol{A}}{\partial t} = -\mu \boldsymbol{I} \delta(\rho - a)\delta(z - h).$$

The loop carries a current of (t) Amperes and is located at $\rho = 0, z = h$ in cylindrical coordinates. σ and μ are the electrical conductivity and magnetic permeability of the medium. For a sinusoidal current of amplitude $\hat{I}$,

$$\boldsymbol{I}(t) = \hat{\boldsymbol{I}} e^{i\omega t}$$

which has only a φ component and $\partial/\partial\varphi = 0$, we have [38]

$$\frac{1}{\rho}\frac{\partial}{\partial\rho}\left(\rho\frac{\partial\hat{A}}{\partial\rho}\right) + \frac{\partial^2\hat{A}}{\partial z^2} - \frac{\hat{A}}{\rho^2} - i\omega\sigma\mu\hat{A} = -\mu\hat{I}\delta(\rho - a)\delta(z - h).$$

Applying the Fourier-Hankel transform

$$\widetilde{()} = \int_{-\infty}^{\infty}\int_{0}^{\infty} ()e^{-i\kappa z}\rho J_1(\lambda\rho)d\rho dz,$$

leads to a solution

$$\tilde{\hat{A}}(\kappa,\lambda) = \frac{\mu\hat{I}a}{\kappa^2 + \lambda^2 + i\omega\sigma\mu}e^{-i\kappa h}J_1(\lambda a).$$

Inverting the implied Fourier transform in time then yields the Fourier-Hankel transform of the impulse response

$$\tilde{A}(\kappa,\lambda,t) = \frac{\hat{I}a}{\sigma}J_1(\lambda a)e^{-\frac{\lambda^2 t}{\sigma\mu}}e^{-\left(i\kappa h+\frac{\kappa^2 t}{\sigma\mu}\right)}$$

for $t > 0$ [39, eq. 3.2(3)].

The inverse is separable,

$$A(\rho,z,t) = \frac{\hat{I}a}{\sigma}\left\{\int_0^{\infty}\lambda J_1(\lambda a)J_1(\lambda\rho)e^{-\frac{\lambda^2 t}{\sigma\mu}}d\lambda\right\}\left\{\frac{1}{2\pi}\int_{-\infty}^{\infty}e^{-\frac{\kappa^2 t}{\sigma\mu}}e^{i\kappa(z-h)}d\kappa\right\}$$

and the integrals in the brackets are tabulated [39, eq. 1.4(11), 8.11(23)]. The vector potential for the response to a current impulse of strength $\hat{I}$ in a loop with radius a at $\rho = 0$, $z = h$ is then

$$A(\rho,z,t) = \frac{\hat{I}a}{4\sqrt{\pi}\sigma}\left(\frac{t}{\sigma\mu}\right)^{-3/2} I_1\left(\frac{a\rho\sigma\mu}{2t}\right)e^{-\frac{\sigma\mu}{4t}[a^2+\rho^2+(z-h)^2]}.$$

The magnetic field $\boldsymbol{H}$ and magnetic induction or flux density $\boldsymbol{B}$ are given by

$$\boldsymbol{B} = \mu\boldsymbol{H} = \nabla\times\boldsymbol{A}.$$

Since $\boldsymbol{A}$ has only a φ component, $\boldsymbol{B}$ has only ρ and z components:

$$B_\rho = -\frac{\partial A}{\partial z} \quad and \quad B_z = \frac{1}{\rho}\frac{\partial\rho A}{\partial\rho}.$$

Without loss of generality we can set $h = 0$. The magnetic field components are then given in terms of modified Bessel functions of order 0 and 1 (I_0 and I_1) by

$$H_\rho = \frac{\hat{I}a}{\sqrt{\pi}t}\left(\frac{4t}{\sigma\mu}\right)^{-3/2} zI_1\left(\frac{a\rho\sigma\mu}{2t}\right)e^{-\frac{\sigma\mu}{4t}(a^2+\rho^2+z^2)} \quad \text{and}$$

$$H_z = \frac{\hat{I}a}{\sqrt{\pi}t}\left(\frac{4t}{\sigma\mu}\right)^{-3/2}\left\{aI_0\left(\frac{a\rho\sigma\mu}{2t}\right) - \rho I_1\left(\frac{a\rho\sigma\mu}{2t}\right)\right\}e^{-\frac{\sigma\mu}{4t}(a^2+\rho^2+z^2)}.$$

The corresponding electric field ($\nabla \times \boldsymbol{E} = -\partial \boldsymbol{B}/\partial t$) has only a φ component $E = -\partial A/\partial t$.

By Faraday's Law, the voltage induced in a loop is equal and opposite to the time rate of change of the magnetic flux through the loop, with

$$B = \nabla \times A = \frac{1}{\rho}\frac{\partial \rho A}{\partial \rho}$$

in our case. We are interested in the response to a current step down, so the induced voltage equals the flux through the loop due from a current impulse with the same strength. Green's theorem transforms the integral of $\nabla \times \boldsymbol{A}$ over the area enclosed by a loop to a line integral of $\boldsymbol{A}$ around the loop. The voltage induced in a co-located loop with radius b by a 1 A step down current in the primary loop is then

$$V(t) = \frac{\sqrt{\pi}\hat{I}ab}{2\sigma}\left(\frac{t}{\sigma\mu}\right)^{-3/2} I_1\left(\frac{ab\sigma\mu}{2t}\right)e^{-\frac{\sigma\mu}{4t}(a^2+b^2)}.$$

If the receive loop is very small ($b \to 0$) then this reduces to

$$V(t) = \frac{\sqrt{\pi}\mu\hat{I}a^2b^2}{t}\left(\frac{4t}{\sigma\mu}\right)^{-3/2} e^{-\frac{\sigma\mu}{4t}a^2},$$

which is also equal to πb^2 times the rate of change of the flux density at the center of the current loop. The factor $exp(-\sigma\mu a^2/4t)$ accounts for the diffusion of field changes in from the current loop. When $t >> \sigma\mu a^2$ the process is complete and dB/dt (or V) decays as $t^{-5/2}$.

The impulse response for a rectangular loop can be calculated by integrating a continuous magnetic dipole distribution having dipole moment density of $\hat{I}$ per unit area over the area enclosed by the loop. Expressions for the Cartesian (x, y, z) components of the impulse response of a z-directed magnetic dipole with moment m are obtained by rotating the corresponding expressions for the components of an x-directed dipole found in [40, eq. 2.60], so that

$$H_z = \frac{m\theta^3}{\pi^{3/2}t}e^{-\theta^2 r^2}\{\theta^2(z^2 - r^2) + 1\}$$

$$H_x = \frac{m\theta^3}{\pi^{3/2}t} e^{-\theta^2 r^2} \{\theta^2 xz\}$$

$$H_y = \frac{m\theta^3}{\pi^{3/2}t} e^{-\theta^2 r^2} \{\theta^2 yz\}$$

with $r^2 = x^2 + y^2 + z^2$ and $\theta^2 = \sigma\mu/4t$.

For a rectangular loop with side of length $2a$ and $2b$ the various integrals work out to

$$\smallint_{0X} = \int_{x-a}^{x+a} e^{-\theta^2 x^2} dx = \frac{\sqrt{\pi}}{2\theta} \operatorname{erf}(\theta x) \Big]_{x-a}^{x+a}$$

$$\smallint_{1X} = \int_{x-a}^{x+a} x e^{-\theta^2 x^2} dx = -\frac{1}{2\theta^2} e^{-\theta^2 x^2} \Big]_{x-a}^{x+a}$$

$$\smallint_{2X} = \int_{x-a}^{x+a} x^2 e^{-\theta^2 x^2} dx = \left[\frac{\sqrt{\pi}}{4\theta^3} \operatorname{erf}(\theta x) - \frac{x}{2\theta^2} e^{-\theta^2 x^2} \right]_{x-a}^{x+a}$$

and so forth for integrals over y. The field components for the impulse response of the loop are then

$$H_z = \{\smallint_{0X}\smallint_{0Y} - \theta^2 \smallint_{2X}\smallint_{0Y} - \theta^2 \smallint_{0X}\smallint_{2Y}\} \frac{\hat{I}\theta^3}{\pi^{3/2}t} e^{-\theta^2 z^2}$$

$$H_x = \theta^2 z \smallint_{1X}\smallint_{0Y} \frac{\hat{I}\theta^3}{\pi^{3/2}t} e^{-\theta^2 z^2}$$

$$H_y = \theta^2 z \smallint_{0X}\smallint_{1Y} \frac{\hat{I}\theta^3}{\pi^{3/2}t} e^{-\theta^2 z^2}.$$

Sidewall Reflections

Effects of the tank sidewalls are accounted for by adding solutions of the homogeneous (unforced) equation to the forced solution for an unbounded medium so that the boundary conditions are satisfied. The boundary conditions are continuity of the normal component of the magnetic induction $\boldsymbol{B}$ and of the tangential component of the magnetic field $\boldsymbol{H}$. In terms of the vector potential $\boldsymbol{A}$ (which as before has only a φ component) inside the tank (region 1) and outside the tank (region 2),

$$\frac{\partial \rho A_1}{\partial \rho} = \frac{\partial \rho A_2}{\partial \rho}$$

$$\frac{1}{\mu_1}\frac{\partial A_1}{\partial z} = \frac{1}{\mu_2}\frac{\partial A_2}{\partial z}$$

at the tank sidewall $\rho = R$. Since the magnetic susceptibility of the soil is of order 10^{-4} SI [23] we may set $\mu_1 = \mu_2 = \mu_0$ ($4\pi\times10^{-7}$ H/m).

General solutions of the homogeneous equation are

$$\hat{A}(\rho, z) = \frac{1}{2\pi}\int_{-\infty}^{\infty} F(u) I_1(\rho u) e^{i\kappa z} d\kappa$$

and

$$\hat{A}(\rho, z) = \frac{1}{2\pi}\int_{-\infty}^{\infty} G(u) K_1(\rho u) e^{i\kappa z} d\kappa$$

with $u = \sqrt{\kappa^2 + i\omega\sigma\mu}$, $\mathcal{R}(u) > 0$. Here I_1 and K_1 are modified Bessel functions of the first and second kind of order 1. The particular solution which satisfies the forcing was

$$\tilde{\hat{A}}(\kappa, \lambda) = \frac{\mu \hat{I} a}{\kappa^2 + \lambda^2 + i\omega\sigma\mu} e^{-i\kappa h} J_1(\lambda a).$$

Inverting the Hankel transform (and setting $h = 0$ without loss of generality), this becomes

$$\hat{A}(\rho, z) = \frac{\mu \hat{I} a}{2\pi}\int_{-\infty}^{\infty} I_1(\rho u) K_1(a u) e^{i\kappa z} d\kappa$$

for $0 < \rho < a$ or

$$\hat{A}(\rho, z) = \frac{\mu \hat{I} a}{2\pi}\int_{-\infty}^{\infty} I_1(a u) K_1(\rho u) e^{i\kappa z} d\kappa$$

for $a < \rho < \infty$ [39, eq. 8.11(10)]. Including the particular solution for $\rho > a$ and setting $\mu = \mu_0$, we then have

$$\hat{A}_1(\rho, z) = \frac{\mu_0 \hat{I} a}{2\pi}\int_{-\infty}^{\infty} I_1(a u) K_1(\rho u) e^{i\kappa z} d\kappa + \frac{1}{2\pi}\int_{-\infty}^{\infty} F(u) I_1(\rho u) e^{i\kappa z} d\kappa$$

inside the tank, where now $u = \sqrt{\kappa^2 + i\omega\sigma\mu_0}$ in terms of the electrical conductivity σ of the water in the tank, and since the surrounding soil is essentially non-conducting [23]

$$\hat{A}_2(\rho, z) = \frac{1}{2\pi}\int_{-\infty}^{\infty} G(|\kappa|) K_1(\rho|\kappa|) e^{i\kappa z} d\kappa$$

outside the tank.

Applying the boundary conditions and working through the algebra to determine (u) we get the complete solution for $\rho < a$:

$$\hat{A}(\rho, z) = \frac{\mu_0 \hat{I} a}{\pi} \int_0^{\infty} \{K_1(au) + C I_1(au)\} I_1(\rho u) \cos(\kappa z)\, d\kappa.$$

The first term corresponds to the response in an unbounded medium and the second term corresponds to the reflection from the sides of the cylinder. The reflection coefficient is

$$C = -\frac{\kappa K_1(uR) K_0(\kappa R) - u K_1(\kappa R) K_0(uR)}{\kappa I_1(uR) K_0(\kappa R) + u K_1(\kappa R) I_0(uR)}.$$

The voltage induced a small co-located loop with area πb^2 is then

$$V(t) = \frac{\mu_0 \hat{I} a b^2}{2\pi} \int_{-\infty}^{\infty} \int_0^{\infty} \{K_1(au) + C I_1(au)\}\, u e^{i\omega t} d\kappa\, d\omega.$$

Figure 34 is an example. It shows the background response at the center of a 1 m diameter loop on the axis of a 3 m diameter cylinder having a conductivity of 4 S/m. The current in the loop is a 1 A step down at time $t = 0$. The integrals were calculated by simple numerical quadrature in κ followed by a Fast Fourier Transform in ω. B_0 denotes the background response for an unbounded medium and B_R the reflection from the cylinder walls. The response is negative for the dashed portion of B_R. $B_R \rightarrow -B_0$ asymptotically for $t >> T_D = R^2\sigma\mu_0$ where R is the tank radius (T_D = 11 µs for R = 1.5 m and σ = 4 S/m). Once the field has diffused in from the loop the response scales with the size of the tank through the diffusion time scale T_D. Considered as a function of t/T_D the amplitude scales with $T_D^{5/2}$. Asymptotically the response is unchanged – for a larger tank it just takes longer for the reflected fields to be fully realized. In this regime changes in the size of the current loop affect only the strength of the response due to changes in the transmit moment.

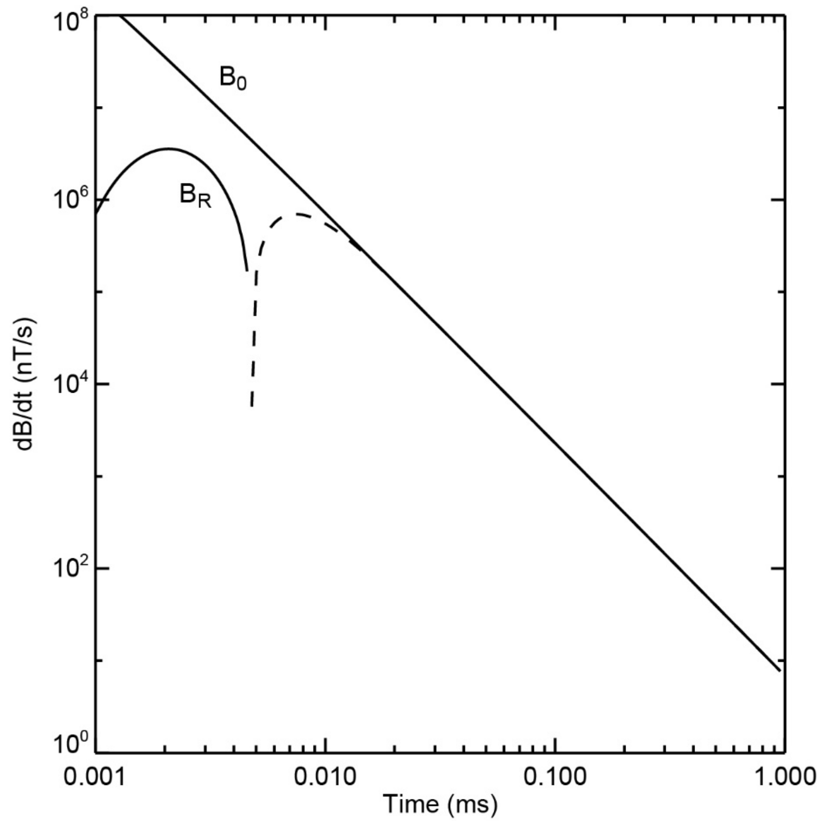

Figure 34. Background response at the center of a 1 m diameter loop on the axis of a 3 m diameter cylinder having a conductivity of 4 S/m. The current in the loop is a 1 A step down. B_0 is the background response for an unbounded medium and B_R is the reflection from the cylinder walls. The response is negative for the dashed portion of B_R. Asymptotically $B_R \rightarrow -B_0$.

Top and Bottom

As with the sidewalls, we start with the solution of the forced problem in an unbounded medium and then proceed to account for the boundaries by adding appropriate solutions to the homogeneous equation. Anticipating a boundary at $z = 0$ a distance h above the source, the particular solution for a loop with radius a located at $z = -h$ is as before

$$\tilde{\hat{A}}(\kappa, \lambda) = \frac{\mu \hat{I} a}{\kappa^2 + \lambda^2 + i\omega\sigma\mu} e^{i\kappa h} J_1(\lambda a).$$

Inverting the Fourier transform in z,

$$\hat{A} = \frac{\mu \hat{I} a}{2} \int_0^\infty \frac{\lambda}{u} e^{-u|z+h|} J_1(\lambda a) J_1(\lambda \rho) d\lambda$$

where now $u = \sqrt{\lambda^2 + i\omega\sigma\mu}$, $\mathcal{R}(u) > 0$. General solutions of the homogeneous equation are

$$\hat{A} = \int_0^\infty F(\lambda)e^{\pm uz}J_1(\lambda\rho)d\lambda.$$

Consider first a single plane boundary above the source at z = 0. Setting $\mu = \mu_0$, we then have

$$\hat{A}_1(\rho, z) = \frac{\mu_0 \hat{I} a}{2}\int_0^\infty \frac{\lambda}{u}J_1(\lambda a)J_1(\lambda\rho)e^{-u|z+h|}d\lambda + \int_0^\infty F(\lambda)J_1(\lambda\rho)e^{-u|z|}d\lambda$$

in the water, with $u = \sqrt{\lambda^2 + i\omega\sigma\mu_0}$. In our case region 2 is air and can set σ = 0, so that

$$\hat{A}_2(\rho, z) = \int_0^\infty G(\lambda)J_1(\lambda\rho)e^{-\lambda|z|}d\lambda$$

for z > 0.

The boundary conditions are as before, only now applied at z = 0. Applying the boundary conditions and working through the algebra to determine (λ) we get the complete solution

$$\hat{A}(\rho, z) = \frac{\mu_0 \hat{I} a}{2}\int_0^\infty \left\{e^{-u|z+h|} + Ce^{-u(|z|+h)}\right\}\frac{\lambda}{u}J_1(\lambda a)J_1(\lambda\rho)d\lambda.$$

The first term corresponds to the response in an unbounded medium and the second term corresponds to the reflection from the boundary at z = 0. In this case the reflection coefficient is simply

$$C = \frac{u - \lambda}{u + \lambda}.$$

The voltage induced a small co-located (*i.e.* at z = -h) loop with area πb^2 is then

$$V(t) = \frac{\mu_0 \hat{I} a b^2}{2}\int_{-\infty}^\infty \int_0^\infty \{1 + Ce^{-2uh}\}\frac{\lambda^2}{u}J_1(\lambda a)e^{i\omega t}d\lambda d\omega.$$

If the region above the surface were conducting the λ's would be replaced by u's based on the conductivity in that region. In full generality we would have

$$C_{21} = \frac{\mu_1 u_2 - \mu_2 u_1}{\mu_1 u_2 + \mu_2 u_1}$$

with subscripts 1 and 2 referring to the regions above and below the surface respectively. The convention C_{21} refers to the reflection of the field in region 2 by the boundary with region 1.

Figure 35 is an example of the response for an air-water boundary. It shows the background response at the center of a 1 m diameter loop located 1.5 m below the surface. The conductivity of the water is 4 S/m. The current in the loop is a 1 A step down. B_0 is the background response for an unbounded medium and B_R is the reflection from the surface. The response is negative for the dashed portion of B_R. As before, the integrals were calculated by simple numerical quadrature in κ followed by a Fast Fourier Transform in ω. In this case $B_R \rightarrow -0.5\ B_0$ asymptotically for $t >> T_D = L^2\sigma\mu_0$ where now L is distance from the surface (T_D = 11 μs for L = 1.5 m and σ = 4 S/m). This asymptotic ratio depends on the conductivity contrast between the layers. Once the field has diffused in from the loop the response scales with L through the diffusion time scale T_D. Considered as a function of t/T_D the amplitude scales with $T_D^{5/2}$. Asymptotically the response is unchanged – if the loop is farther from the surface it just takes longer for the reflected fields to be fully realized. In this regime changes in the size of the current loop affect only the strength of the response due to changes in the transmit moment.

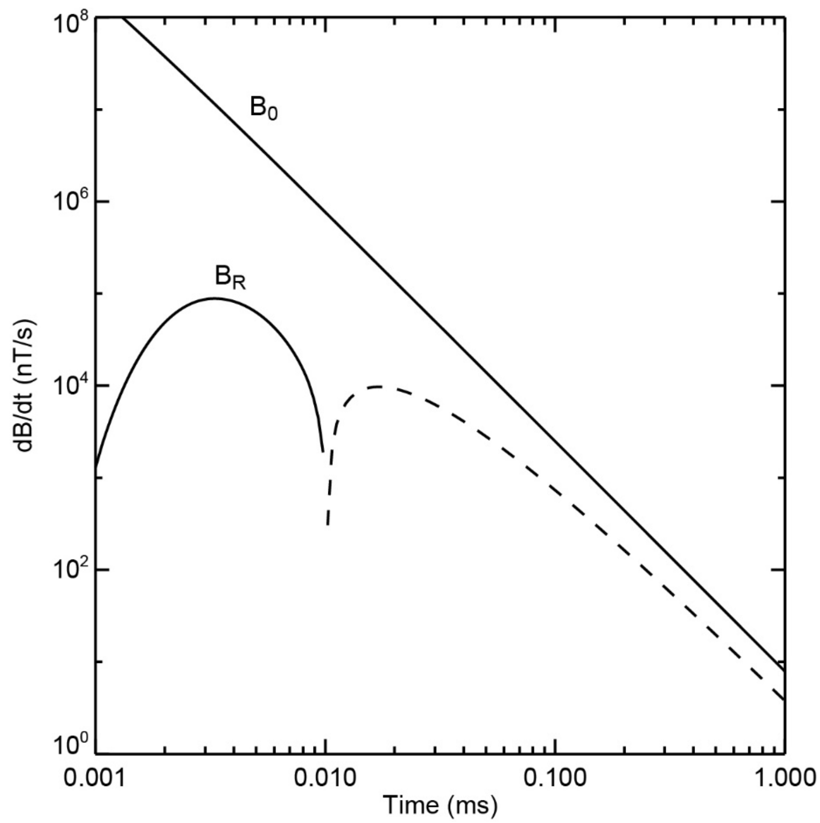

Figure 35. Background response at the center of a 1 m diameter loop below the surface of a semi-infinite body of salt water having a conductivity of 4 S/m. The current in the loop is a 1 A step down. B_0 is the background response for an unbounded medium and B_R is the reflection from the surface. The response is negative for the dashed portion of B_R. The $B_R \rightarrow -0.5\ B_0$ for times large compared to the diffusion time scale $T_D = L^2\sigma\mu_0/2$ where the characteristic length scale L is the distance below the surface (T_D = 5.6 μs for L = 1.5 m).

Including a lower boundary is straightforward. Expressions for the relevant reflection coefficients are given in [41]. With a current loop at $z = -h$ and the bottom at $z = -d$ we have

$$\hat{A}(\rho,z) = \frac{\mu_0 \hat{I} a}{2}\int_0^\infty \left\{e^{-u|z+h|} + R_S e^{-u(|z|+h)} + R_B e^{-u([d+z]+[d-h])}\right\}\frac{\lambda}{u}J_1(\lambda a)J_1(\lambda\rho)d\lambda.$$

Writing

$$C_S = \frac{u-\lambda}{u+\lambda}$$

for the basic reflection at the surface (air water boundary) and

$$C_B = \frac{\mu_B u - \mu_0 u_B}{\mu_B u + \mu_0 u_B}$$

for the reflection condition at the bottom, where the subscript B references the bottom, we have

$$R_S = \frac{C_S\left(1 + C_B e^{-2u(d-h)}\right)}{1 - C_S C_B e^{-2ud}}$$

and

$$R_B = \frac{C_B(1 + C_S e^{-2uh})}{1 - C_S C_B e^{-2ud}}.$$

The voltage induced a small co-located loop with area πb^2 is then

$$V(t) = \frac{\mu_0 \hat{I} a b^2}{2}\int_{-\infty}^{\infty}\int_0^\infty \left\{1 + R_S e^{-2uh} + R_B e^{-2u(d-h)}\right\}\frac{\lambda^2}{u}J_1(\lambda a)e^{i\omega t}d\lambda d\omega.$$

If both the surface and the bottom are non-conducting and nonmagnetic then

$$R_S = C\,\frac{1 + Ce^{-2u(d-h)}}{1 + Ce^{-ud}}\,\frac{1}{1 - Ce^{-ud}}$$

and

$$R_B = C\,\frac{1 + Ce^{-2uh}}{1 + Ce^{-ud}}\,\frac{1}{1 - Ce^{-ud}}$$

with $C = (u-\lambda)/(u+\lambda)$ and $u = \sqrt{\lambda^2 + i\omega\sigma\mu_0}$ based on the conductivity in the layer. As noted in [41] we can expand the last term in these expressions so that it appears as a sequence of reflections at the boundaries:

$$\frac{1}{1 - Ce^{-ud}} = \sum_{n=0}^{\infty} C^n e^{-nud}.$$

To the extent that these subsequent reflections have little effect on the overall response, the net effect of the pair of boundaries should be about twice that for a single boundary when the loops are near the center of the layer since the middle term in the expressions for R_S and R_B equals one when $h = d/2$. This is borne out by numerical evaluation of the integrals for a 1 m diameter loop 1.5 m below the surface of a 3 m deep layer having a conductivity of 4 S/m. In this case the asymptotic ratio of the boundary contribution to the background response in the middle of the layer is about 1.8 times the corresponding boundary effect 1.5 m below the surface for the semi-infinite medium.

Layered Sediment Models

We cannot assume that the physical properties of the bottom sediments are uniform in depth. The standard approach is to represent the sediments by a series of layers with different physical properties [7, 42]. Figure 36 shows the notation and coordinate system for the horizontally layered sediment model used here. The EMI source is a current loop with radius a at Z = Z_S in the water layer.

As before, we start with the solution of the forced problem in an unbounded medium and then proceed to account for the boundaries using solutions of the homogeneous problem. The vector potential $\boldsymbol{A}$ satisfies

$$\nabla^2 \boldsymbol{A} - \sigma\mu \frac{\partial \boldsymbol{A}}{\partial t} = -\mu \boldsymbol{I} \delta(\rho - a)\delta(z - h)$$

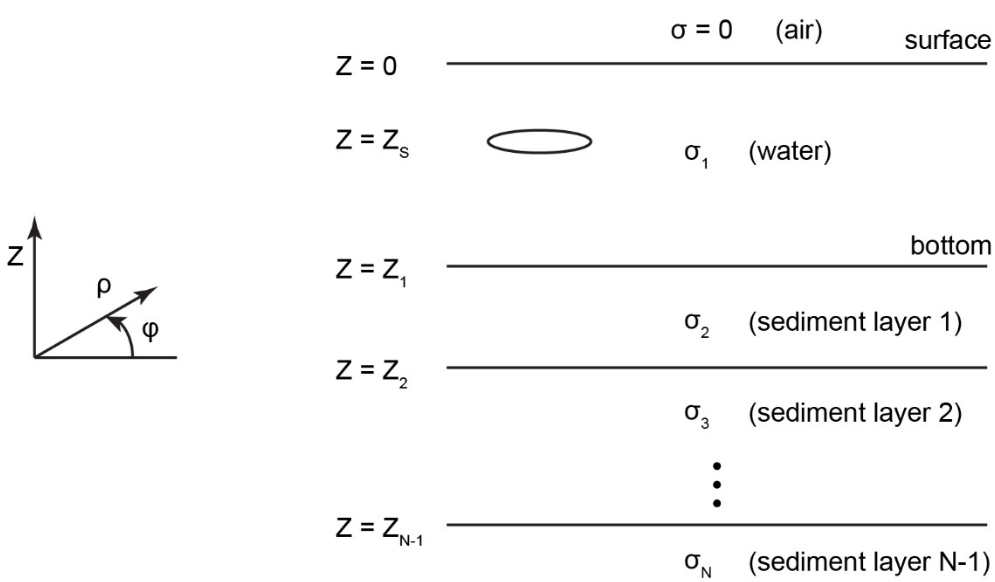

Figure 36. Notation and coordinate system for the horizontally layered sediment model.

The loop has radius a and carries a current I and is located at $\rho = 0$, $z = z_s$ in cylindrical coordinates. σ and μ are the electrical conductivity and magnetic permeability of the medium. For a sinusoidal current

$$\boldsymbol{I}(t) = \hat{\boldsymbol{I}} e^{i\omega t}$$

which has only a φ component and $\partial/\partial\varphi = 0$, we have

$$\frac{1}{\rho}\frac{\partial}{\partial \rho}\left(\rho \frac{\partial \hat{A}}{\partial \rho}\right) + \frac{\partial^2 \hat{A}}{\partial z^2} - \frac{\hat{A}}{\rho^2} - i\omega\sigma\mu\hat{A} = -\mu\hat{I}\delta(\rho - a)\delta(z - h).$$

Applying the Fourier-Hankel transform

$$\widetilde{()} = \int_{-\infty}^{\infty}\int_{0}^{\infty} ()e^{-i\kappa z}\rho J_1(\lambda\rho)d\rho dz,$$

we have

$$\tilde{\tilde{A}}(\kappa, \lambda) = \frac{\mu\hat{I}a}{\kappa^2 + \lambda^2 + i\omega\sigma\mu}e^{-i\kappa h}J_1(\lambda a).$$

Inverting the Fourier transform in z,

$$\hat{A} = \frac{\mu\hat{I}a}{2}\int_0^\infty \frac{\lambda}{u}e^{-u|z+h|}J_1(\lambda a)J_1(\lambda\rho)d\lambda$$

where now $u = \sqrt{\lambda^2 + i\omega\sigma\mu}$, $\mathcal{R}(u) > 0$.

General solutions of the homogeneous equation are

$$\hat{A} = \int_0^\infty F^{\pm}(\lambda)e^{\pm uz}J_1(\lambda\rho)d\lambda.$$

Boundary conditions are continuity of the tangential component of the magnetic field $\boldsymbol{H}$ and the normal component of the magnetic induction or flux density $\boldsymbol{B}$, where

$$\boldsymbol{B} = \mu\boldsymbol{H} = \nabla \times \boldsymbol{A}.$$

Since $\boldsymbol{A}$ has only a φ component, $\boldsymbol{B}$ (and $\boldsymbol{H}$) has only ρ and z components:

$$B_\rho = -\frac{\partial A}{\partial z} \quad and \quad B_z = \frac{1}{\rho}\frac{\partial \rho A}{\partial \rho}.$$

Hence we need

$$\frac{\partial \rho A_j}{\partial \rho} = \frac{\partial \rho A_{j+1}}{\partial \rho}$$

$$\frac{1}{\mu_j}\frac{\partial A_j}{\partial z} = \frac{1}{\mu_{j+1}}\frac{\partial A_{j+1}}{\partial z}$$

at each boundary. Measured values of the magnetic susceptibility for our sediment samples from the York were all less than 10^{-4} SI, so we simply use $\mu = \mu_0 = 4\pi\text{x}10^{-7}$ H/m in each layer for our calculations. Since our calculations are done in the frequency domain and then transformed to the time domain, we could easily include a frequency dependent permeability [43] to account for magnetic sediments.

More generally, we write

$$\hat{A}_j = \int_0^\infty \left\{F_j^+(\lambda)e^{+u_j z} + F_j^-(\lambda)e^{-u_j z}\right\} J_1(\lambda\rho)d\lambda$$

for the homogeneous solution in each layer. In the water (layer 1) the solution is

$$\hat{A}_1 = \int_0^\infty \left\{F_1^+(\lambda)e^{+u_1 z} + F_1^-(\lambda)e^{-u_1 z} + \frac{\mu \hat{I} a}{2}\frac{\lambda}{u_1}e^{-u_1|z-z_s|}\right\} J_1(\lambda\rho)d\lambda.$$

The basic idea then then to work up from the lowest layer and down from the surface to obtain a pair of equations in $F_1^+$and F_1^-. We simplify the notation by writing

$$C_{ij} = \frac{u_j - u_i}{u_j + u_i}$$

for the reflection coefficient from layer i into layer j and setting

$$f_S(\lambda) = \frac{\mu \hat{I} a}{2}\frac{\lambda}{u_1}J_1(\lambda a).$$

In the air, $F_0^+ = 0$, so across the surface (z = 0) we have

$$F_0^- = F_1^+ + F_1^- + f_S e^{u_1 z_s}$$

$$-\lambda F_0^- = u_1 F_1^+ - u_1 F_1^- - u_1 f_S e^{u_1 z_s},$$

or

$$F_1^+ = C_{01}\{F_1^- + f_S e^{u_1 z_s}\}.$$

Going from the water into the sediment,

$$F_1^+ e^{u_1 z_1} + F_1^- e^{-u_1 z_1} + f_S e^{u_1(z_1 - z_s)} = F_2^+ e^{u_2 z_1} + F_2^- e^{-u_2 z_1}$$

$$u_1 F_1^+ e^{u_1 z_1} - u_1 F_1^- e^{-u_1 z_1} + u_1 f_S e^{u_1(z_1 - z_s)} = u_2 F_2^+ e^{u_2 z_1} - u_2 F_2^- e^{-u_2 z_1}.$$

Between sediment layers we have similar equations without the f_S term. Going into the final (N+1) layer $F_{N+1}^- = 0$, so that

$$F_{N+1}^+ e^{u_{N+1} z_N} = F_N^+ e^{u_N z_N} + F_N^+ e^{u_N z_N}$$

$$u_{N+1} F_{N+1}^+ e^{u_{N+1} z_N} = u_N F_N^+ e^{u_N z_N} - u_N F_N^+ e^{-u_N z_N},$$

from which

$$F_N^- = C_{N+1,N} F_N^+.$$

For a four-layer (two sediment layers) model we have four equations:

$$F_1^+ = C_{01}\{F_1^- + f_S e^{u_1 z_s}\}$$

$$F_1^+ e^{u_1 z_1} + F_1^- e^{-u_1 z_1} + f_S e^{u_1(z_1 - z_s)} = F_2^+ e^{u_2 z_1} + F_2^- e^{-u_2 z_1}$$

$$u_1 F_1^+ e^{u_1 z_1} - u_1 F_1^- e^{-u_1 z_1} + u_1 f_S e^{u_1(z_1 - z_s)} = u_2 F_2^+ e^{u_2 z_1} - u_2 F_2^- e^{-u_2 z_1}$$

$$F_2^- = C_{32} F_2^+.$$

Solving for the homogeneous field components in the water (layer 1) we have

$$F_1^- = \frac{u_1 D_+ (1 + C_{01} e^{2u_1 z_s}) - u_2 D_- (1 + C_{01} e^{2u_1 z_s})}{u_1 D_+ (1 - C_{01} e^{2u_1 z_1}) + u_2 D_- (1 + C_{01} e^{2u_1 z_1})} f_S e^{2u_1 z_1} e^{-u_1 z_s}$$

$$F_1^+ = C_{01}\{F_1^- + f_S e^{u_1 z_s}\},$$

where

$$D_\pm = 1 \pm C_{32} e^{2u_2(z_2 - z_1)}.$$

The voltage induced in a small loop with radius b located a horizontal distance x from the transmitter is then

$$V(t) = \frac{\mu_0 \hat{I} a b^2}{2} \int_{-\infty}^{\infty} \int_0^{\infty} \{1 + F_1^+ e^{u_1 z_s} + F_1^- e^{-u_1 z_s}\} \frac{\lambda^2}{u} J_1(\lambda a) J_1(\lambda x) e^{i\omega t} d\lambda d\omega.$$

The integrals are calculated by simple numerical quadrature in λ followed by a Fast Fourier Transform in ω. We used 2000 terms with $\Delta\lambda$ = 0.025 m^{-1} and 2^{18} terms with Δf = 200 Hz for the cases considered here.

Electric Field Effects

In the frequency domain the vector potential $\boldsymbol{F}$ for the electric field due to a harmonic magnetic dipole with dipole moment $\boldsymbol{m} = I_0 d\boldsymbol{A}$ at the origin is given by

$$\nabla^2 \boldsymbol{F} + k^2 \boldsymbol{F} = -i\omega\mu_0 \boldsymbol{m}\delta(x)\delta(y)\delta(z)$$

with $k^2 = -i\omega\sigma\mu_0$, where σ is the background conductivity. The solution is

$$\boldsymbol{F}(\boldsymbol{r}) = \frac{i\omega\mu_0 \boldsymbol{m}}{4\pi r} e^{-ikr}$$

[40, eq. 2.54]. The electric field $\boldsymbol{E} = -\nabla \times \boldsymbol{F}$ is then

$$\boldsymbol{E} = -\frac{i\omega\mu_0 I_0}{4\pi} \nabla \times \left(\frac{d\boldsymbol{A}}{r} e^{-ikr}\right).$$

Following [40, eq. 2.51 *etc.*] the corresponding time domain solution for an upwards current step I_0 is

$$\boldsymbol{E}_0(\boldsymbol{r}, t) = \frac{\mu_0 I_0}{2\pi^{3/2} t} e^{-\theta^2 r^2} \boldsymbol{r} \times d\boldsymbol{A}$$

with $\theta^2 = \sigma\mu_0/4t$. This is a brief pulse at very early time which gets convolved with the target's response function. As a practical matter we can simply integrate $\boldsymbol{E}$ over time and multiply the response function by the result. We can then calculate the electric field for a loop by treating this as a dipole density and integrating over the area enclosed by the loop so that the strength of the primary field impulse due to a current step of strength I_0 in the loop is

$$\boldsymbol{E}_0 dt = \frac{\mu_0 I_0}{4\pi} \iint \frac{1}{r^3} \boldsymbol{r} \times d\boldsymbol{A}.$$

Introducing a coil response function for the electric field

$$\boldsymbol{G}(\boldsymbol{r}) = \frac{1}{4\pi} \iint \frac{\boldsymbol{r} \times d\boldsymbol{A}}{r^3}$$

we can express the primary field impulse strength as

$$\boldsymbol{E}_0 dt = \mu_0 I_0 \boldsymbol{G}_T(\boldsymbol{r})$$

where the subscript T refers to the transmit loop.

By analogy with the eddy current problem [25] we represent the target response by an induced electric dipole with moment

$$Id\boldsymbol{s} = \sigma \int \boldsymbol{E}_0(t')\boldsymbol{\mathcal{P}}(t - t')dt'$$

where $\boldsymbol{\mathcal{P}}$ is the polarizability tensor for the target's electric field response. Again, since the electric field impulse occurs at very early time we simply integrate the impulse and replace the convolution with the product so that the induced electric dipole moment is given by

$$Id\boldsymbol{s} = \sigma\mu_0 I_0 \boldsymbol{G}_T \boldsymbol{\mathcal{P}}.$$

We can follow through the derivations in [40] to determine the magnetic flux through the receive coil from the induced dipole or simply invoke electromagnetic reciprocity [44] and recognize that the voltage induced in a receive loop for a downwards current step of strength I_0 is simply

$$V(t) = \sigma\mu_0^2 I_0 \boldsymbol{G}_R \cdot \left(\boldsymbol{G}_T \frac{d\boldsymbol{\mathcal{P}}}{dt}\right)$$

wherein $\boldsymbol{G_R}$ is now the receive coil response function.

Appendix. Data Tables.

Table 4. Suspended Particulate Matter (SPM) Concentrations.

Table 2.
Suspended Particulate Matter (SPM) Concentrations

Cruise	Desc.	Station Code	Water depth m (from Castaway CTD)	Sample depth m (Approx marked line)	Sample ID	Suspended Particulate Matter (SPM) >0.7 microns								
						TSPM<60 mg/L	FSPM<60 mg/L	VSPM<60 mg/L	TSPM>60 mg/L	FSPM>60 mg/L	VSPM>60 mg/L	TSPM mg/L	FSPM mg/L	VSPM mg/L
YR160624	Clay Bank Mud	CB	5.18	1	5657T	38.50	24.00	14.50	***	***	***	38.50	24.00	14.50
				2	5657M	44.50	28.50	16.00	***	***	***	44.50	28.50	16.00
				4	5657B	59.50	41.00	18.50	***	***	***	59.50	41.00	18.50
YR160701	Gloucester Pt Mud	GP	4.60	1	5667T	19.17	15.33	3.83	0.00	0.00	0.00	19.17	15.33	3.83
				2	5667M	24.17	20.17	4.00	0.00	0.00	0.00	24.17	20.17	4.00
				3.5	5667B	55.00	45.25	9.75	0.00	0.00	0.00	55.00	45.25	9.75
YR160706	Pamunkey Mud	PM	4.30	1	S5673T	26.32	18.16	8.16	***	***	***	26.32	18.16	8.16
				2	S5673M	32.67	21.00	11.67	***	***	***	32.67	21.00	11.67
				3.5	S5673B	41.33	30.00	11.33	***	***	***	41.33	30.00	11.33
YR160706_2	West Point Mud	WP	4.16	1	S5675T	28.95	20.26	8.68	***	***	***	28.95	20.26	8.68
				2	S5675M	31.39	21.67	9.72	***	***	***	31.39	21.67	9.72
				3.5	S5675B	77.63	61.58	16.05	***	***	***	77.63	61.58	16.05
YR160714	Ferry Point Sand/Mud	FP	4.10	1	S5681T	18.00	11.83	6.17	***	***	***	18.00	18.00	6.17
				2	S5681M	13.33	9.50	3.83	0.27	0.18	0.09	13.61	9.68	3.92
				3.5	S5681B	27.33	21.33	6.00	0.20	0.20	***	27.53	21.53	6.00
YR160721	Pamunkey Sand/Mud	PS	3.50	1	S5690T	19.50	15.75	3.75	***	***	***	19.50	15.75	3.75
				2.5	S5690M	17.75	13.75	4.00	***	***	***	17.75	13.75	4.00
				3	S5690B	56.75	47.00	9.75	0.58	0.38	0.19	57.33	47.38	9.94
YR160805	Goodwin Island Sand/Mud	GI	4.40	1	S5700T	11.00	7.75	3.25	***	***	***	11.00	7.75	3.25
				2	S5700M	11.25	8.25	3.00	***	***	***	11.25	8.25	3.00
				4	S5700B	12.38	8.75	3.63	***	***	***	12.38	8.75	3.63
YR160920	Naval Weapons Mud	NWS	5.90	0.1	S5737	12.17	9.50	2.67	***	***	***	12.17	9.50	2.67

** Below Detection Limit

Table 5. Temperature, conductivity and salinity profiles.

Table 3.1

Temperature, Conductivity and Salinity profiles (from Castaway CTD)

Cruise / Time (EST)	YR160623 / 0620				YR160624 / 0708				YR160624 / 0918				YR160701/ 0659				YR160701/ 0854			
Desc.	Clay Bank Mud				Clay Bank Mud				Clay Bank Mud				Gloucester Pt Mud				Gloucester Pt Mud			
Station Code	CB_160623_0620				CB_160624_0708				CB_160624_0918				GP_160701_0659				GP_160701_0854			
Water depth (m)	5.18				5.15				5.37				4.56				4.36			
	Depth (m)	Temperature (deg C)	Conductivity (µS/cm)	Salinity (PSU)	Depth (m)	Temperature (deg C)	Conductivity (µS/cm)	Salinity (PSU)	Depth (m)	Temperature (deg C)	Conductivity (µS/cm)	Salinity (PSU)	Depth (m)	Temperature (deg C)	Conductivity (µS/cm)	Salinity (PSU)	Depth (m)	Temperature (deg C)	Conductivity (µS/cm)	Salinity (PSU)
	0.15	25.43	24414.41	14.68	0.15	25.20	24506.49	14.81	0.15	25.35	24398.26	14.69	0.15	25.81	30525.02	18.60	0.15	26.13	30944.50	18.75
	0.46	25.43	24417.25	14.68	0.46	25.19	24616.79	14.89	0.46	25.32	24406.51	14.70	0.45	25.78	30564.75	18.63	0.45	26.10	30965.77	18.77
	0.76	25.40	24541.21	14.77	0.76	25.16	24640.21	14.91	0.76	25.31	24423.64	14.72	0.76	25.79	30682.95	18.71	0.76	26.08	31025.75	18.82
	1.06	25.37	24719.64	14.89	1.06	25.14	24663.48	14.93	1.06	25.28	24458.27	14.75	1.06	25.82	30761.74	18.75	1.06	26.05	31116.15	18.89
	1.37	25.36	24918.34	15.03	1.37	25.11	24741.11	14.99	1.37	25.22	24606.67	14.87	1.36	25.86	30945.40	18.86	1.36	26.03	31207.96	18.96
	1.67	25.37	24978.79	15.07	1.67	25.09	24850.62	15.07	1.67	25.21	24674.09	14.92	1.67	25.86	31136.37	18.98	1.67	25.99	31422.28	19.13
	1.97	25.37	25139.15	15.17	1.97	25.08	24912.44	15.12	1.97	25.19	24748.18	14.97	1.97	25.86	31438.06	19.19	1.97	25.93	31660.03	19.31
	2.28	25.37	25169.82	15.19	2.28	25.08	24989.23	15.17	2.28	25.16	24871.42	15.06	2.27	25.83	31642.28	19.34	2.27	25.90	31805.72	19.42
	2.58	25.37	25251.32	15.25	2.58	25.09	25080.70	15.23	2.58	25.14	25012.61	15.17	2.57	25.75	31802.75	19.48	2.57	25.84	31881.04	19.49
	2.88	25.37	25311.44	15.29	2.89	25.10	25132.83	15.26	2.88	25.09	25365.36	15.41	2.88	25.67	32097.03	19.71	2.88	25.82	31911.00	19.52
	3.19	25.37	25391.50	15.34	3.19	25.10	25179.86	15.29	3.19	25.06	25536.65	15.54	3.18	25.57	32452.10	20.00	3.18	25.82	31913.83	19.53
	3.49	25.36	25456.85	15.38	3.49	25.11	25198.32	15.30	3.49	25.05	25547.31	15.55	3.48	25.51	32480.71	20.04	3.48	25.80	31930.90	19.54
	3.80	25.36	25503.63	15.42	3.80	25.12	25211.22	15.30	3.80	25.05	25550.14	15.55	3.78	25.48	32539.99	20.10	3.78	25.79	31951.16	19.57
	4.10	25.35	25542.33	15.44	4.10	25.11	25230.12	15.32	4.10	25.05	25580.56	15.57	4.09	25.46	32747.20	20.25	4.09	25.76	31966.91	19.59
	4.40	25.35	25544.16	15.45	4.40	25.11	25229.87	15.32	4.40	25.05	25603.24	15.59	4.39	25.42	32887.29	20.36	4.37	25.77	31960.30	19.58
	4.71	25.35	25547.31	15.45	4.71	25.09	25235.35	15.33	4.71	25.03	25630.49	15.61	4.56	25.43	32911.47	20.37				
	5.01	25.34	25638.34	15.51	5.15	25.11	25252.40	15.33	5.01	25.02	25774.38	15.71								
	5.18	25.34	25638.18	15.51					5.37	25.02	25857.68	15.77								

Table 5, continued.

Table 3.2

Temperature, Conductivity and Salinity profiles (from Castaway CTD)

Cruise	YR160706 / 0926				YR160706 / 0941				YR160706_2 / 1023				YR160714 / 0636				YR160714 / 0841			
Desc.	Pamunkey Mud				Pamunkey Mud				West Point Mud				Ferry Point Sand/Mud				Ferry Point Sand/Mud			
Station Code	PM_160706_0926				PM_160706_0941				WP_160706_1023				FP_160714_0636				FP_160714_0841			
Water depth (m)	6.25				4.45				4.16				4.11				5.52			
	Depth (m)	Temperature (deg C)	Conductivity (µS/cm)	Salinity (PSU)	Depth (m)	Temperature (deg C)	Conductivity (µS/cm)	Salinity (PSU)	Depth (m)	Temperature (deg C)	Conductivity (µS/cm)	Salinity (PSU)	Depth (m)	Temperature (deg C)	Conductivity (µS/cm)	Salinity (PSU)	Depth (m)	Temperature (deg C)	Conductivity (µS/cm)	Salinity (PSU)
	0.15	27.23	266.65	0.12	0.15	27.23	1226.86	0.58	0.15	27.89	4975.33	2.51	0.15	28.90	24408.87	13.63	0.15	29.33	24163.29	13.36
	0.46	27.09	269.44	0.13	0.46	27.00	1222.81	0.58	0.46	27.67	4969.96	2.52	0.46	28.89	25144.73	14.08	0.46	29.21	24466.43	13.58
	0.77	27.06	270.21	0.13	0.77	26.98	1251.31	0.60	0.77	27.22	4938.59	2.52	0.76	28.85	25700.47	14.44	0.76	29.11	24799.83	13.81
	1.08	27.05	270.88	0.13	1.07	26.94	1359.39	0.65	1.07	27.05	5025.80	2.58	1.06	28.82	25992.14	14.63	1.07	29.07	25285.16	14.12
	1.38	27.04	270.35	0.13	1.38	26.93	1423.28	0.68	1.38	27.06	5156.57	2.65	1.37	28.79	26301.86	14.83	1.37	28.98	25806.07	14.46
	1.69	27.05	270.14	0.13	1.69	26.93	1454.25	0.70	1.69	27.04	5373.09	2.77	1.67	28.72	26677.43	15.08	1.67	28.88	26217.66	14.75
	2.00	27.05	269.86	0.13	2.00	26.93	1490.04	0.72	1.99	27.02	5431.27	2.80	1.98	28.65	27261.19	15.46	1.98	28.80	26650.17	15.04
	2.30	27.05	270.65	0.13	2.30	26.92	1527.31	0.74	2.30	27.00	5654.42	2.93	2.28	28.62	27410.75	15.57	2.28	28.69	27194.79	15.41
	2.61	27.05	273.83	0.13	2.61	26.92	1564.89	0.76	2.61	26.98	5880.86	3.05	2.58	28.58	27626.71	15.71	2.58	28.54	27729.52	15.79
	2.92	27.04	275.27	0.13	2.92	26.92	1599.23	0.77	2.91	26.96	5982.19	3.11	2.89	28.56	27717.27	15.78	2.89	28.41	28226.15	16.15
	3.23	27.04	274.88	0.13	3.22	26.92	1626.85	0.79	3.22	26.96	6036.33	3.14	3.19	28.52	27918.70	15.92	3.19	28.26	28732.83	16.51
	3.53	27.04	274.81	0.13	3.53	26.92	1658.43	0.80	3.53	26.94	6053.77	3.15	3.50	28.50	28017.46	15.98	3.50	28.14	29395.32	16.98
	3.84	27.04	274.85	0.13	3.84	26.92	1758.37	0.85	3.83	26.94	6068.33	3.16	3.80	28.46	28128.42	16.07	3.80	27.98	29973.81	17.40
	4.15	27.04	274.93	0.13	4.15	26.92	1838.31	0.89	4.16	26.93	6064.61	3.16	4.11	28.45	28210.52	16.12	4.10	27.80	30226.99	17.63
	4.45	27.04	274.93	0.13	4.45	26.92	1894.84	0.92									4.41	27.73	30407.38	17.77
	4.76	27.03	276.07	0.13													4.71	27.68	30586.09	17.91
	5.07	27.03	276.45	0.13													5.01	27.63	30673.17	17.98
	5.38	27.03	277.08	0.13													5.32	27.58	30716.01	18.03
	5.68	27.03	277.26	0.13													5.52	27.58	30701.94	18.02
	5.99	27.03	277.43	0.13																
	6.25	27.03	274.98	0.13																

Table 5, continued.

Table 3.3

Temperature, Conductivity and Salinity profiles (from Castaway CTD)

Cruise	YR160721 / 0728				YR160721 / 0949				YR160721_2 / 1102				YR160805 / 0523				YR160805 / 0642			
Desc.	Pamunkey Sand/Mud				Pamunkey Sand/Mud				Ferry Point Sand/Mud				Goodwin Island Sand/Mud				Goodwin Island Sand/Mud			
Station Code	PM_YR160721_0728				PM_YR160721_0949				FP_YR160721_1102				GI_YR160805_0523				GI_YR160805_0642			
Water depth (m)	5.70				4.00				6.75				4.34				4.48			
	Depth (m)	Temperature (deg C)	Conductivity (µS/cm)	Salinity (PSU)	Depth (m)	Temperature (deg C)	Conductivity (µS/cm)	Salinity (PSU)	Depth (m)	Temperature (deg C)	Conductivity (µS/cm)	Salinity (PSU)	Depth (m)	Temperature (deg C)	Conductivity (µS/cm)	Salinity (PSU)	Depth (m)	Temperature (deg C)	Conductivity (µS/cm)	Salinity (PSU)
	0.15	29.84	5174.06	2.51	0.15	30.46	3189.81	1.49	0.15	29.01	31454.08	17.96	0.15	27.63	37323.57	22.33	0.15	28.07	37328.30	22.13
	0.46	29.81	5219.33	2.54	0.46	30.27	3146.21	1.47	0.45	28.93	31446.11	17.98	0.45	27.64	37317.68	22.32	0.45	28.07	37330.32	22.13
	0.77	29.81	5211.57	2.53	0.77	30.18	3120.98	1.46	0.76	28.89	31456.66	18.01	0.76	27.64	37312.65	22.32	0.76	28.07	37327.22	22.12
	1.07	29.81	5246.96	2.55	1.08	30.09	3076.89	1.44	1.06	28.77	31496.45	18.08	1.06	27.64	37323.72	22.32	1.06	28.07	37329.11	22.13
	1.38	29.80	5326.97	2.59	1.38	30.04	3036.41	1.42	1.36	28.67	31548.10	18.15	1.36	27.64	37334.95	22.33	1.36	28.06	37333.73	22.13
	1.69	29.79	5397.76	2.63	1.69	30.01	3001.58	1.41	1.67	28.62	31617.94	18.21	1.66	27.63	37332.28	22.33	1.66	28.05	37331.84	22.14
	1.99	29.79	5461.38	2.66	2.00	29.99	3002.51	1.41	1.97	28.43	31895.94	18.46	1.96	27.63	37334.80	22.34	1.96	28.04	37322.59	22.14
	2.30	29.79	5534.97	2.70	2.30	30.00	3004.95	1.41	2.27	28.26	32142.02	18.68	2.27	27.62	37331.17	22.34	2.27	28.04	37338.31	22.15
	2.61	29.79	5591.50	2.73	2.61	30.00	3013.32	1.41	2.58	28.19	32246.39	18.78	2.57	27.62	37318.70	22.33	2.57	28.04	37345.37	22.15
	2.92	29.80	5620.67	2.75	2.92	30.00	3024.85	1.42	2.88	28.13	32303.03	18.84	2.87	27.62	37322.53	22.33	2.87	28.03	37358.31	22.16
	3.22	29.80	5662.27	2.77	3.23	30.01	3027.02	1.42	3.18	28.10	32329.31	18.87	3.17	27.62	37326.52	22.34	3.17	28.03	37337.22	22.15
	3.53	29.80	5689.24	2.78	3.53	30.00	3026.19	1.42	3.49	28.10	32329.03	18.87	3.48	27.62	37354.09	22.35	3.48	28.04	37355.30	22.16
	3.84	29.80	5704.09	2.79	3.84	30.00	3025.90	1.42	3.79	28.09	32346.69	18.88	3.78	27.62	37125.94	22.20	3.78	28.03	37366.75	22.17
	4.14	29.81	5770.10	2.82	4.00	30.01	3023.99	1.42	4.09	28.07	32391.98	18.92	4.08	27.62	37187.21	22.24	4.08	28.03	37356.17	22.16
	4.45	29.81	5783.81	2.83					4.40	28.05	32535.89	19.02	4.34	27.62	37382.55	22.37	4.48	28.02	37353.42	22.16
	4.76	29.81	5807.28	2.84					4.70	28.03	32592.97	19.06								
	5.06	29.81	5819.71	2.85					5.00	28.01	32652.77	19.11								
	5.37	29.81	5866.89	2.87					5.30	28.00	32702.21	19.14								
	5.70	29.81	5880.44	2.88					5.61	27.99	32804.31	19.22								
									5.91	27.99	32817.71	19.23								
									6.21	27.99	32824.17	19.23								
									6.52	27.97	32789.76	19.21								
									6.75	27.98	32725.02	19.17								

Table 5, continued.

Table 3.4

Temperature, Conductivity and Salinity profiles (from Castaway CTD)

Cruise	YR160920 / 0633				YR160920 / 0657			
Desc.	Naval Weapons Station Mud				Naval Weapons Station Mud			
Station Code	NWS_YR160920_0633				NWS_YR160920_0657			
Water depth (m)	5.92				5.96			
	Depth (m)	Temperature (deg C)	Conductivity (µS/cm)	Salinity (PSU)	Depth (m)	Temperature (deg C)	Conductivity (µS/cm)	Salinity (PSU)
	0.15	25.55	37282.32	23.32	0.15	25.67	37403.34	23.35
	0.45	25.54	37283.19	23.33	0.45	25.66	37379.02	23.33
	0.75	25.54	37291.92	23.33	0.75	25.67	37390.95	23.34
	1.06	25.56	37295.78	23.33	1.06	25.68	37424.60	23.35
	1.36	25.61	37379.02	23.36	1.36	25.69	37443.21	23.36
	1.66	25.66	37471.03	23.39	1.66	25.70	37457.45	23.37
	1.96	25.69	37521.60	23.41	1.96	25.70	37456.33	23.37
	2.26	25.73	37594.30	23.44	2.26	25.69	37441.29	23.36
	2.57	25.75	37632.94	23.46	2.57	25.70	37451.02	23.36
	2.87	25.77	37653.98	23.47	2.87	25.70	37457.88	23.37
	3.17	25.80	37714.02	23.49	3.17	25.70	37456.34	23.36
	3.47	25.83	37784.83	23.52	3.47	25.73	37494.38	23.38
	3.77	25.86	37822.02	23.54	3.77	25.75	37544.66	23.40
	4.07	25.88	37836.51	23.54	4.07	25.77	37581.14	23.41
	4.38	25.88	37847.63	23.54	4.38	25.81	37637.50	23.44
	4.68	25.89	37852.96	23.54	4.68	25.82	37654.66	23.44
	4.98	25.89	37852.21	23.54	4.98	25.83	37680.25	23.45
	5.28	25.89	37851.81	23.54	5.28	25.84	37704.47	23.46
	5.58	25.89	37846.16	23.54	5.58	25.84	37703.29	23.46
	5.92	25.89	37859.71	23.55	5.96	25.85	37709.56	23.46

Table 6. Burst averaged ADCP water speed, direction and acoustic backscatter.

Table 4.1 intensity scale factor = 0.43 dB/count

Burst Averaged ADCP Water Column Speed, Direction and Acoustic Backscatter

Cruise / Time (EST)	YR160623 / 0648				YR160624 / 0759				YR0701/ 0617				YR160706 / 0850			
Desc.	Clay Bank Mud				Clay Bank Mud				Gloucester Pt Mud				Pamunkey Mud			
Station Code	CB_23				CB_24				GP				PM			
Water depth (m)	4.06				4.81				3.81				3.81			
	Depth (m)	Speed (cm/s)	Direction (deg)	backscatter (dB)	Depth (m)	Speed (cm/s)	Direction (deg)	backscatter (dB)	Depth (m)	Speed (cm/s)	Direction (deg)	backscatter (dB)	Depth (m)	Speed (cm/s)	Direction (deg)	backscatter (dB)
	1.06	35.98	128.20	93.15	1.06	31.62	131.88	91.33	1.06	6.92	218.23	86.07	1.06	48.69	222.07	102.98
	1.31	32.59	125.72	93.75	1.31	27.94	135.03	91.13	1.31	7.50	217.30	86.23	1.31	45.30	222.38	103.63
	1.56	33.43	124.57	93.88	1.56	22.93	130.27	90.10	1.56	2.93	215.10	85.40	1.56	44.64	223.37	103.10
	1.81	31.60	121.48	93.73	1.81	19.87	132.11	89.17	1.81	2.92	194.96	84.70	1.81	45.74	222.00	102.60
	2.06	28.41	119.64	93.13	2.06	17.43	131.90	88.33	2.06	2.15	311.47	83.77	2.06	42.56	222.96	102.00
	2.31	26.85	120.42	93.75	2.31	15.58	131.97	88.87	2.31	4.37	5.17	84.30	2.31	39.96	221.92	102.70
	2.56	24.98	118.96	94.20	2.56	16.19	131.81	89.10	2.56	6.99	353.95	84.73	2.56	39.65	221.00	103.30
	2.81	25.09	121.54	94.53	2.81	17.37	136.63	89.27	2.81	9.00	356.01	85.43	2.81	39.31	224.00	103.85
	3.06	24.01	119.84	94.70	3.06	15.51	129.92	89.43	3.06	10.71	3.03	86.17	3.06	36.13	221.47	104.45
	3.31	22.25	116.49	94.88	3.31	14.85	139.94	89.87	3.31	7.13	0.73	86.67	3.31	33.21	218.58	105.08
	3.56	22.04	120.13	94.95	3.56	14.16	138.26	90.40	3.56	6.19	343.68	86.83	3.56	28.67	221.01	105.83
	3.81	21.15	119.80	95.00	3.81	10.18	133.06	90.87	3.81	5.60	342.64	87.23	3.81	26.97	218.80	107.18
	4.06	17.05	124.92	98.58	4.06	10.71	127.59	91.13								
					4.31	7.85	124.08	91.40								
					4.56	7.24	141.88	91.97								
					4.81	4.83	122.79	107.63								

Table 6, continued.

Table 4.2																
Burst Averaged ADCP Water Column Speed, Direction and Acoustic Backscatter												intensity scale factor = 0.43 dB/count				
Cruise / Time (EST)	YR160706_2 / 1026				YR160714 / 0636				YR160714 / 0704				YR160714 / 0726			
Desc.	West Point Mud				Ferry Point Sand/Mud				Ferry Point Sand/Mud				Ferry Point Sand/Mud			
Station Code	WP				FP_0636				FP_0704				FP_0726			
Water depth (m)	4.06				4.06				4.06				4.31			
	Depth (m)	Speed (cm/s)	Direction (deg)	backscatter (dB)	Depth (m)	Speed (cm/s)	Direction (deg)	backscatter (dB)	Depth (m)	Speed (cm/s)	Direction (deg)	backscatter (dB)	Depth (m)	Speed (cm/s)	Direction (deg)	backscatter (dB)
	1.06	38.07	352.02	80.65	1.06	3.93	62.26	98.13	1.06	1.05	256.16	84.63	1.06	6.69	177.32	87.80
	1.31	41.06	353.22	80.75	1.31	14.16	323.52	93.83	1.31	7.08	317.45	82.48	1.31	1.72	174.60	86.70
	1.56	41.88	351.47	80.33	1.56	7.63	332.41	89.18	1.56	12.39	328.94	80.45	1.56	2.77	297.90	82.85
	1.81	43.28	354.76	79.63	1.81	18.46	356.43	85.28	1.81	14.45	331.49	78.70	1.81	6.77	328.52	79.45
	2.06	42.89	354.11	78.88	2.06	13.21	354.37	83.08	2.06	17.33	328.53	78.33	2.06	11.03	321.97	77.50
	2.31	44.88	353.12	80.25	2.31	16.18	344.62	83.13	2.31	15.18	332.84	79.08	2.31	10.05	319.62	77.85
	2.56	45.46	353.50	82.85	2.56	19.26	348.02	83.08	2.56	14.43	321.74	79.93	2.56	7.68	319.26	77.65
	2.81	44.91	354.99	86.23	2.81	17.45	333.87	83.35	2.81	12.58	326.03	80.73	2.81	10.27	318.78	77.90
	3.06	43.25	352.35	91.48	3.06	16.54	354.21	83.98	3.06	9.25	323.92	80.85	3.06	8.73	318.45	77.90
	3.31	43.30	353.32	95.15	3.31	9.85	328.89	84.10	3.31	10.84	322.75	80.68	3.31	6.62	321.86	77.78
	3.56	39.81	352.95	97.65	3.56	11.19	342.99	84.80	3.56	10.07	313.69	80.88	3.56	4.31	321.56	78.20
	3.81	35.76	351.77	99.70	3.81	8.39	343.46	85.85	3.81	7.36	322.13	82.08	3.81	3.18	340.23	79.00
	4.06	31.64	352.95	111.98	4.06	6.81	339.76	89.18	4.06	1.67	295.09	95.93	4.06	0.90	318.23	80.93
													4.31	9.39	155.22	110.40

Table 6, continued.

Table 4.3 intensity scale factor = 0.43 dB/count

Burst Averaged ADCP Water Column Speed, Direction and Acoustic Backscatter

Cruise / Time (EST)	YR160721 / 0811				YR160721 / 0941				YR160805 / 0659			
Desc.	Pamunkey Sand/Mud				Pamunkey Sand/Mud				Goodwin Island Sand/Mud			
Station Code	PS_0811				PS_0941				GI			
Water depth (m)	3.56				3.56				4.06			
	Depth (m)	Speed (cm/s)	Direction (deg)	backscatter (dB)	Depth (m)	Speed (cm/s)	Direction (deg)	backscatter (dB)	Depth (m)	Speed (cm/s)	Direction (deg)	backscatter (dB)
	1.06	33.09	224.78	103.38	1.06	0.90	197.43	92.43	1.06	6.43	340.03	87.08
	1.31	32.91	225.40	103.38	1.31	1.18	128.56	92.90	1.31	6.3	339.54	86.23
	1.56	31.23	222.47	102.55	1.56	2.38	173.22	92.00	1.56	7.63	337.78	84.45
	1.81	32.30	222.52	101.63	1.81	1.51	84.68	91.13	1.81	7.17	334.64	82.63
	2.06	28.65	221.26	100.83	2.06	2.95	98.55	90.43	2.06	6.84	330.1	80.85
	2.31	28.49	220.56	101.35	2.31	3.92	131.72	90.93	2.31	5.99	326.48	80.30
	2.56	26.23	221.10	101.80	2.56	4.69	69.02	91.35	2.56	6.33	325.04	79.80
	2.81	24.58	220.94	102.18	2.81	5.66	25.98	91.78	2.81	7.05	331.68	79.20
	3.06	21.78	221.11	102.53	3.06	4.37	32.13	92.10	3.06	9.29	331.97	78.93
	3.31	18.50	225.75	102.93	3.31	4.63	18.03	92.48	3.31	8.21	318.71	78.60
	3.56	17.54	219.97	109.10	3.56	6.02	38.08	93.18	3.56	8.67	327.13	78.43
									3.81	9.6	327.42	79.30
									4.06	10.49	248.26	107.80

Table 7. Sediment prcent moisture, porosity, volatile solids and fixed solids (by net weight).

Sediment Percent Moisture, Porosity, Volitile Solids and Fixed Solids (by wet weight)

Cruise / Time (EST)	YR160624 / 0708					YR0701/ 0659					YR160706 / 0926					YR160706_2 / 1023				
Desc.	Clay Bank Mud					Gloucester Pt Mud					Pamunkey Mud					West Point Mud				
Station Code	CB					GP					PM					WP				
Water depth (m)	5.15					4.56					6.25					4.16				
	Depth (cm)	Moisture (%)	Porosity (%)	Volitle Solids (%)	Fixed Solids (%)	Depth (cm)	Moisture (%)	Porosity (%)	Volitle Solids (%)	Fixed Solids (%)	Depth (cm)	Moisture (%)	Porosity (%)	Volitle Solids (%)	Fixed Solids (%)	Depth (cm)	Moisture (%)	Porosity (%)	Volitle Solids (%)	Fixed Solids (%)
	0.5	69.26	85.47	2.42	28.32	0.5	73.23	87.72	2.49	24.28	0.5	62.49	81.30	2.34	35.17	0.5	60.60	80.06	1.65	37.75
	1.5	67.72	84.56	2.56	29.72	1.5	68.40	84.96	2.65	28.95	1.5	69.37	85.53	2.81	27.82	1.5	41.34	64.78	1.62	57.04
	2.5	68.34	84.92	2.53	29.13	2.5	67.21	84.25	2.51	30.28	2.5	73.17	87.68	2.97	23.86					
	3.5	63.63	82.03	2.60	33.77	3.5	64.38	82.51	2.50	33.12	3.5	71.63	86.83	2.99	25.38					
	4.5	61.73	80.81	2.65	35.62	4.5	59.09	79.03	2.33	38.59	4.5	61.97	80.96	2.75	35.28					
	5.5	60.79	80.18	2.66	36.55	5.5	55.76	76.69	2.29	41.95	5.5	52.73	74.43	2.31	44.96					
	6.5	59.78	79.50	2.74	37.48	6.5	52.62	74.35	2.24	45.14	6.5	48.87	71.39	2.11	49.02					
	7.5	59.35	79.22	2.65	38.00	7.5	49.45	71.85	2.25	48.31	7.5	47.56	70.30	2.09	50.35					
	8.5	60.45	79.96	2.65	36.90	8.5	45.39	68.45	2.19	52.41	8.5	49.18	71.64	2.15	48.67					
	9.5	61.75	80.82	2.69	35.56	9.5	44.30	67.49	2.20	53.50	9.5	47.53	70.27	2.11	50.36					

Sediment Percent Moisture, Porosity, Volitile Solids and Fixed Solids (by wet weight)

Cruise / Time (EST)	YR160714 / 0636					YR160721 / 0728					YR160805 / 0523					YR160920 / 0633				
Desc.	Ferry Point Sand/Mud					Pamunkey Sand/Mud					Goodwin Island Sand/Mud					Naval Weapons Station Mud				
Station Code	FP					PS					GI					NWS				
Water depth (m)	4.11					5.70					4.34					5.92				
	Depth (cm)	Moisture (%)	Porosity %	Volitle Solids (%)	Fixed Solids (%)	Depth (cm)	Moisture (%)	Porosity (%)	Volitle Solids (%)	Fixed Solids (%)	Depth (cm)	Moisture (%)	Porosity (%)	Volitle Solids (%)	Fixed Solids (%)	Depth (cm)	Moisture (%)	Porosity (%)	Volitle Solids (%)	Fixed Solids (%)
	0.5	45.77	68.78	1.57	52.66	0.5	25.47	47.14	0.45	74.09	0.5	31.12	54.11	0.80	68.08	0.5	63.25	81.79	3.01	33.74
	1.5	39.54	63.06	1.52	58.94	1.5	23.36	44.30	0.55	76.09	1.5	28.05	50.43	0.80	71.15					
	2.5	34.32	57.69	1.33	64.35	2.5	33.85	57.18	2.13	64.03	2.5	24.78	46.23	0.75	74.48					
	3.5	27.48	49.73	1.00	71.52	3.5	26.04	47.89	1.12	72.84	3.5	24.60	46.00	0.79	74.61					
	4.5	23.95	45.11	0.82	75.23						4.5	23.60	44.64	0.71	75.69					
	5.5	24.21	45.47	0.89	74.90						5.5	22.44	43.03	0.69	76.87					
	6.5	22.36	42.92	0.72	76.91						6.5	22.10	42.55	0.63	77.26					
	7.5	22.40	42.97	0.83	76.77						7.5	22.12	42.57	0.64	77.24					

Table 8. Sediment grainsize and organic matter (by dry weight).

Table 5

Sediment Percent Grainsize and Oganic Matter (by dry weight)

Cruise / Time (EST) Desc. Station Code Water depth (m)	Core Depth (cm)	>850 (%)	>850 Organic (%)	Sand (%)	Sand Organic (%)	Silt (%)	Silt Organic (%)	Clay (%)	Clay Orgainic (%)
YR160624 / 0708	0.5	0.18	0.01	3.28	0.40	39.69	0.79	45.88	9.77
Clay Bank Mud	1.5	0.00	0.00	2.94	0.13	46.32	0.42	39.51	10.68
CB	2.5	0.00	0.00	3.75	0.18	50.24	0.18	34.29	11.37
5.15	3.5	0.00	0.00	5.77	0.24	44.48	0.93	39.06	9.51
	4.5	0.05	0.00	8.14	0.18	45.02	0.30	36.14	10.17
	5.5	0.03	0.01	9.40	0.17	45.89	1.75	33.54	9.21
	6.5	0.00	0.00	8.36	0.17	42.21	0.67	39.26	9.33
	7.5	0.00	0.00	6.97	0.47	39.89	0.90	43.28	8.50
	8.5	0.00	0.00	4.84	0.07	42.37	0.75	42.92	9.05
	9.5	0.17	0.01	5.64	0.20	42.12	1.04	41.91	8.92
YR0701/ 0659	0.5	0.00	0.00	9.90	0.11	49.84	1.66	29.18	9.30
Gloucester Pt Mud	1.5	0.04	0.00	11.64	2.47	47.69	0.25	28.87	9.04
GP	2.5	0.00	0.02	13.36	0.14	47.15	0.16	29.49	9.70
4.56	3.5	0.00	0.02	17.37	0.15	45.19	0.46	27.90	8.91
	4.5	0.33	0.01	31.24	0.17	36.15	1.08	24.23	6.79
	5.5	0.97	0.03	35.57	0.22	34.46	0.57	21.77	6.41
	6.5	0.27	0.02	43.03	0.34	29.08	1.05	21.95	5.25
	7.5	4.33	0.13	45.92	0.39	21.13	0.88	22.83	4.39
	8.5	4.01	0.04	48.50	0.22	25.08	1.05	16.91	4.20
	9.5	0.88	0.02	51.87	0.40	23.73	0.19	18.51	4.41
YR160706 / 0926	0.5	0.00	0.05	43.41	1.15	24.38	1.36	23.40	6.26
Pamunkey Mud	1.5	0.06	0.01	11.40	1.04	40.75	2.55	34.95	9.24
PM	2.5	0.00	0.00	3.26	0.44	51.26	2.21	31.06	11.76
6.25	3.5	0.00	0.00	3.92	0.88	46.35	1.82	36.47	10.56
	4.5	0.03	0.01	29.55	0.58	32.54	1.20	28.72	7.36
	5.5	0.08	0.03	48.44	0.43	21.53	0.55	23.85	5.08
	6.5	0.00	0.03	63.98	0.77	16.31	0.00	14.52	4.33
	7.5	0.00	0.00	63.00	0.58	15.74	0.65	15.99	4.04
	8.5	0.01	0.01	58.93	0.45	18.84	0.63	16.64	4.50
	9.5	0.01	0.03	63.62	0.71	16.44	0.50	15.05	3.64
YR160706_2 / 1023	0.50	0.00	0.00	62.09	0.27	19.44	0.29	12.33	5.59
West Point Mud	1.50	0.04	0.03	73.12	0.21	13.34	0.09	9.92	3.25
WP									
4.16									
YR160714 / 0636	0.5	0.59	0.01	75.74	0.14	15.49	0.38	4.35	3.30
Ferry Point Sand/Mud	1.5	0.86	0.01	76.46	0.09	14.35	0.22	4.57	3.45
FP	2.5	0.90	0.02	81.32	0.08	10.65	0.08	4.31	2.64
4.11	3.5	0.94	0.00	87.13	0.05	7.37	0.18	2.58	1.75
	4.5	0.65	0.03	89.85	0.07	6.07	0.00	1.97	1.77
	5.5	0.40	0.00	89.70	0.05	6.62	0.50	1.54	1.20
	6.5	0.64	0.05	89.58	0.06	5.84	0.10	2.33	1.41
	7.5	0.86	0.17	89.98	0.11	5.58	0.00	1.83	1.51
YR160721 / 0728	0.5	0.24	0.26	96.39	0.09	1.98	0.44	0.44	0.17
Pamunkey Sand/Mud	1.5	0.80	0.22	96.45	0.08	1.79	0.00	0.46	0.60
PS	2.5	1.49	3.05	87.27	0.22	4.91	0.30	1.09	1.66
5.70	3.5	2.11	3.81	85.92	0.15	5.20	0.00	1.46	1.50
YR160805 / 0523	0.5	0.07	0.01	83.10	0.14	4.38	1.34	9.72	1.24
Goodwin Island Sand/Mud	1.5	0.17	0.01	83.42	0.14	4.65	0.96	9.37	1.27
GI	2.5	0.01	0.00	82.98	0.09	4.74	1.18	9.64	1.37
4.34	3.5	0.50	0.03	81.40	0.10	5.19	1.63	9.67	1.47
	4.5	0.06	0.00	84.82	0.10	4.10	1.31	8.35	1.25
	5.5	0.01	0.01	84.93	0.09	4.39	1.14	8.29	1.14
	6.5	0.00	0.01	86.73	0.13	3.42	1.02	7.43	1.26
	7.5	0.00	0.00	88.93	0.17	3.04	0.61	6.48	0.77
YR160920 / 0633	surface	0.08	0.01	7.90	0.13	48.79	0.61	32.90	9.58
Naval Weapons Station Mud									
NWS									
5.92									

Literature Cited

1. Bradshaw, A. L., and Karl E. Schleicher, "Electrical conductivity of seawater," *IEEE Journal of Oceanic Engineering* 5(1), 50-62, 1980.

2. Kingdon, James B., Bruce J. Barrow, Thomas H. Bell, David C. George, Glenn R, Harbaugh and Daniel A, Steinhurst, "TEMTADS Adjunct Sensor Systems: Hand-held EMI Sensor for Cued UXO Discrimination (ESTCP MR-200807) and Man-Portable EMI Array for UXO Detection and Discrimination (ESTCP MR-200909) Final Report," Naval Research Laboratory Report NRL/MR/6110--12-9401, April 2012.

3. Friedrichs, C.T., "York River physical oceanography and sediment transport," In: K.A. Moore and W.G. Reay, (eds.), A Site Profile of the Chesapeake Bay National Estuarine Research Reserve, Virginia, *Journal of Coastal Research Special Issue* 57, pp. 17-22, 2009.

4. Hobbs, Carl, "York River Geology," In: K.A. Moore and W.G. Reay, (eds.), A Site Profile of the Chesapeake Bay National Estuarine Research Reserve, Virginia, *Journal of Coastal Research Special Issue* 57, pp. 10-16, 2009.

5. Clark, William B. and Benjamin L. Miller, "Physiography and Geology of the Coastal Plain Province of Virginia," *Virginia Geological Society Bulletin* 9, 1912.

6. Dellapenna, Timothy M., Steven A. Kuehl, and Linda C. Schaffner, "Ephemeral deposition, seabed mixing and fine-scale strata formation in the York River estuary, Chesapeake Bay," *Estuarine, Coastal and Shelf Science* 58(3), 621-643, 2003.

7. Evans, Rob L., "Measuring the shallow porosity structure of sediments on the continental shelf: A comparison of an electromagnetic approach with cores and acoustic backscatter," *Journal of Geophysical Research: Oceans* 106(C11), 27047-27060, 2001.

8. Jackson, Darrell R. and Michael D. Richardson, *High-Frequency Seafloor Acoustics*, §4.4.2, Springer, 2007.

9. Massey, G.M. and C.T. Friedrichs, 2016 Data collected for Resistivity, Magnetic Susceptibility and Sediment Characterization of the York River Estuary, VA in Support of the Empirical Investigation of the Factors Influencing Marine Applications of EMI (Year 2 of SERDP Project MR-2409), 2017. https://doi.org/10.21220/V5VG67

10. Gust, G., & V. Müller, “Interfacial hydrodynamics and entrainment functions of currently used erosion devices,” In N. Burt, R. Parker, & J. Watts (Eds.), Cohesive sediments – Proc. 4th Nearshore and Estuarine Cohesive Sediment Transport Conference INTERCOH '94, Wallingford, 149–174, Chichester, UK: Wiley, July 1994.

11. Massey, G.M. and C.T. Friedrichs, “Resistivity, Magnetic Susceptibility and Sediment Characterization of the York River Estuary in Support of the Empirical Investigation of the Factors Influencing Marine Applications of EMI (Year 2 of SERDP Project MR-2409),” Final Report. Virginia Institute of Marine Science, College of William and Mary, 2017. https://doi.org/10.21220/V5QS3Z

12. Plumb, R.H. Jr., “Procedures for Handling and Chemical Analysis of Sediment and Water Samples,” Technical Report EPA/CE-81-1. Great Lakes Laboratory, State University College at Buffalo, Buffalo, NY. 1981.

13. Dickhudt, Patrick J., Carl T. Friedrichs, and Lawrence P. Sanford, "Mud matrix solids fraction and bed erodibility in the York River estuary, USA, and other muddy environments," *Continental Shelf Research* 31(10), S3-S13, 2011.

14. Wheatcroft, R.A., “In situ measurements of near-surface porosity in shallow-water marine sands,” *IEEE Journal of Oceanic Engineering* 27, 561–570, 2002.

15. Cartwright, Grace M. and Carl T. Friedrichs, "Resistivity, Magnetic Susceptibility and Sediment Characterization of the York River in support of the Empirical investigation of the factors influencing marine applications of EMI," VIMS Report CHSD-2015-01, January 2015.

16. M. N. Nabighian, “Quasi-static transient response of a conducting half-space - An approximate representation,” Geophysics, 44(10), 1700-1705, 1979.

17. Steinhurst, D.A, G.R. Harbaugh, J.B. Kingdon, T. Furuya, D.A. Keiswetter and D.C. George, "EMI Array for Cued UXO Discrimination," ESTCP Project MR-200601 Final Report, July 2010.

18. Fletcher, J., T. Judendorfer, M. Mueller, N. Hassanain, and M. Muhr, "Electrical issues associated with sea-water immersed windings in electrical generators for wave-and tidal current-driven power generation," *IET Renewable Power Generation*, 3(2), 254-264, 2009.

19. Kuipers, Johannes, Harry Bruning, Doekle Yntema, Simon Bakker, and Huub Rijnaarts, "Self-capacitance and resistive losses of saline-water-filled inductors," *IEEE Transactions on Industrial Electronics*, 61(5), 2356-2361, 2014.

20. Bana, Viktor, Greg Anderson, Lu Xu, Doeg Rodriguez, Alex Phipps and John D. Rockway, "Characterization of Coupled Coil in Seawater for Wireless Power Transfer," SPAWAR Systems Center Pacific Technical Report 2026, September 2013.

21. Askari, Alex, Robert Stark, Joseph Curran, Donald Rule, and Kevin Lin, "Underwater wireless power transfer," *Proc. 2015 IEEE Wireless Power Transfer Conference (WPTC)*, pp. 1-4, 2015.

22. Jenkins, Alonzo, Viktor Bana, and Goran Anderson, "Impedance of a coil in seawater," *Proc. 2014 IEEE Antennas and Propagation Society International Symposium (APSURSI)*, pp. 625-626, 2014.

23. Harbaugh, G.R., D.A. Steinhurst, M. Howard, B.J. Barrow, J.T. Miller, and T.H. Bell, "Quantification of Noise Sources in EMI Surveys Technology Demonstration Report, Army Research Laboratory Blossom Point Facility, Maryland, July – September, 2006," Naval Research Laboratory Report NRL/MR/6110--10-9235, January 2010.

24. SanFilipo, Bill, and I.J. Won, "Broadband Electromagnetic Detection and Discrimination of Underwater UXO," SERDP Project MR-1321 Final Report, August 2005.

25. Bell, Thomas, "Phenomenology and Signal Processing for UXO/Clutter Discrimination," SERDP Project MR-1595 Final Report, August 2009.

26. Norton, Stephen J., William A. SanFilipo, and I. J. Won, "Eddy-current and current-channeling response to spheroidal anomalies," *IEEE Transactions on Geoscience and Remote Sensing* 43(10), 2200-2209, 2005.

27. Mahmoudi, Masoud, and Soon Yim Tan, "Depth detection of conducting marine mines via eddy-current and current-channeling response," *Progress In Electromagnetics Research* 90, 287-307, 2009.

28. Bell, Thomas, "Magnetic Surface Modes and UXO/Clutter Classification and Discrimination,", SERDP Project MR-1658 Final Report, December 2011.

29. Bell, Thomas, "Demonstration Report at Former Southwestern Proving Ground, Hope, Arkansas," ESTCP Project MR-201310, May 2015.

30. Bell, Thomas, Daniel Steinhurst, Glenn Harbaugh, James Kingdon, Bruce Barrow and Dave George, "Transient EMI Arrays for UXO Classification and Discrimination," SEG Annual Meeting, San Antonio, September 2011.

31. Barrow, Bruce, Thomas Bell and Daniel Steinhurst, "Noise Sources and Parameter Estimation in Recently Developed EMI Sensors Used for UXO Discrimination," Symposium

on the Application of Geophysics to Engineering and Environmental Problems, Tucson, AZ, March 2012.

32. Billings, Stephen D. and Lin-Ping Song, "Determining Detection and Classification Potential of Munitions using Advanced EMI Sensors in the Underwater Environment," SERDP Project MR-2412 Final Report, November 2016.

33. Hendrickx, J.M.H., B. Borchers, D.L. Corwin, S.M. Lesch, A.C. Hilgendorf and J. Schlue, "Inversion of Soil Conductivity Profiles from Electromagnetic Induction Measurements: Theory and Experimental Verification," *Soil Sci. Soc. Am. J.* 66, 673–685 2002.

34. Müller, Hendrik, Tilo von Dobeneck, Christian Hilgenfeldt, Bill SanFilipo, Daniel Rey and Belén Rubio, "Mapping the magnetic susceptibility and electric conductivity of marine surficial sediments by benthic EM profiling," *Geophysics* 77(1), 1-14, 2012.

35. McDonald, Jim, "Marine Towed Array Technology Demonstration Blossom Point Research Facility," ESTCP project MR-200324 Final Report, August 2009.

36. Cartwright, Grace M. and Carl T. Friedrichs, "Development of a Sediment Transport Model for the Chesapeake Bay: Supporting Physical Data from VIMS Potomac River Intensive Surveys August 19-28, 2004 and September 20-23, 2005," Virginia Institute of Marine Science Report CHSD-206-02, 2006.

37. Lippson, Alice L., Michael S. Haire, A. Frederick Holland, Fred Jacobs, Jorgen Jensen, R. Lynn Moran-Johnson, Tibor T. Polgar and William A Richkus, *Environmental Atlas of the Potomac Estuary*, prepared for Power Plant Siting Program, Maryland Department of Natural Resources by the Environmental Center of Martin Marietta Corporation, Williams and Heintz Map Company, 1979.

38. Cheng, David H.S., "The reflected impedance of a circular coil in the proximity of a semi-infinite medium," *IEEE Transactions on Instrumentation and Measurement* 14(3), 107-116, 1965.

39. Magnus, W., Harry Bateman, Arthur Erdélyi, F. Oberhettinger, and F. G. Tricomi, *Tables of Integral Transforms*, McGraw-Hill, 1954.

40. Ward, Stanley H., and Gerald W. Hohmann, "Electromagnetic theory for geophysical applications," *Electromagnetic Methods in Applied Geophysics, Vol. 1, Theory,* Misac N. Nabighian (ed.), Society of Exploration Geophysicists, 131-311, 1988.

41. Song, Lin-Ping, S.D. Billings, L.R. Pasion and Douglas W. Oldenburg, "Transient electromagnetic scattering of a metallic object buried in underwater sediments," *IEEE Transactions on Geoscience and Remote Sensing* 54(2), 1091-1102, 2016.

42. Farquharson, C.G. and D.W. Oldenburg, “Inversion of time-domain electromagnetic data for a horizontally layered Earth,” *Geophys. J. Int.* 114(3), 433-442, 1993.

43. Das, Y, "Effects of soil electromagnetic properties on metal detectors." *IEEE Transactions on Geoscience and Remote Sensing* 44(6), 1444-1453, 2006.

44. Monteath, G.D., *Applications of the Electromagnetic Reciprocity Principle*, Pergamon Press, 1973.